THE UNIVERSITY *of* EDINBURGH

On the Formation and Growth of Vapour Bubbles

Patrick Sullivan

Doctor of Philosophy

The University of Edinburgh

2023

This is for the haters

Sarah

Carlos

Saikat

Abstract

Vapour bubble formation has been attributed as the driving factor behind natural phenomena such as geyser formation and volcanic eruptions. The strong forces associated with the formation of bubbles has been utilised for ultrasonic cleaning. The high heat fluxes dissipated from surfaces during bubble formation and growth has seen pool boiling attracting significant interest in thermal management systems. On the other hand, the explosive failure of pressurised containers and wear of turbomachinery caused by cavitation bubbles highlight the deleterious effects of vapour bubbles on industrial processes. Understanding the formation and growth behaviour of vapour bubbles is therefore an important open problem, and current theoretical models remain incomplete.

The understanding of homogeneous vapour bubble growth is currently restricted to asymptotic descriptions of their limiting behaviour. While attempts have been made to incorporate both the inertial and thermal limits into bubble growth models, the early stages of bubble growth have not been captured. By accounting for both the changing inertial driving force and the thermal restriction to growth, an inertio-thermal model of homogeneous vapour bubble growth is developed, capable of accurately capturing the evolution of a bubble from the nano- to the macro-scale. These model predictions are compared with: a) published experimental and numerical data, and b) new molecular simulations, showing significant improvement over previous models. This work utilises molecular dynamics (MD) simulations to investigate nanoscale vapour bubble growth. MD is a technique where the future positions and momenta of the molecules in a system are determined according to a defined intermolecular potential used to compute forces between molecules. A velocity-verlet algorithm is then used to integrate Newton's equations of motion to calculate future molecule positions.

In practise, vapour bubbles typically form heterogeneously, on a solid surface where the barrier to nucleation is lower. The majority of the industrial and scientific interest in the the study of vapour bubbles has, therefore, been investigating the formation and growth of heterogeneous bubbles. Much research has been performed on the effects of the surface on the formation and ultimate detachment of the bubbles. However, the role that the surface plays in determining the growth of the bubble is still poorly understood. Currently, theoretical understanding of heterogeneous vapour bubble growth is limited to hemispherical bubbles or completely spherical bubbles next to a heated surface. By accounting for the effect of the surface on both the geometry of the bubble and on the available thermal energy, the *homogeneous* inertio-thermal model is extended to capture the effect of surface wettability on *heterogeneous* vapour bubble growth. Using

molecular simulations, the effect of bubble geometry on growth rate is investigated. This is achieved by modifying the strength of the fluid-solid intermolecular forces to obtain different bubble contact angles. The resulting bubble growth simulations showed good agreement with theoretical predictions.

These heterogeneous bubble growth simulations show the formation of a non-evaporating layer (NEL) of molecules underneath bubbles on wetting surfaces. The NEL has been shown to alter the interfacial free energy balance at the three phase contact line, causing a change in the contact angle behaviour of the bubbles. The subsequent effect of this layer on the growth rate of vapor bubbles is analysed in this work. An energy balance criterion is developed to predict the formation of the NEL, accounting for the potential contributions from the solid-fluid and fluid-fluid interactions. This analysis highlights how the non-continuum nature of the fluid under the bubble on hydrophilic surfaces plays a vital role in determining the bubble shape and subsequent dynamics.

The effect of surface wettability on vapour bubble nucleation has been widely studied due to its particular importance to two-phase thermal management systems. Classical nucleation theory (CNT) predicts that nucleation occurs preferentially on hydrophobic surfaces due to a reduced energy barrier. While there have been many investigations highlighting the agreement of experimental data to classical nucleation theory, molecular simulation results have observed preferential nucleation on hydrophilic surfaces. These surprising results arise from the methodology used in the simulations, where the results become strongly dependant on non-equilibrium and temporal effects. Using an isothermal-isobaric ensemble, this work shows how the predictions of CNT can be recovered in molecular simulation. Further testing investigates the role of surface roughness on nucleation. Distinct regimes are identified for bubble growth from surface cavities. Wetted cavities are shown to not significantly alter nucleation behaviour, while dewetted cavities are shown to reduce the temperature required for sustained bubble growth.

It is hoped that the findings presented in this thesis help improve the understanding of the fundamental physical processes responsible for the formation and growth of vapour bubbles. These findings, have application to help improve the performance and design of micro- and nano-fluidic devices, as well as two-phase thermal management systems.

Lay Summary

Despite their simple appearance, there is rich physics surrounding bubbles with many industrial and scientific applications, making them of interest to scientists and engineers alike. As the applications of bubbles can be wide reaching, understanding their behaviour requires combining surface science, fluid mechanics, and thermodynamics. Surface tension controls the shape of bubbles, pulling them into a round shape whether in the bulk of a liquid or on a surface. The large pressures inside bubbles can cause explosions, like those that send a champagne cork flying, showing the immense power that can be harnessed from controlling the flow of bubbles. Controlling bubbles can be difficult, as they are very sensitive to their surrounding conditions. The bubbles in a pot of boiling water form at 100 °C at sea level, but will form at 80 °C at the top of Mount Everest as the pressure of the water in the pot and surrounding air is lower.

These vapour bubbles consist of only the vapour of the liquid they have formed in, differing from gas bubbles, which contain a different gas substance such as the carbon dioxide in water found in fizzy drinks. While there is not much difference in the appearance of these two types of bubble, they can behave very differently. Vapour bubbles must either continuously grow or quickly collapse back into the liquid they are contained in, while gas bubbles are much more stable and can remain the same size for extended periods of time. These differences mean that vapour bubbles are much more sensitive to the temperature and pressure of the liquid they are growing in. Understanding exactly how temperature and pressure effect the formation and growth rate of vapour bubbles is important to understanding how vapour bubbles can be used to cool electronics and clean surfaces using ultra-fast vibrations. To further understand how these technologies can be improved, we must understand how these bubbles behave at the smallest sizes.

This research uses molecular dynamics (MD) simulations to understand how the smallest bubbles form and grow. MD is a technique that simulates the motion of all the molecules in the system, allowing for accurate modelling of the smallest possible bubbles. The advantages of MD include the ability to capture molecular scale phenomena, most notably the effect of the surface on which the bubble forms. These effects would need to be added using additional mathematical models and using other simulation techniques. MD does, however, require significant computational resources, which limits the simulations to lengths of nanometers and times of nanoseconds. While the bubbles at these length

scales are too small to see and the timescale is thousands of times quicker than the blink of an eye, these are the scales at which bubbles initially form. This makes MD a useful tool for investigating the formation of vapour bubbles and the early stages of their growth.

In this research, a new model for the growth of spherical vapour bubbles is proposed. The model expands on existing bubble growth models by accounting for fluid dynamic effects that are most relevant in the initial stages of bubble growth. By comparing predictions of the new model to MD simulation results, it is shown that these effects are indeed needed to accurately predict the growth of vapour bubbles in a bulk liquid. This model is then expanded to capture the differences between bubbles growing in a bulk liquid and on a wall. By accounting for the change in shape of the bubble due to the wall, changing from a sphere to a droplet like spherical cap, the growth of the bubble can again be predicted. Accounting for the effect of the wall is particularly important because it is easier for bubbles to form on walls than in bulk liquid. This means that, in practise, most bubbles form on surfaces. The role of the surface chemistry and geometry on the formation of vapour bubbles is then explored, with a strong relationship between these factors and bubble formation observed.

Acknowledgements

Firstly, I would like to thank my supervisor, Rohit, for his constant support and advice throughout the journey I have undergone the past few years. The guidance I continue to receive has helped me develop not just as a researcher, but also as a person. While this has not been an easy process, it has been made immeasurably more so thanks to his patience, understanding, and belief.

I would also like to acknowledge the role that my extended supervision team has played in helping me through this process. The regular meetings with Matthew, Duncan, and Ryan have helped me to better understand my work and provided stimulating discussion, bearing many fruitful ideas. More importantly, they have acted as exemplary role models, showing what is needed to be a good researcher. I hope to repay the work they have put in to help me, and to achieve the potential they have seen in me.

Finally, I would like to thank everyone who has helped make my life bearable throughout the last few years. The difficulties of the pandemic have affected us all, and the support I received during that time cannot go understated. Without the help and support of close friends and family, none of this would have been possible.

Declaration

I declare that this thesis was composed by myself, that the work contained herein is my own except where explicitly stated otherwise in the text, and that this work has not been submitted for any other degree or professional qualification except as specified.

Patrick Sullivan

Contents

Figures and Tables

Figures

Tables

Chapter 1

Background

1.1 Vapour Bubbles

Bubbles, at their simplest, consist of a volume of gas contained within a liquid phase (Prosperetti, 2004). This definition encompasses several different categories of bubble, each of which represents an area of significant research and rich underlying physics. For example, soap bubbles consist of a thin layer of liquid, encapsulating a gas phase inside. Due to the light weight of the liquid film and lower density of the typically warmer gas inside the bubble than outside, these bubbles will rise against gravity. The lifetime of these bubbles is determined by the stability of the liquid film, disappearing once the film is disturbed. A collection of these bubbles forms a foam, such as that found on top of a cappuccino, which itself is a topic of significant interest to researchers.

These bubbles differ significantly from bubbles contained in the bulk of a liquid. For bubbles contained entirely in a liquid, the stability of the bubble is no longer determined by the stability of a thin film, but by the pressure difference across the bubble interface. Additionally, the composition of these bubbles can play a significant role in determining their stability and dynamics. The gas phase can consist of either a different fluid to the surrounding liquid, for example air bubbles in water, or the vapour of the liquid. Bubbles containing a different gas rely on species diffusion to grow and can remain stable either in the bulk of the fluid (Dergarabedian, 1953) or attached to a solid surface (Robinson, 2002) for considerable periods of time. Bubbles containing only vapour of the surrounding liquid are much less stable, growing through thermal diffusion to maintain a pressure difference or collapsing back into an entirely liquid state (Prosperetti, 2017).

Bubbles that form entirely within the bulk of the liquid are called homogeneous, while those forming on a solid surface are called heterogeneous. Both homogeneous and heterogeneous bubbles attempt to form a minimal surface that minimises the free energy of the system. For homogeneous bubbles this takes the form of a sphere, the shape that provides the minimum surface area per unit volume. The presence of the wall for heterogeneous bubbles alters the shape that minimises the free energy. In this case, the bubble takes the shape of a spherical cap, with the contact angle θ determined by the balance of interfacial excess energies of the three-phase interfaces. The difference

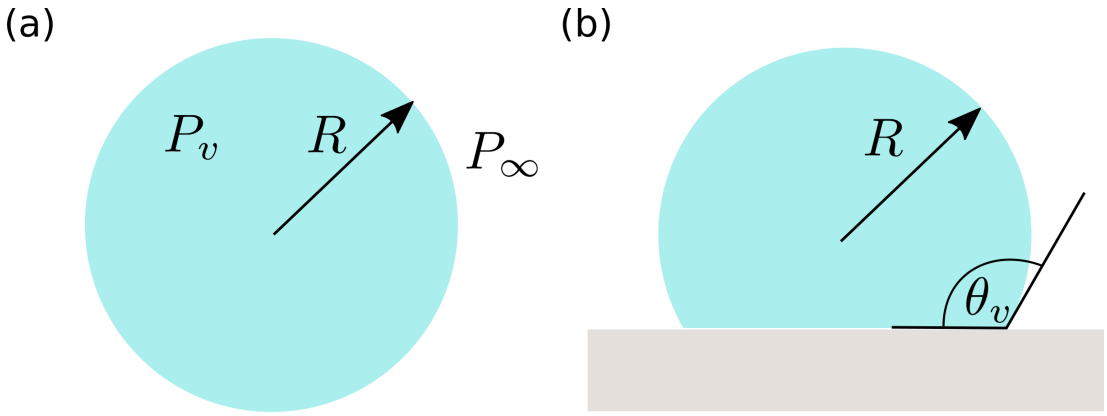

Figure 1.1: Schematics of (a) a homogeneous vapor bubble and (b) a heterogeneous vapour bubble with contact angle θ_v measured from the vapour side. The radius of curvature of the bubble is given by R with P_v and P_∞ representing the vapour pressure and far field pressure, respectively.

between homogeneous and heterogeneous bubbles is highlighted in figure 1.1. The shape of the bubble, whether it is homogeneous or heterogeneous, plays a significant role in the formation and subsequent growth of the bubble. The existing theories describing these effects will be presented in the section 1.2 and section 1.3.

1.2 Bubble Growth

1.2.1 Homogeneous Bubble Growth

The dynamics of bubbles were initially analysed by Rayleigh (1917), who equated the kinetic energy of the moving bubble to the work done by moving the interface. This gave a limiting expression for the velocity of a bubble as a function of its radius. This analysis was expanded by Plesset and Zwick (1954), who derived an expression for bubble growth accounting for the effects of viscosity and capillarity:

$$\underbrace{R\ddot{R} + \frac{3}{2}\dot{R}^2}_{\text{Inertia}} = \frac{1}{\rho_l}\left(\underbrace{P_v - P_\infty}_{\text{Pressure difference}} - \underbrace{\frac{2\gamma}{R}}_{\text{Capillarity}} - \underbrace{\frac{4\mu\dot{R}}{R}}_{\text{Viscosity}}\right), \tag{1.1}$$

where the R, $\dot{R}$, and $\ddot{R}$ represent the radius, radial velocity, and radial acceleration, respectively. The liquid density is given by ρ_l, surface tension by γ, and the the dynamic viscosity by μ. This expression is commonly referred to as the Rayleigh–Plesset (RP) equation. Equation (1.1) has been further generalised to account for non-Newtonian viscosity and mass transfer at the liquid-vapour interface (Prosperetti & Plesset, 1978) as well as the effects of non-condensable gasses (Brennen, 2013). By

integrating equation (1.1), it has been shown that the inertial bubble velocity reaches a maximum value of A, given as (Prosperetti, 2017):

$$\dot{R}_{\mathrm{RP,max}} = A = \sqrt{\frac{2\Delta P}{3\rho_l}}. \tag{1.2}$$

Taking the initial acceleration of $\ddot{R} = \Delta P/\rho_l R_0$ (Brennen, 2013, p. 38), the time taken by a stationary bubble of initial size R_0 to reach this inertial velocity A, can be approximated as:

$$\tau_{\mathrm{RP}} = \frac{A}{\ddot{R}} = R_0\sqrt{\frac{2\rho_l}{3\Delta P}}. \tag{1.3}$$

One of the earliest experimental investigations into the growth rates of vapour bubbles was performed by Dergarabedian (1953), who managed to achieve homogeneous nucleation by heating the bulk of the liquids. These experimental results were used as comparison by Plesset and Zwick (1954), who developed a model for bubble growth controlled by thermal diffusion, that accurately modelled the experimental data. This model, called the PZ model, approximates the solution to the energy equation by making a thin thermal boundary layer approximation. The energy equation, expressed in spherical coordinates is given as:

$$\frac{\partial T\left(r,t\right)}{\partial t} + \frac{R^2\left(t\right)}{r^2}\frac{dR\left(t\right)}{dt}\frac{\partial T\left(r,t\right)}{\partial r} = \frac{\alpha}{r^2}\frac{\partial}{\partial r}\left(r^2\frac{\partial T\left(r,t\right)}{\partial r}\right), \tag{1.4}$$

where $T\left(r,t\right)$ represents the temperature of the liquid with thermal diffusivity α at a radial distance r from the centre of a bubble of radius $R\left(t\right)$. This gives an expression for the thermal-diffusion limited growth of a vapour bubble:

$$\dot{R}_{\mathrm{PZ}} = Ja\sqrt{\frac{3\alpha}{\pi t}}, \tag{1.5}$$

where $\alpha = k/\rho_l c_p$ is the thermal diffusivity of the liquid, k is the thermal conductivity, and c_p is the specific heat capacity, and ρ_l the liquid density. The Jakob number Ja, is the ratio of sensible heat to latent heat, given by $Ja = \rho_l c_p \Delta T_0/\rho_v h_{lv}$, where ΔT_0 is the initial liquid superheat, and h_{lv} is the enthalpy of vapourisation. These tests were later repeated for a range of other fluids (Dergarabedian, 1960), showing similar good agreement with the theory.

Further experimental tests of bubble growth at reduced pressure were later carried out by Lien (1969). These experiments generated bubbles using electrodes to induce catalysis, which can disturb the formation of the thermal boundary layer in the early stages of growth, but showed good agreement with the existing theories in the later stages of growth. Florschuetz et al. (1969) investigated the effect of gravity on the growth rates of bubbles of various fluids, using an experimental setup in free-fall to provide a zero gravity testing environment.

Accounting for the inertial limiting velocity, Mikic et al. (1970) interpolated between inertial limit given by equation (1.2) and the thermal limit from equation (1.5), giving the MRG model:

$$\dot{R}_{\mathrm{MRG}} = A\left[\sqrt{\frac{A^2}{B^2}t + 1} - \sqrt{\frac{A^2}{B^2}t}\right], \tag{1.6}$$

with A given by equation (1.2) and $B = Ja\sqrt{12\alpha/\pi}$.

Further testing by Board and Duffey (1971) showed excellent agreement with the MRG model and demonstrated that the theory can be generalised to other fluids, in their case, water being used to predict the growth of sodium bubbles. Theofanous and Patel (1976) later showed that there is some predictive error in the theory when the mass ratio of the vapour at the initial and final temperature is large.

Consistently producing and detecting homogeneous vapour bubbles can be quite challenging experimentally. The reduced nucleation energy barrier on solid surfaces requires careful consideration when designing experimental setups. Additionally, due to the stochastic nature of homogeneous nucleation, it is not possible to predict exactly where and when vapour bubbles will form, which makes obtaining high-resolution measurements of bubble growth rates difficult. Due to the complex experimental conditions required for the measurement of vapour bubbles, researchers have taken to a variety of computational techniques to investigate bubble growth. The increasing availability of computational resources has made performing highly resolved numerical simulation of vapour bubbles more achievable (Allen & Tildesley, 2017; Carey, 2018). This has allowed for vapour bubbles to be studied at time and length scales not currently feasible experimentally.

Dalle Donne and Ferranti (1975) directly coupled the Rayleigh–Plesset (equation (1.1)) and energy (equation (1.4)) equations to model the growth of sodium bubbles, showing good agreement with experimental data. This approach was later adapted by Prosperetti and Plesset (1978), who used the thin thermal boundary layer approximation of Plesset and Zwick (1954) instead of the complete energy equation. The numerical results compared well with the results of Dalle Donne and Ferranti (1975), indicating the validity of this approximation. These results also showed good agreement with the MRG model (Mikic et al., 1970), provided the bubble had grown sufficiently so that capillarity

no longer played a significant role in determining the growth dynamics. This approach of coupling the RP and Energy equations has been adopted by many other authors (Bardia & Trujillo, 2019; H. S. Lee & Merte, 1996; Prosperetti, 2017; Robinson & Judd, 2004), showing similar good agreement with experimental results and the MRG model.

While these numerical investigations have highlighted the wide applicability of the PZ and MRG models, the improved spatial and temporal resolution has also revealed some of the limitations of these models. The existing models have been shown to overpredict the early stages of bubble growth (Prosperetti, 2017). For small bubbles, capillarity and viscosity, which are not accounted for in the PZ and MRG models, play a significant role in determining the bubble dynamics. To obtain a complete understanding of the process of vapour bubble growth, these effects must be included in the models. In chapter 3, the role of inertia in the early stages of bubble growth is investigated, and a new class of inertio-thermal bubble growth models is developed. These models capture the early stage behaviour of vapour bubbles, including the capillary and viscous effects which have thus far been neglected.

1.2.2 Heterogeneous Bubble Growth

While studying homogeneous bubbles is useful to understand the physics of the general problem of bubble growth, in practice, bubbles typically form and grow heterogeneously, while attached to a solid surface. Most industrial applications will, therefore, require knowledge of the role of the surface on bubble growth behaviour.

The role of buoyancy in determining the lifetime of heterogeneous bubbles is widely studied experimentally (Carey, 2018). The timescale at which buoyancy forces overcome capillarity and detach bubbles from the surface is relevant to determining the maximum heat transfer rate obtainable in boiling systems. In part due to the dominance of buoyancy effects, there is less understanding of the role of surface wettability on the growth behaviour of vapour bubbles. While some work has investigated the effects of wettability in the departure of vapour bubbles (Phan et al., 2010), the effect on the growth rate must currently be inferred from the departure behaviour. A model for heterogeneous vapour bubble growth rates based on a knowledge of the departure time was developed by van Stralen et al. (1975). While they did show good agreement with experimental results (H. C. Lee et al., 2003; van Stralen et al., 1975), the model requires knowledge of the bubble's initial and final state, only including the effect of wettability if it is included in the calculation of departure time.

Robinson and Judd (2001) showed good agreement between their experimental data and model for hemispherical bubble growth, where symmetry allows for spherical bubble growth models to be used. Similarly, Mikic et al. (1970) predicted the growth of spherical bubbles near a heated surface, by accounting for the non-uniform temperature field.

Enríquez et al. (2014) have shown that the presence of a solid surface has a significant effect on the diffusion-limited growth of bubbles[1], but this effect is yet to be fully characterised for thermally-limited vapour bubble growth. This is complicated by the formation of a liquid microlayer underneath growing vapour bubbles, that provides a significant contribution to the heat transfer from the surface (Cooper & Lloyd, 1969; Gerardi et al., 2010; Zou et al., 2016).

When attempting to numerically analyse heterogeneous vapour bubble growth, direct couplings of the Rayleigh–Plesset (equation (1.1)) and energy (equation (1.4)) are not possible as the spherical symmetry assumed in the RP equation is no longer applicable. This means that an analytical approach is challenging, and therefore numerical methods have been widely used. A variety of techniques have been developed to numerically model the growth of heterogeneous bubbles. Volume of fluid approaches have been used in many investigations, such as by Mukherjee and Kandlikar (2007), who used a level-set technique to track the bubble interface, while Mirsandi et al. (2018) adopted a local front-reconstruction method. Alternative numerical approaches have been adopted to solving the Navier–Stokes and energy equations. There have been investigations into the effects of surface roughness and wettability on the growth of bubbles using the lattice Boltzmann method (Chang et al., 2019; Gong & Cheng, 2012; Mu et al., 2017). Other numerical techniques showing promise include smooth particle hydrodynamics (Joshi et al., 2019) and weighted particle solutions to the Enskog–Vlasov equation (Busuioc et al., 2022).

While some work has been done on analysing low Bond number bubble growth (Lesage et al., 2014; Robinson & Judd, 2001), most numerical studies into heterogeneous vapour bubble growth focus on the growth and detachment the bubbles due to buoyancy effects. This leaves open the question of how the bubbles grow when buoyancy does not dominate, i.e. for bubble radii smaller than the capillary length scale. This is most relevant to the early stages of bubble growth, when bubbles are smaller and capillary effects more dominant. Chapter 4 investigates how heterogeneous vapour bubbles grow on surfaces of varying wettability. By accounting for the change in geometry of the bubble, the models developed in chapter 3 are adapted to account for the altered thermal diffusion in the surrounding liquid due to the presence of the wall.

---

1. These experiments investigated the effect of the surface on species diffusion, however we can apply the findings to thermal diffusion by similitude

1.3 Bubble Nucleation

Nucleation is the process by which a new phase forms from an energetically unfavourable state. This can be the condensation of liquid droplets, the solidification of solid crystals, or, most relevant to this work, the formation of vapour bubbles. Understanding the mechanisms by which bubbles form, i.e. *nucleate*, can give us an insight into the key physics relevant to vapour bubbles that will be important throughout this work.

Nucleation theory can be broken into the thermodynamics and the kinetics of nucleation. The thermodynamic aspect of nucleation theory explores the energetic barrier to nucleation, determining the free energy change associated with the formation of a cluster, and the transition from the old phase to the new phase. Nucleation kinetics refers to the mechanisms by which these clusters form and grow, and explores the rate at which nucleation events can be expected to occur. These two areas will be discussed in further detail below, particularly in the context of vapour bubbles, where some extra considerations are needed.

1.3.1 Nucleation theory

Nucleation as a phenomenon is dependant on two competing effects: a material existing in an energetically unfavourable phase, and an energy barrier to creating a new phase boundary. In order for the material to move from the old, energetically unfavourable phase to the new one, an initial seed, or nucleus, must form. Whether this nucleus grows into the new phase or collapses back into the old phase is dependant on the balance between these two effects (Kaschiev, 2000).

The driving force for nucleation is the difference between the chemical potential of a molecule in the old and new phases, termed the supersaturation $\Delta\mu$. In the context of vapour bubbles formed by boiling, this driving force is often expressed in terms of superheat ΔT, the difference between the fluid temperature T and the saturation temperature T_{sat}. Due to the practical convenience of performing experimental tests at atmospheric pressure, this provides a simple and easily measurable way to analyse the driving force. For the analysis of bubbles, the driving force is typically given in terms of the fluid underpressure ΔP, the difference between the pressure in the fluid P_∞ and the fluid's vapour pressure P_v, i.e. $\Delta P = P_v - P_\infty$. The supersaturation associated with the formation of a vapour bubble can be determined by taking the difference between the free energies of the fluid in the vapour and liquid states:

$$\Delta\mu = k_B T \ln\left(\frac{P_v}{P_\infty}\right) - v_0\left(P_v - P_\infty\right), \tag{1.7}$$

where k_B is the Boltzmann constant, T is the temperature of the fluid, and v_0 is the molecular volume. Typically $k_BT \gg v_0\Delta P$ and the second term can be disregarded (Kaschiev, 2000).

The barrier to the formation of a new phase arises from the additional free energy required to form the interface between the two phases. This interfacial excess energy γ arises from the force anisotropy experienced by the molecules at the interface (de Gennes et al., 2004; Israelachvili, 2011). In the case of a liquid interface with it's own vapour, this excess energy is often referred to as *surface tension*, as it is indistinguishable from the interfacial stress (Di Pasquale & Davidchack, 2020).

Taking the difference between the barrier resisting nucleation and the energetic driving force, the change in Gibbs free energy ΔG associated with the formation of a nucleus can be given as (Kaschiev, 2000):

$$\Delta G = -n\Delta\mu + \gamma A, \tag{1.8}$$

where n is the number of molecules in the nucleus and A is the interfacial area. In the case of vapour bubbles, it is often more useful to express the Gibbs free energy in terms of pressure difference (Carey, 2018; Kaschiev, 2000). For the case of a spherical vapour nucleus the Gibbs free energy $\Delta G(R)$ change is expressed in terms of the radius as (Kaschiev, 2000):

$$\Delta G(R) = -\frac{4}{3}\pi R^3\Delta P + 4\gamma\pi R^2. \tag{1.9}$$

This expression gives a clearer picture of the relationship between the change in Gibbs free energy and the size of the nucleus. For large nuclei, the volumetric supersaturation term dominates as it scales with R^3. In these cases, it is energetically favourable for the nucleus to grow indefinitely. Meanwhile, for small nuclei, the surface area term dominates as it scales with R^2. Here, it is energetically favourable for the nucleus to shrink, reducing the interfacial surface area, despite the supersaturation.

This means there is a critical value of nucleus radius R_c above which it is energetically favourable for the nucleus to grow, and below which it is favourable for it to shrink. This can be seen qualitatively in the plot in figure 1.2 which visualises how the Gibbs free energy changes with radius. The energy barrier that must be overcome (ΔG_c) is the value of the change in free energy of a critically sized nucleus. We can obtain an expression for the critical radius by finding the location of the maximum of equation (1.9) by setting the first derivative with respect to R as 0:

$$R_c = \frac{2\gamma}{\Delta P} \tag{1.10}$$

Notably, this expression is identical to the Young-Laplace equation, relating the pressure change across a curved interface to its radius of curvature. This shows that in order for a nucleus to grow, the pressure difference ΔP must exceed the Laplace pressure.

In the case of heterogeneous nuclei, the same analysis can be used. However, the volume and surface area terms must be scaled to account for the change in geometry of the nucleus. For spherical cap shaped nuclei the free energy of the nucleus becomes a function of both the radius and contact angle θ_v. In addition the interfacial free energy between the nucleus and surface must be considered in the calculations. This results in a scaling of the free energy by a factor of:

$$\psi(\theta_v) = \frac{(2 + \cos\theta_v)(1 - \cos\theta_v)^2}{4}. \tag{1.11}$$

This factor ψ always takes a value between 0 and 1 and is equivalent to the scaling factor of the volume of a spherical cap to the sphere of the same radius. This shows that the energy barrier associated with the formation of a heterogeneous nucleus is always lower than a homogeneous nucleus at the same supersaturation. This can be seen in figure 1.2, which shows that ΔG_c for a homogeneous nucleus is greater than for a heterogeneous nucleus. Accounting for the effect of the modified bubble geometry on the Gibbs free energy associated with the supersaturation and creation of the liquid-vapour and vapour-solid interfaces, equation (1.9) can be rewritten for heterogeneous nucleation as (Kaschiev, 2000):

$$\Delta G(R, \theta_v) = \frac{(2 + \cos\theta_v)(1 - \cos\theta_v)^2}{4}\left(-\frac{4}{3}\pi R^3 \Delta P + 4\gamma\pi R^2\right). \tag{1.12}$$

Finding the location of the maximum of equation (1.12) by differentiating again returns the Young-Laplace equation, indicating that the critical radius is identical for homogeneous and heterogeneous nuclei. However, the value of the free energy barrier is reduced by $\psi(\theta_v)$. Additionally, equation (1.9) shows that ΔG_c is lower for low values of θ_v. This matches experimental observations, where vapour bubbles form at lower superheats on less wetting surfaces (Carey, 2018; Chu et al., 2013).

1.3.2 Surface Effects on Nucleation

From the theoretical analysis above it is clear that surface wettability plays a significant role in determining heterogeneous nucleation behaviour. However, there is generally less interest in determining the heterogeneous nucleation limit of surfaces than for homogeneous nucleation. This is largely due to the presence of active sites for nucleation on the surface, which significantly reduce the barrier to nucleation (Carey, 2018; Kaschiev, 2000). Experimental investigations into pool boiling heat transfer have shown that

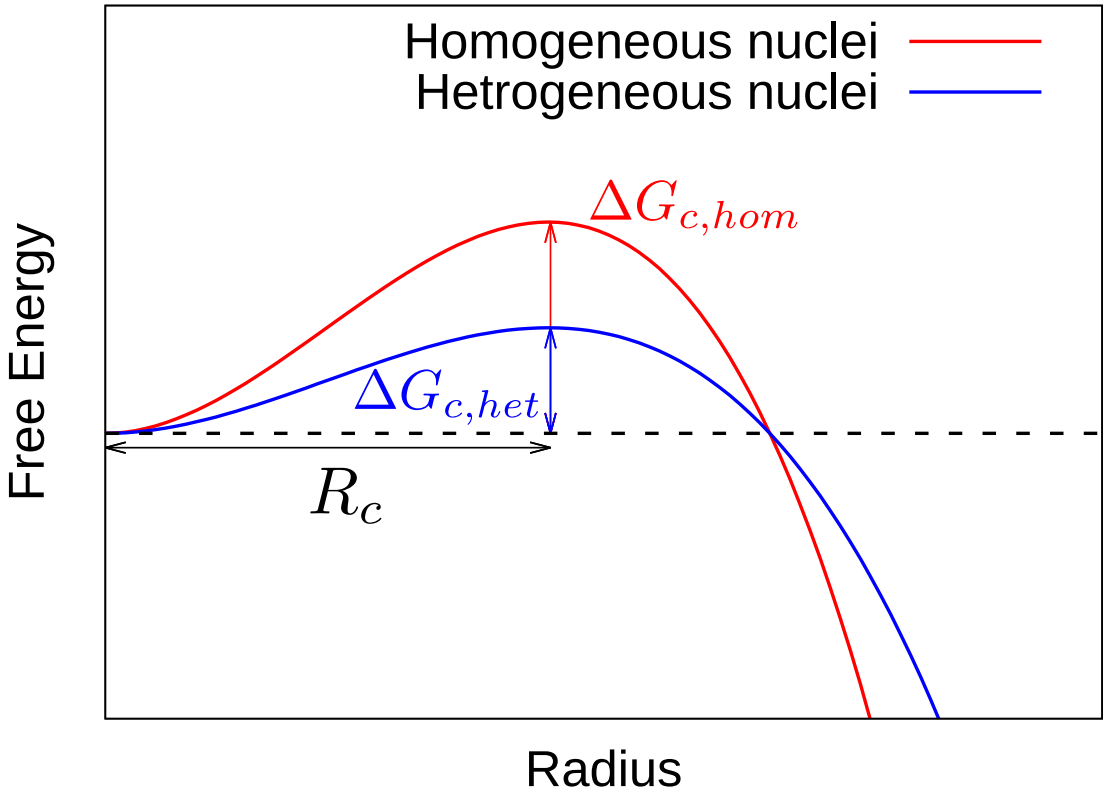

Figure 1.2: Illustration of change in Gibbs free energy of a nucleus of a given radius. The maximum value of free energy ΔG_c is lower for heterogeneous nuclei, but the critical radius R_c is equal for both homogeneous and heterogeneous nuclei

nucleation occurs at lower superheats on hydrophobic surfaces (Bourdon et al., 2013, 2012), in line with the predictions of CNT. However, due to the presence of active sites for nucleation on experimental surfaces, the exact dependence of nucleation temperature on wettability cannot be easily measured. In order to obtain accurate comparisons against theory, atomically smooth surfaces must be used.

Due to the importance of active sites in encouraging the formation of vapour bubbles, significant investigation has been performed into the effect of surface roughness on the onset of nucleate boiling (Carey, 2018). Early work by Lorenz et al. (1974) showed how the presence of surface roughness can cause gas pockets to become trapped on the surface, providing preferential sites for nucleation on the surface, significantly reducing the superheat required for boiling. A variety of surfaces have been designed to promote nucleation by providing locations for the entrapment of gases on the surface. Chu et al. (2013) developed surfaces with hierarchical roughness, at both the micro- and nano-scales, to increase heat transfer performance. Ujereh et al. (2007) observed nucleation at lower superheats on surfaces coated with a layer of carbon nanotubes. Similar investigations have been performed for copper and silicon nanowire arrays (R. Chen et al., 2009; Shi et al., 2015), showing a decreased superheat for nucleation. Nanoporous copper and alumina surfaces have been shown to significantly enhance the formation of vapour bubbles (Lu et al., 2016; Vemuri & Kim, 2005). One of the outstanding issues in these investigations is decoupling the change in wettability and change in roughness (Kim et al., 2011), which can be difficult to achieve experimentally.

The predictions of CNT are tested in chapter 5, where the role of surface wettability and morphology on the nucleation of vapour bubbles is investigated. By using atomically smooth surfaces, the effect of wettability is completely isolated and directly compared to CNT. The effect of surface roughness on the formation of active sites is then investigated, and compared to CNT and the Lorenz et al. (1974) model of vapour trapping.

1.4 Nucleation and Growth of Vapour Bubbles

The theoretical analyses shown in section 1.2 show that there is still a gap in the understanding of the early stages of vapour bubble growth. While descriptions exist of both inertially- and thermally-controlled growth, there is currently little understanding of the interplay between inertial and thermal effects shortly after nucleation. This is further complicated by the preference for heterogeneous nucleation. The presence of the solid surface has been shown to affect diffusive bubble growth due to the breaking of spherical symmetry (Enríquez et al., 2014). Additionally, the layering of molecules near the solid surface and associated adsorbed layer underneath vapour bubbles have not been accurately captured by continuum techniques. The effect of this non-evaporating

layer on the interfacial stress balance governing the shape of vapour bubbles has only recently been investigated using a continuum approximation (Ardron & Giustini, 2021), with much still to understand on the role of wettability in the formation of the layer. Understanding the effect of this layer on the nucleation and growth of vapour bubbles therefore remains an open question.

In summary, the key objectives of this thesis can be summarised as:

1. to understand the interplay between the inertial forces driving the growth of vapour bubbles and the limiting thermal diffusion. Chapter 3 presents a new class of inertio-thermal vapour bubble growth models to better capture the early stages of growth;
2. to investigate the effect of a surface on the growth rate of vapour bubbles. Chapter 4 demonstrates the role of surface wettability on the available thermal diffusion and on the formation of the non-evaporating layer that has been observed on hydrophilic surfaces;
3. to determine the effect of surface wettability and morphology on the nucleation of vapour bubbles. Chapter 5 investigates if the change in interfacial stress and presence of surface cavities cause deviations from classical nucleation theory.

Chapter 2

Simulation Methodology

2.1 Molecular dynamics simulation

Molecular dynamics is a high-fidelity deterministic simulation method which integrates Newton's equations of motion for each molecule in systems of many molecules (Allen & Tildesley, 2017). It differs from continuum fluid dynamics models in that MD tracks the positions of individual molecules in the system rather than solving for continuum approximated properties. This does however restrict MD simulations to smaller systems, typically of order nanometers, for short periods of time, on the order of nanoseconds, due to the high computational cost of tracking every molecule position over time. In this work, all MD simulations are performed using the open source software LAMMPS (Plimpton, 1995).

2.2 Molecular potentials

In order to determine the forces required to calculate the dynamics of the system, the interaction between each molecule must be defined. The interactions between molecules are typically broken down into dispersive (e.g. van der Waals) and electrostatic (Coulombic) interactions (Israelachvili, 2011). The dispersive interactions are typically captured by the Lennard-Jones (LJ) 12-6 potential (Lennard-Jones, 1924), given as:

$$U(r_{ij}) = 4\epsilon_{ij}\left[\left(\frac{\sigma_{ij}}{r_{ij}}\right)^{12} - \left(\frac{\sigma_{ij}}{r_{ij}}\right)^{6}\right], \tag{2.1}$$

where σ is the characteristic length scale, ϵ is the potential well depth, and r is the distance between two molecules, denoted by the subscripts i and j. The form of the equation captures the attractive $r^{-1/6}$ relation from van der Waals interactions (Israelachvili, 2011). The repulsive $r^{-1/12}$ component is used for computational efficiency as it closely matches the repulsive behaviour and can be easily computed by squaring the $r^{-1/6}$ term rather than performing a separate calculation, such as in the Buckingham potential,

which uses an exponential function to model repulsive interactions (Allen & Tildesley, 2017). The fluid interaction parameters used in these simulations are $\sigma = 0.34\,\text{nm}$ and $\epsilon = 0.2392\,\text{kcal/mol}$, respectively, which were chosen to model argon (Maroo & Chung, 2008).

The force, $\vec{F}_{ij}$, experienced by each molecule in the pair is given by the gradient of the potential,

$$\vec{F}_{ij} = -\nabla \vec{U}_{ij}. \tag{2.2}$$

The future positions and velocities of each molecule in the system is calculated by performing the velocity Verlet integration scheme (Verlet, 1967). The simulations in this thesis are performed with a timestep of 5 fs.

In order to improve the computational efficiency of the simulations, the potential is truncated for values of $r > r_{\text{cut}}$, where $r_{\text{cut}} = 1.3\,\text{nm}$ for these simulations. Additionally the value of the potential is shifted by the value at the cutoff in order to maintain a continuous value of the potential. The potential is then given by:

$$U(r_{ij}) = \begin{cases} 4\epsilon_{ij}\left[\left(\frac{\sigma_{ij}}{r_{ij}}\right)^{12} - \left(\frac{\sigma_{ij}}{r_{ij}}\right)^{6} - \left(\frac{\sigma_{ij}}{r_{\text{cut}}}\right)^{12} + \left(\frac{\sigma_{ij}}{r_{\text{cut}}}\right)^{6}\right] & r \leq r_{\text{cut}} \\ 0 & r > r_{\text{cut}} \end{cases}, \tag{2.3}$$

Calculating these pair potentials is the most computationally expensive part of MD simulations. As there is no interaction between molecules outside the cutoff distance, attempting to compute these pair potentials is redundant. Neighbour lists are used to reduce the number of molecules on which pair calculations are attempted to be performed. The neighbour list for a molecule consists of all other molecules within a given distance, typically the cutoff distance plus a small skin distance. Only molecules within this radius are investigated for pair calculations, rather than every molecule in the system (and their periodic images). The lists are updated periodically to ensure relevant interactions are not missed. The frequency of these updates is dependant on the specified value of the skin distance; a greater skin distance means fewer pair calculations are performed each timestep, but needs a greater frequency of updating the neighbour lists. The pairwise interactions are only calculated for the molecules on the neighbour list, rather than every molecule in the system, greatly reducing the computational cost of the simulation.

2.3 Thermodynamic quantities

As MD tracks the properties of individual molecules rather than spatial averages, statistical mechanics must be used to extract thermodynamic data from the system (Allen & Tildesley, 2017). Macroscopic system properties such as temperature and pressure are calculated from time averages of the system's microscopic properties to reduce the statistical uncertainty in the measurements. Ergodic theory tells us that this time average is equivalent to the ensemble average (Hill, 1956), allowing for the time average of a single system, rather than an ensemble of systems be used to compute ensemble properties.

2.3.1 Temperature

The temperature of a molecular system is a measure of the average molecular kinetic energy. For a system of N molecules, the total translational kinetic energy E_k can be given as:

$$E_k = \sum_i^N \frac{1}{2} m_i {v_i}^2 = \frac{3N}{2} k_B T, \tag{2.4}$$

where v is the absolute velocity of each molecule, m is the mass of the molecule, and k_B is the Boltzmann constant. This expression can then be rearranged to give an expression for temperature that can be computed from a molecular simulation:

$$T = \sum_i^N \frac{m_i {v_i}^2}{3N k_B}. \tag{2.5}$$

2.3.2 Pressure

The pressure of a molecular system can be calculated through the stress tensor $\overleftrightarrow{\tau}$, which for a system of volume V with N molecules is calculated as:

$$\overleftrightarrow{\tau} = \frac{1}{V} \left\langle \sum_i^N m_i \vec{v}_i \otimes \vec{v}_i + \sum_i^N \sum_{j<i}^N \vec{r}_{ij} \otimes \vec{f}_{ij} \right\rangle, \tag{2.6}$$

where m is the mass of each molecule, $\vec{v}_i$ is the velocity of molecule i, $\vec{r}_{ij}$ represents the displacement of the molecules i and j, and $\vec{f}_{ij}$ is the force the molecules exert on each other. The angle brackets $\langle\rangle$ represent the ensemble average. The term on the left hand side of equation (2.6) is the kinetic pressure, due to the motion of the molecules. The term on the right hand side is the virial pressure, which is due to the intermolecular forces. In a gas, the kinetic pressure term typically dominates as molecules are further

apart and there is often negligible intermolecular interaction. In liquids meanwhile, there is a greater contribution from the virial term, as molecules are more densely packed (Parker, 1954). The pressure of the system can be determined by taking the negative trace of the stress tensor, i.e.:

$$P = -\frac{\text{trace}\left(\overleftrightarrow{\tau}\right)}{3} = -\frac{\tau_{xx} + \tau_{yy} + \tau_{zz}}{3} \tag{2.7}$$

2.4 Thermodynamic ensembles

Thermodynamic ensembles describe the collection of microscopic system states, i.e. configurations of molecules, that correspond to the same macroscopic state, i.e. systems with the same values of thermodynamic properties such as temperature, pressure, and density. When molecular simulations are performed, the particles' dynamics are typically controlled such that they, on average, match those of a particular ensemble. Typically these ensembles look to keep some of the following system properties constant: volume, temperature, pressure, and energy. While not an exhaustive list, the following are some of the most commonly used thermodynamic ensembles:

2.4.1 Microcanonical ensemble (NVE)

The microcanonical ensemble consists of a constant number of molecules, system volume, and system energy. For this reason it is often referred to as the NVE ensemble. This corresponds to an isolated system, one where there is no mass or energy transfer in or out of the system. The ergodic hypothesis states that all microstates of these systems occur with equal probability over time, meaning that the time average of the thermodynamic properties of the system are identical to the average over the ensemble (Hill, 1956).

2.4.2 Canonical ensemble (NVT)

The canonical ensemble represents a closed system coupled to an external temperature reservoir. The number of molecules, system volume, and temperature of the system are kept constant. Due to the constant temperature (in place of constant energy in NVE) this is also called the NVT ensemble.

In numerical simulations, the temperature is maintained using a "thermostat", an algorithm that adjusts the velocities of the system molecules to ensure a constant average kinetic energy. The simplest thermostat scales the velocity of all molecules equally such that the target temperature value from equation (2.5) is achieved. Other examples of thermostats include the Berendsen thermostat, which couples the molecules

to a thermal reservoir (Berendsen et al., 1984), the Langevin thermostat, which applies a stochastic damping force to the molecules to achieve the target temperature (Schneider & Stoll, 1978), and the Andersen thermostat, which randomly changes molecule velocities to fit a Maxwell–Boltzmann distribution (Andersen, 1980).

The thermostat used in this work is the Nosé–Hoover thermostat, which couples the system to a virtual mass to ensure a constant temperature. This is implemented in LAMMPS through the *fix nvt* command, and includes time integration of the molecules. The thermostat is used for performing isothermal simulations and for equilibrating systems prior to non-equilibrium measurements.

2.4.3 Isothermal-isobaric ensemble (NPT)

The isothermal-isobaric ensemble consists of a system held at constant temperature and pressure, representing a closed system coupled to a temperature reservoir where boundary work can be performed. It is also known as the NPT ensemble and implemented in LAMMPS through the *fix npt* command. The volume of the system is no longer constant, and is adjusted by a barostat to maintain the target system pressure.

While this ensemble has been used to investigate CNT of homogeneous vapour bubbles (Rosales-Pelaez et al., 2019), it is not suitable for measuring heterogeneous bubbles due to the interaction of the barostat with the solid surface. As barostats are applied to the entire system volume, stresses in the solid will affect the ability of the barostat to accurately control system pressure, and provide inaccurate results in the fluid. In order to achieve an NPT ensemble in this work, a piston is used to control the system pressure. This is discussed in further detail in section 2.7.

2.5 Model validation

The LJ interaction parameters used to model argon listed in section 2.2 are taken from literature. In order to confirm the accuracy of the potential used, benchmark simulations are performed to validate the model (Maroo & Chung, 2013). The key thermodynamic properties of the fluid are compared to those of argon and of reference values for the pure LJ fluid.

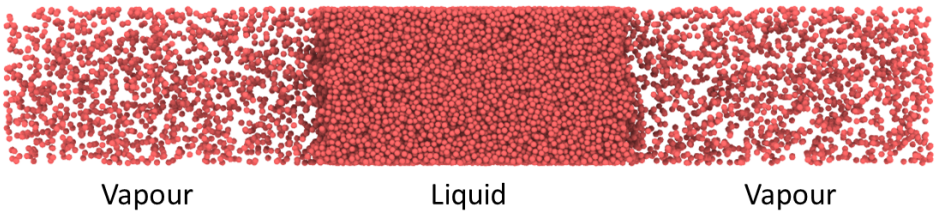

Figure 2.1: Liquid-vapour equilibrium simulation setup for the measurement of saturation properties

2.5.1 Saturation Properties

Vapour bubble formation and growth is an inherently multiphase problem. Therefore, the saturation properties of the fluid are of significant importance. The saturation properties of the fluid are measured from equilibrium simulations of a liquid-vapour system. The simulation setup is shown in figure 2.1, consisting of a liquid slab of length 20 nm held at constant temperature in equilibrium with its own vapour. The simulation domain size is 10 nm 10 nm $\times$ 60 nm. The properties of both the liquid and vapour regions can then be measured from these simulations.

Density

Density is calculated separately in the liquid and vapour regions by measuring the number of molecules per unit volume in the liquid and vapour regions of the setup in figure 2.1. Figure 2.2 shows excellent agreement of the MD simulation data with the vapour pressure data of the LJ fluid obtained from NIST (Johnson et al., 1993). There is also good agreement with the NIST data for argon obtained from REFPROP (Lemmon et al., 2018). There is some deviation seen between the LJ and argon values at high reduced temperatures. This is due to the choice of LJ interaction parameters, which is designed to provide a good fit for temperatures below the critical value.

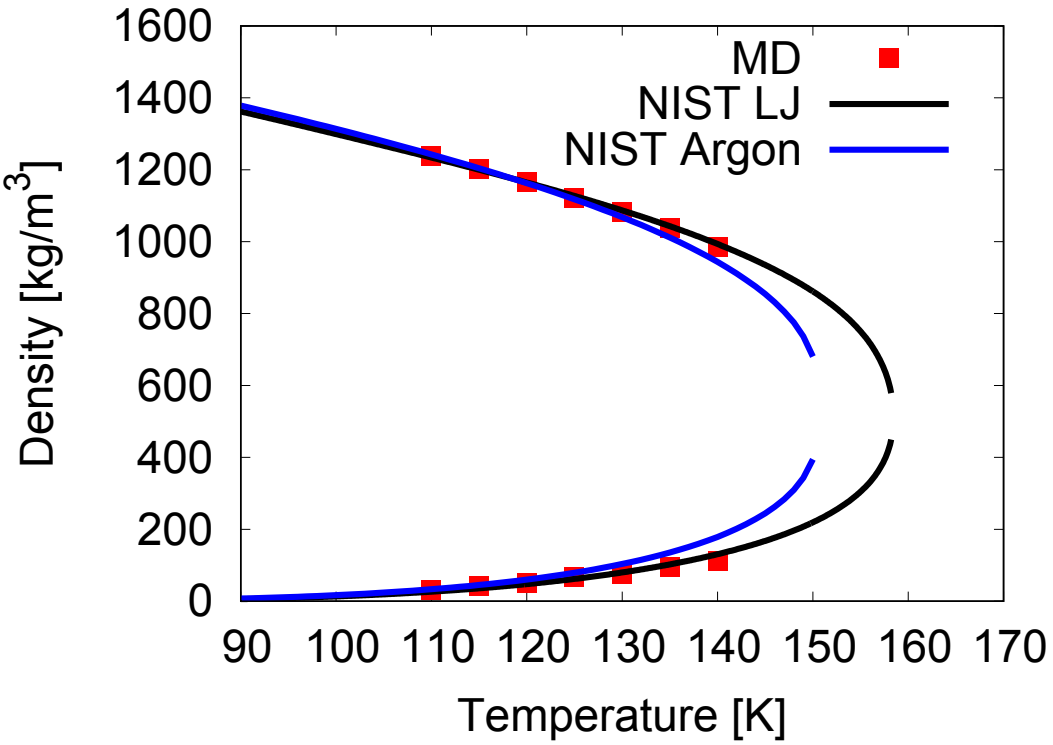

Figure 2.2: Comparison of vapour pressure measurements from MD simulation to the vapour pressure of argon and the LJ fluid. Both reference curves are obtained from NIST.

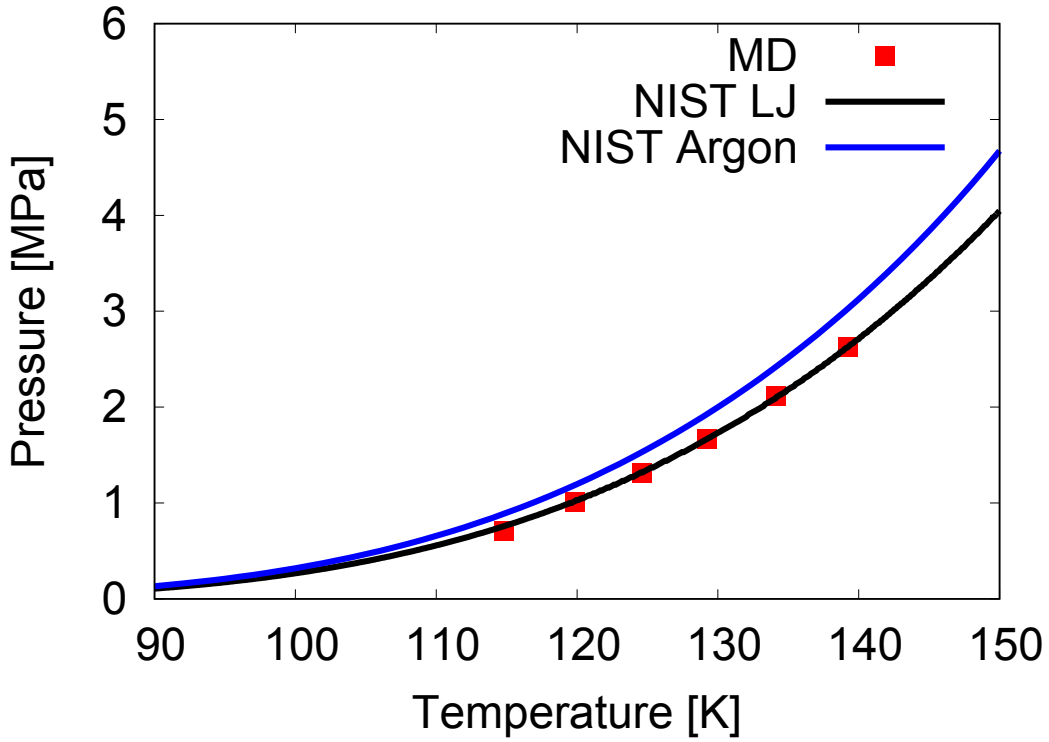

Figure 2.3: Comparison of vapour pressure measurements from MD simulation to the vapour pressure of argon and the LJ fluid. Both reference curves are obtained from NIST.

Vapour Pressure

The vapour pressure for the system can be calculated using equation (2.7), with the simulation results shown in figure 2.3. Again we see good agreement of the MD simulation data with the NIST data for both the LJ fluid. There is a slight underprediction of the data for pure argon, with the disagreement increasing with temperature.

2.5.2 Surface Tension

Surface tension is a measure of the excess free energy associated with the creation of a phase interface. This is caused by the imbalance of forces experienced by molecules at the interface. Following the methodology from Yamaguchi et al. (2019) and Nishida et al. (2014), the liquid-vapour interfacial stress γ_{lv} is calculated as the integral of the difference of the normal τ_N and tangential τ_T pressure components in the direction normal to the interface from a location in the bulk liquid y_l to one in the bulk vapour y_v:

$$\gamma_{lv} = \int_{y_l}^{y_v} (\tau_N - \tau_T) dy, \tag{2.8}$$

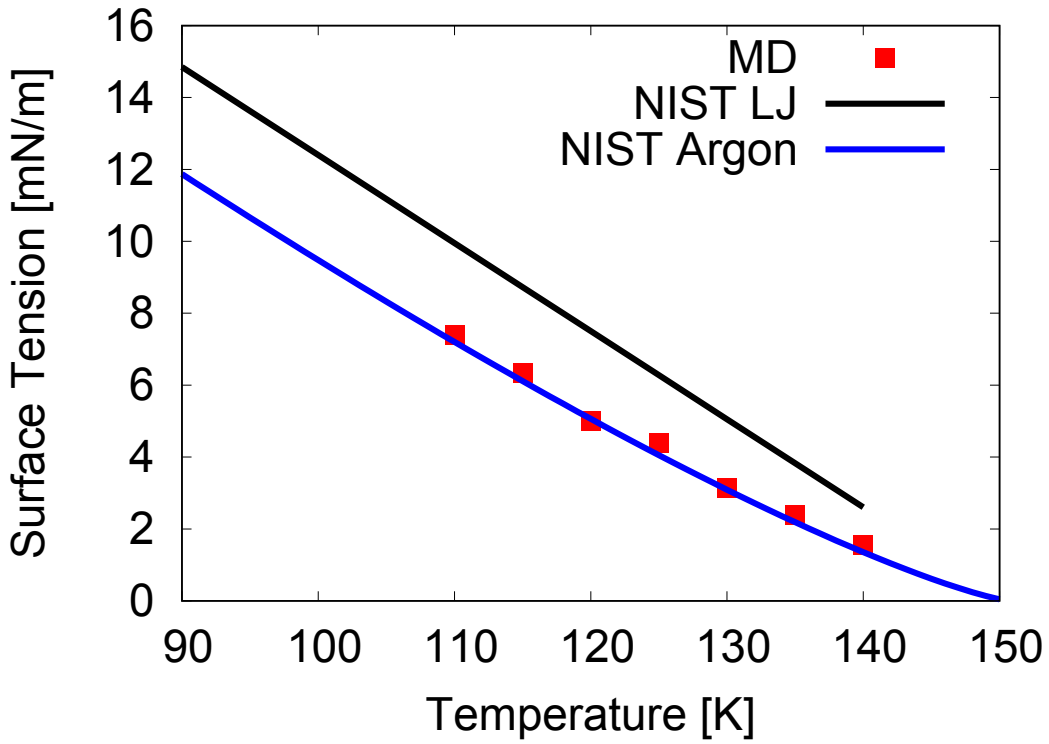

Figure 2.4: Comparison of surface tension measurements from MD simulation to the values of argon and the LJ fluid. Both reference curves are obtained from NIST.

where formally, $\tau_N = \overleftrightarrow{\tau} N$ and $\tau_T = \overleftrightarrow{\tau} T$, where $\vec{N}$ and $\vec{T}$ represent the normal and tangential vectors.

The equation for the stress tensor in a finite segment of fluid can be given as a modified version of equation (2.7):

$$\overleftrightarrow{\tau} = \frac{1}{V}\left\langle \sum_{i \in V} m_i v_i \otimes v_i + \sum_{i}^{N} \sum_{j<i}^{N} w_{ij} r_{ij} \otimes f_{ij} \right\rangle, \tag{2.9}$$

where w_{ij} represents the proportion of the distance between the two molecules that passes through the volume. These values are then numerically integrated in the direction normal to the interface to compute the surface tension. The results of the MD simulation compared to the reference values for argon and the LJ fluid are shown in figure 2.4. There is excellent agreement seen between the measured values and the NIST values for pure argon. There is however, a noticeable underprediction of the NIST LJ values. This is likely due to the effects of the cutoff length chosen in this work. Here, a cutoff of 1.3 nm was used, equivalent to 3.8σ. The full surface tension of LJ argon is not achieved until a cutoff length of approximately 3nm (Méndez-Bermúdez et al., 2022) with shorter cutoff lengths producing lower values of surface tension.

For the solid-liquid and solid-vapour interfaces, only the difference between the two values is needed, and it is simpler to measure the interfacial stress relative to a bare surface. In these cases the lower bound of the integral is adjusted to be the fluid-solid interface y_{sf} (Yamaguchi et al., 2019). The expression is given as the difference between the interfacial stress γ_{sf} and the bare surface γ_{s0}:

$$\gamma_{sf} - \gamma_{s0} = \int_{y_{sf}}^{y_f} (\tau_N - \tau_T) dy. \tag{2.10}$$

Note that as the difference between solid-liquid and solid-vapour interfacial stresses is the parameter of interest in this study (i.e. $\gamma_{sl} - \gamma_{sv}$), the bare surface term is not needed to be calculated as:

$$\gamma_{sl} - \gamma_{sv} = \int_{y_{sl}}^{y_l} (\tau_N - \tau_T) dy - \int_{y_{sv}}^{y_v} (\tau_N - \tau_T) dy. \tag{2.11}$$

2.6 Domain Setup

The simulation setup used across the MD investigations performed in this thesis consists of a liquid slab bounded by two rigid face-centred cubic (FCC) walls, one of which has its wettability or geometry altered when investigating heterogeneous bubbles and is fixed in place, while the second is allowed to translate in the normal direction after fluid equilibration. The other boundaries of the domain are periodic. The liquid slab was created using the software package Packmol (Martínez et al., 2009), with the dimensions of the slab chosen depending on the investigation being performed. The number of liquid molecules was chosen to be slightly lower than the saturation density, creating a supersaturated liquid (e.g. $\rho_l = 1000\text{kg/m}^3$ less that the saturation density of 1068kg/m^3 for $T = 130\,\text{K}$).

The liquid is initially equilibrated (with both surfaces fixed) in the NVT ensemble until the potential energy reached a steady value. The piston is then released to apply the required pressure, which will be described in section 2.7. The system was equilibrated again in the NVT ensemble until the piston reached a steady position, at which point the damping was removed from the piston. The general simulation setup is shown in figure 2.5, with the differences between simulation procedures highlighted below.

Homogeneous Bubble Growth:

For the homogeneous bubble growth simulations (chapter 3), a cube of 60 nm side length was used as the fluid domain. This size was chosen as it prevented the thermal boundary layer, of size $\delta = \sqrt{\alpha t}$ where α is the thermal diffusivity of the liquid and t is the time the bubble has been growing, from extending beyond the periodic boundaries within

the time-frame of the bubble growth simulations. A smaller size was not suitable for the bubble growth investigations as it would not allow for the bubble to grow sufficiently to clearly see a departure from existing theories. A sphere of molecules was removed from the centre of the simulation domain. A smaller number of vapour molecules were then inserted into this void, with the number of molecules set to match the saturated vapour density. This system was then run with the fluid in the NVT ensemble for 1000 timesteps, performing this step helped to prevent any cavitation bubbles from forming in the bulk liquid. The production simulations could then be performed with the fluid in the NVE ensemble. These simulations were run for a total of 200,000 timesteps, or 1 ns.

Heterogeneous Bubble Growth:

For the heterogeneous bubble growth simulations (chapter 4), the size of the domain was altered depending on the expected contact angle of the bubble. The dimensions ranged from a height of 45 nm and length of 60 nm for the most wetting cases, to a height of 20 nm and length of 70 nm for the least wetting cases. A spherical cap (chapter 4) of molecules was removed from the liquid next to the stationary surface for heterogeneous simulations. The contact angle of the cap was set to match the expected wettability of the surface. The simulation procedure then continued as in the homogeneous investigations. An example of a measured heterogeneous bubble profile is shown in figure 2.5.

Bubble Nucleation: The same simulation setup is used for the heterogeneous nucleation simulations (chapter 5). For the investigations on smooth surfaces, the surface area is reduced to a 20 nm side length square for reduced computational cost. This is increased to 30 nm for the investigations into nucleation in conical cavities, to allow for cavity radii of 10 nm to fit within the simulation domain. In these investigations, the fluid is integrated in the NVT ensemble to control the system temperature. The system temperatures are slowly increased until nucleation occurs.

2.6.1 Domain independence

To show the independence of the measured bubble radii from the size of the domain, secondary simulations were performed investigating the growth of a homogeneous vapour bubble with a side length of 80 nm. As before, the system was equilibrated prior to the insertion of a bubble and then allowed to grow in the NVE ensemble. Figure 2.6 shows a comparison of the growth rates measured for the case of $T = 130$ K, $P = 0.1$ MPa, and $R_0 = 7$ nm for the two domain sizes: 60 nm and 80 nm. The plot shows good agreement between the two data sets. This is to be expected as the sum of the bubble radius and diffusive thermal length scale, given as $\delta = \sqrt{\alpha t}$, is less than the distance between the bubble interface to the periodic boundary throughout the simulation.

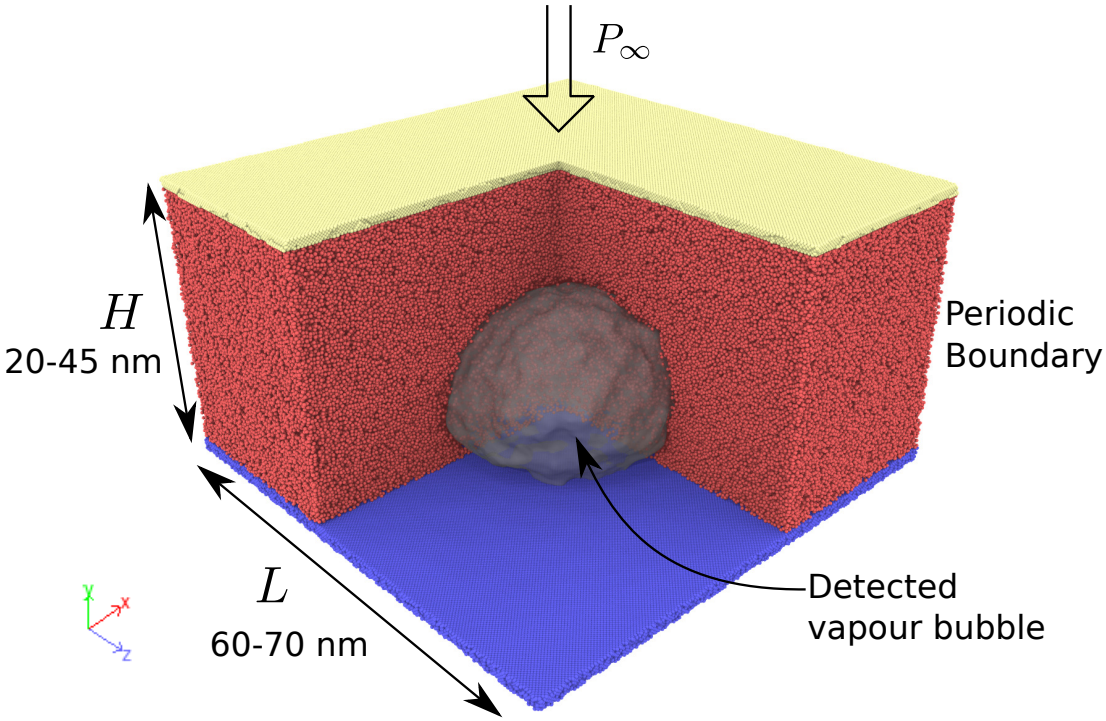

Figure 2.5: Sample simulation setup with detected bubble highlighted (coloured grey). The simulation domain length L and height H are adjusted depending on the investigation being performed. The pressure of the system is controlled by applying a constant force on the piston molecules (coloured yellow).

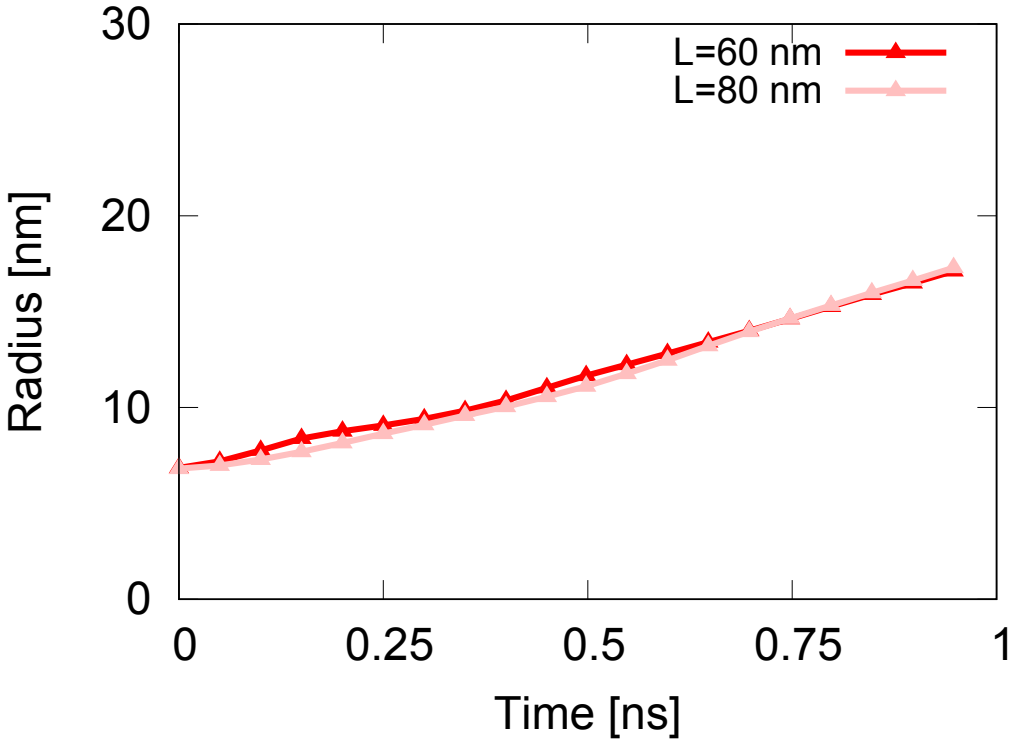

Figure 2.6: The measured radius of a vapour bubble for domain sizes of 60 nm and 80 nm with $T = 130\,\mathrm{K}$, $P = 0.1\,\mathrm{MPa}$, and $R_0 = 7\,\mathrm{nm}$.

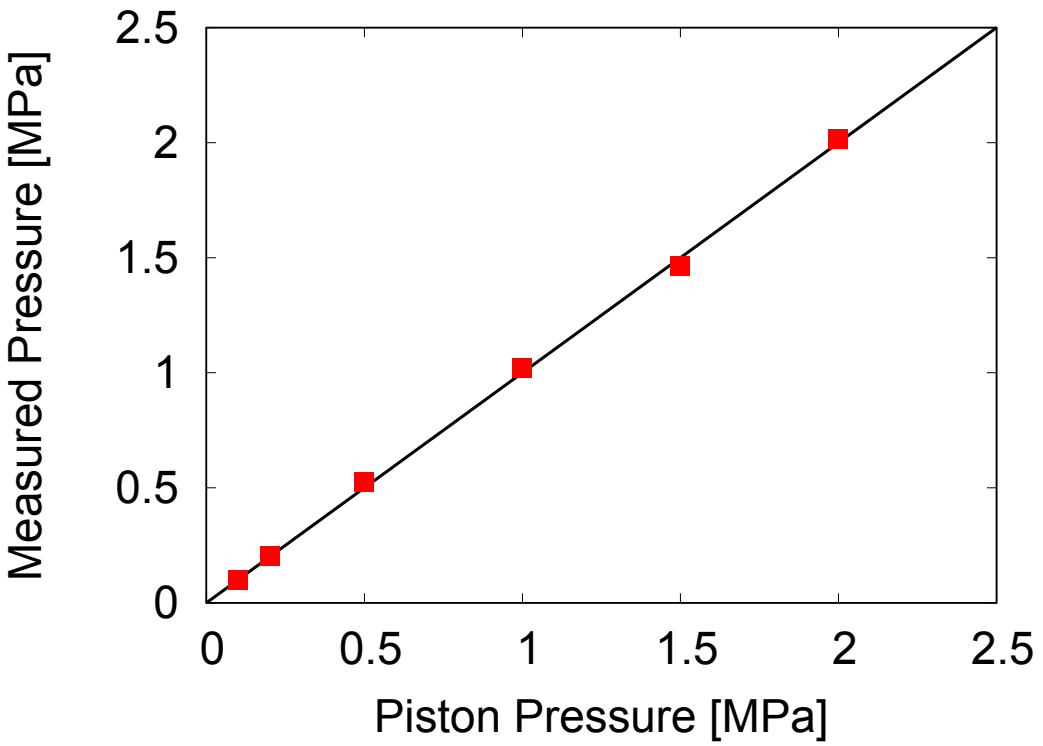

Figure 2.7: Comparison of the pressure input to the piston and the pressure measured in the bulk fluid.

2.7 Pressure control

As discussed in section 2.4, the pressure of the MD simulations is controlled through the use of a piston. The piston is achieved by restricting the motion of a group of molecules to the normal direction. All forces acting on the piston are averaged and applied at the piston centre of mass, treating the piston as a single solid object. The pressure in the fluid $P_\infty = 0.1$ MPa was controlled through a constant force F, applied to each particle in the piston. The force is given by $F = P_\infty A_P / N_P$, where A_P is the wetted area of the piston, and N_P is the number of piston atoms. During the equilibration stage, a fictitious damping force was also added to the piston to prevent excessive oscillations, which could lead to cavitation bubbles forming in the liquid. The damping force was calculated by scaling the velocity of the piston by a damping constant, c. The damping constant used in these simulations was approximately 7 fN-s/m, which was applied to the motion of each piston molecule. Figure 2.7 shows the agreement of the measured pressure in the bulk fluid with the pressure applied to the piston. It is worth noting that these bulk pressure values do not include the fluid at the fluid-solid interface, where the stress tensor is no longer scalar, *i.e.* $\tau_{xx} \neq \tau_{yy}$, due to the interfacial tension (Yamaguchi et al., 2019).

2.8 Bubble detection

The radius of the bubble was determined by measuring the volume of the bubble, V, and converting it to an equivalent radius R_{eq} using the equation $R_{\text{eq}} = (3V/4\pi)^{1/3}$. The volume of the bubble was measured by overlaying the simulation domain with a cubic lattice of non-interacting nodes prior to running the simulation, and determining the number of these nodes in vapour-like regions. A node was determined to be in liquid-like or vapour-like regions based on its coordination number, which is defined as the number of molecules within a specified distance. A cutoff of $N_c = 15$ argon molecules within a distance of $r = 1.3$ nm was chosen as the criterion for a vapour-like lattice node. This criterion was determined from analysing the radial distribution function of the liquid and vapour in a separate simulation, and focusing on a coordination number clearly between the values of liquid and vapour. The value of the cutoff distance used for these measurements is notably larger than others previously used (Datta et al., 2021) to provide increased statistical confidence in the measurements and prevent the false detection of bubbles in the bulk fluid. Each lattice node determines whether a cube of volume d^3, where $d = 0.3$ nm is the spacing of the lattice nodes, is in a liquid-like or vapour-like region. The total bubble volume is therefore the number of vapour-like lattice nodes multiplied by d^3. This is highlighted in figure 2.8

An example of the vapour like lattice nodes can be seen in figure 2.9(c). This bubble measurement technique can be implemented directly in LAMMPS by creating fictitious molecules to represent the lattice nodes. This technique mimics measuring the local density in a Cartesian binned system, but allows for the calculations to be performed during the simulation, taking advantage of the computational optimisations already present in LAMMPS.

In the case of heterogeneous vapour bubbles, an adjustment must be made to the calculated coordination number to account for the presence of the surface. The bulk coordination number N_c is scaled by the volumetric scaling factor associated with the spherical cap formed by excluding the surface from the measurement area. The coordination number threshold for the near wall region $N_{c,sc}$ within a distance r of the measured node can be given in terms of the distance above the surface y as:

$$N_{c,sc} = N_c \frac{(y+r)^2}{4r^3} (2r - y) \,. \tag{2.12}$$

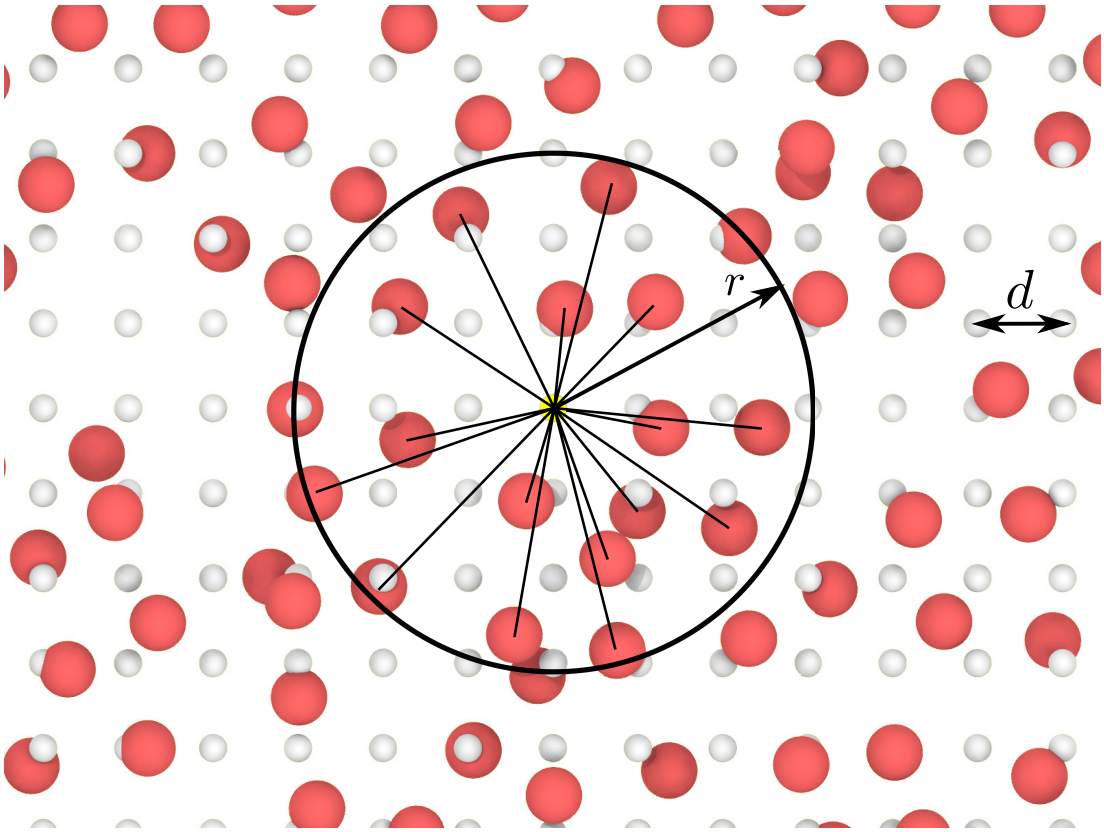

Figure 2.8: Schematic showing the number of fluid molecules (red) within a radius r of the central lattice node (yellow). The lattice nodes (gray) are separated by a distance d.

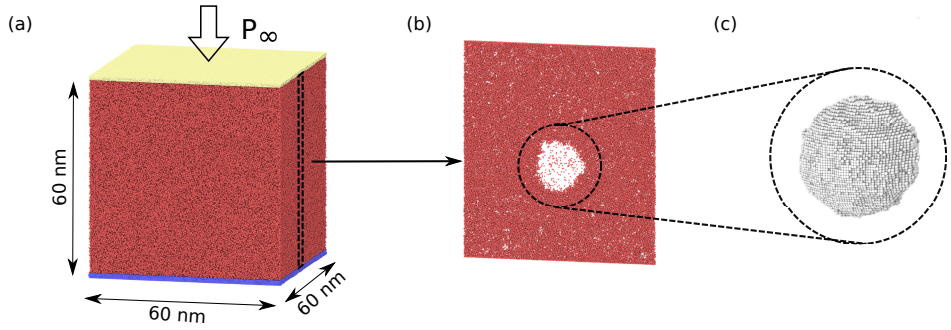

Figure 2.9: (a) The MD simulation domain, red atoms are argon, blue atoms form the bottom (stationary) surface and yellow atoms belong to the piston. (b) A simulation slice, showing the presence of a vapour bubble in the bulk of the fluid. (c) Detected bubble from lattice coordination number showing vapour like nodes.

Table 2.1: LJ scaling factors for varying wettability surfaces with approximate contact angles from literature and measured from MD simulation.

β	θ_l [°]	θ_{MD} [°]
0.9	10	14
0.7	40	43
0.65	55	55
0.6	70	73
0.5	95	96
0.4	120	125
0.3	150	148

2.9 Contact angle measurement

To investigate the effect of surface wettability, the molecular potential was adjusted using the model of Nagayama and Cheng (2004). This model is based on the Lorentz—Berthelot combining rules (equation (2.13) and equation (2.14)) which predict the effective length and energy scales for the fluid-solid interaction, σ_{sl} and ε_{sl}, respectively:

$$\sigma_{sl} = \frac{\sigma_s + \sigma_l}{2}, \tag{2.13}$$

$$\varepsilon_{sl} = \sqrt{\varepsilon_s \varepsilon_l}. \tag{2.14}$$

Their model incorporates the modifications made by Din and Michaelides (1998) as well as by Barrat and Bocquet (1999). The factor α scales the magnitude of the potential, while the factor β adjusts the balance of attractive to repulsive components (shown here without cutoff term for simplicity).

$$U_{sl}(r_{ij}) = 4\alpha\sqrt{\varepsilon_s \varepsilon_l}\left(\left(\frac{\sigma_{sl}}{r_{ij}}\right)^{12} - \beta\left(\frac{\sigma_{sl}}{r_{ij}}\right)^{6}\right). \tag{2.15}$$

To adjust this model to a form resembling the traditional LJ potential, modified forms of the length and energy scales are used:

$$\sigma^*_{sl} = \beta^{1/6}\sigma_{sl}, \tag{2.16}$$

$$\varepsilon^*_{sl} = \alpha\beta^2\varepsilon_{sl}. \tag{2.17}$$

A value of $\alpha = 0.14$ was used for the partial wetting simulations (Zhang et al., 2020), allowing for wettability to be controlled by β. The values of β used, and the corresponding contact angles, are given in Table 2.1. Additionally, a completely wetting case, using the fluid interaction parameters for the solid-fluid interaction was performed.

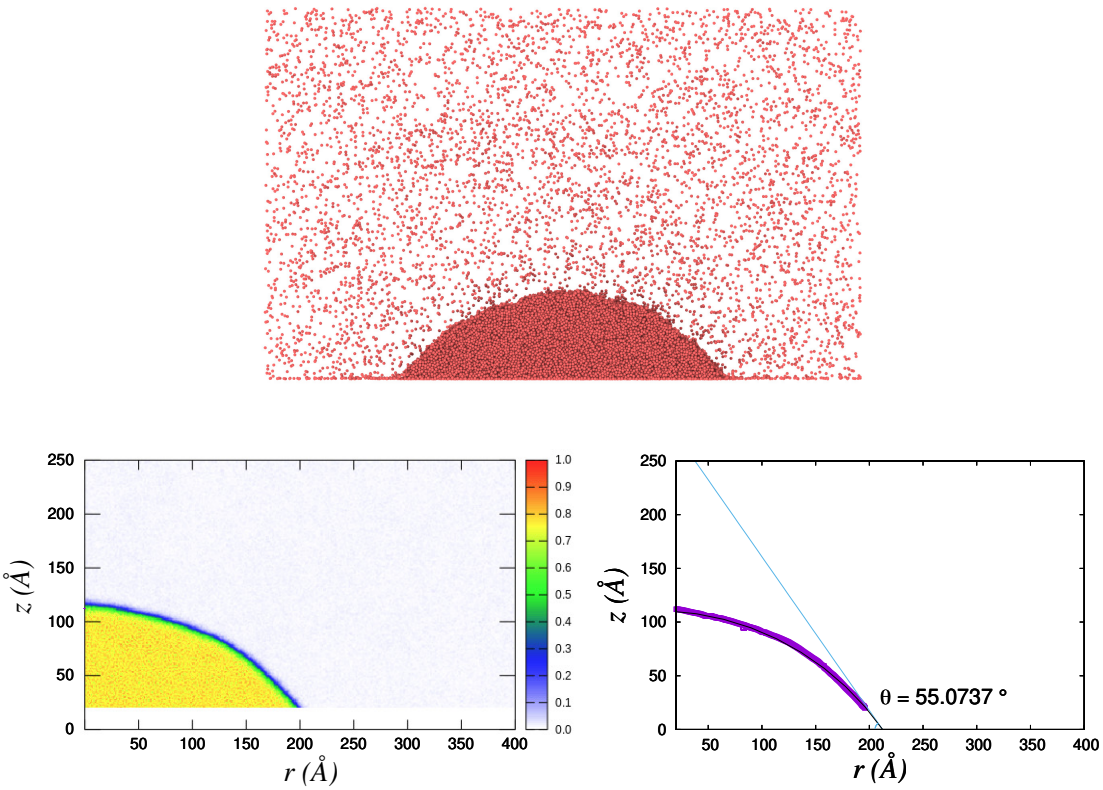

Figure 2.10: Simulation snapshot of equilibrated fluid droplet alongside normalised measured density profile and measured contact angle.

Contact angles are confirmed by running quasi 2D MD simulations of droplets on surfaces with the specified potential. A circle is fit to the 50% isodensity contour of the droplet density profile measured from these simulations. The resulting circle's intersection with the surface is used to compute the contact angle. This is shown in figure 2.10. Figure 2.11 shows the measured contact angles from these MD simulations. The plot shows a clear inverse trend of the liquid contact angle with β, indicating that as the fluid-solid interaction strength increases, the surface wettability increases.

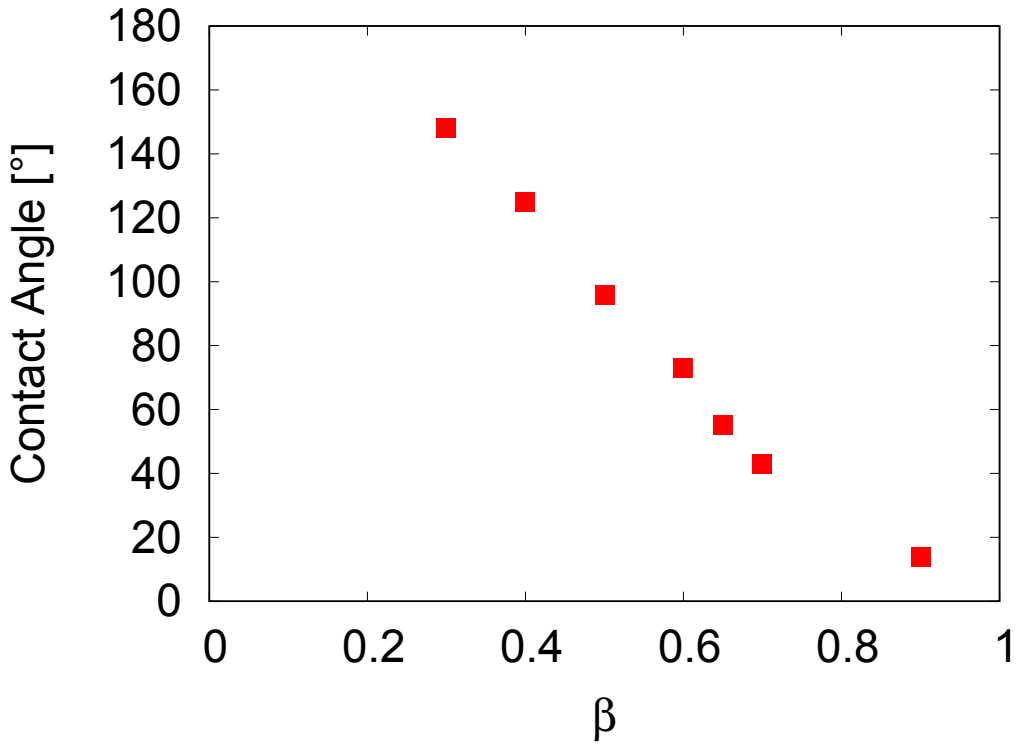

Figure 2.11: Plot showing the measured contact angle of quasi 2D droplets for various values of β.

2.10 Summary

Molecular dynamics is a powerful simulation tool capable of modeling multi-component systems with high spacial and temporal resolution. By defining the intermolecular potentials, the dynamics of the system can be calculated through the time integration of Newton's equations of motion. Through the careful selection of these intermolecular potentials, realistic fluids can be accurately modelled. Statistical mechanics allows for the macroscale fluid properties of these molecular systems to be measured. As the potentials are the only inputs to the model, all material properties are emergent from the system dynamics and are not needed to be modelled separately.

In this chapter, the fluid properties of the argon model used in the investigations are validated against reference data. Good agreement between the model and experimental results is obtained for the density, vapour pressure, and surface tension of the saturated fluid across a range of temperatures. The simulation setups and techniques used in the investigations are outlined, with the differences between them highlighted. The piston technique used to control the pressure of the fluid is validated, showing excellent agreement between the input and measured pressures. The bubble detection and measurement technique, utilising a grid of non-interacting molecules and computing the coordination number is outlined. The adjustments required to accurately measure the near wall behaviour are highlighted.

The fluid-solid interaction potentials used to model different wetting states are given, with the contact angles corresponding to each potential value measured. Additionally, the inherently non-continuum nature of the simulations does not produce a singularity at the three-phase line. This makes MD a useful tool for capturing the formation and growth of vapour bubbles, as the complex, multi-phase physics is all captured by the molecular potentials. Finally, a domain independence study is presented, showing that the growth rates of homogeneous vapour bubbles, which will be analysed in detail in the next chapter, is independent of the domain size for the timescales considered here.

Chapter 3

Inertio-thermal Vapour Bubble Growth

The results of this chapter have already been published in: Sullivan, P., Dockar, D., Borg, M. K., Enright, R., & Pillai, R. Inertio-thermal vapour bubble growth *J. Fluid Mech.* (2022), vol. 948, A55, and is available at doi:10.1017/jfm.2022.734

3.1 Introduction

Vapour bubble growth has long been an area of scientific interest, as they underpin numerous natural phenomena (Prosperetti, 2017) and engineering applications, such as ultrasonic cleaning (Yasui, 2018) and two-phase thermal management systems (Robinson & Judd, 2004). Vapour bubble growth can also have deleterious effects; for example, they have been shown to play a significant role in the explosive failure of pressurised containers (Reinke, 1997) and the dryout failure of pool boiling systems (Chu et al., 2013). Understanding the growth behaviour of vapour bubbles is therefore an important open problem, and current theoretical models remain incomplete.

In one of the earliest theoretical analyses on homogeneous vapour bubble growth, Plesset and Zwick (1954) equated the latent heat required to grow the bubble to the heat available through conduction. Their Plesset–Zwick (PZ) model predictions showed excellent agreement with experimental results for water (Dergarabedian, 1953) and later for other fluids (Dergarabedian, 1960; Florschuetz et al., 1969). However, the PZ model was subsequently shown to significantly overpredict the growth of bubbles at reduced pressures (Lien, 1969), where there is an increased timescale at which thermal effects dominate the bubble's growth. This overprediction results from an unphysical infinite initial velocity, instead of being limited by inertial forces until the thermal timescale has been reached.

Mikic et al. (1970) accounted for this inertial limit and derived a formula that interpolates between the inertial velocity given by Rayleigh (1917) and the thermal velocity of Plesset and Zwick (1954); their model is now commonly referred to as the Mikic–Rohsenow–Griffith (MRG) model. The MRG model removes the infinite initial velocity predicted by the PZ model, instead bounding it by the inertial limit, which then better matched experimental data (Lien, 1969). While the MRG model accurately captures the transition between the inertial- and thermal-limiting velocities, it still overpredicts the growth of an initially static bubble, as it assumes a finite initial velocity. Additionally, there does not exist a model capable of capturing the effects of capillarity and viscosity, which are both relevant to early-stage growth (Avdeev, 2016).

This theoretical bottleneck, coupled with the difficulties in obtaining high resolution data for isolated bubble growth, has led to the development of numerical techniques for the measurement of bubble growth rates (Dalle Donne & Ferranti, 1975; H. S. Lee & Merte, 1996). These numerical investigations have been used to show excellent agreement with the existing theories, failing only when the assumptions made by the theories are shown to be invalid (Robinson & Judd, 2004). Most numerical models solve the coupled momentum and energy differential equations, with varying approximations for the treatment of heat transfer in the thermal boundary layer (Prosperetti & Plesset, 1978). Recent works have investigated the approximations typically made in the momentum equation, such as Bardia and Trujillo (2019) who added the effects of mass transfer across the bubble interface. While these numerical studies provide high-resolution data for the growth of vapour bubbles, they do not provide additional clarity to the understanding of the relationship between the inertial and thermal limitations on bubble growth rates that can be obtained from an analytical model.

In this chapter a new class of inertio-thermal models for the growth of homogeneous vapour bubbles is presented, capable of capturing the competition between inertial and thermal effects on bubble growth. The entire lifetime of the bubble is modeled by limiting the growth by the available inertia. When compared with existing experimental and numerical data, better agreement is shown than the MRG model. Viscous and capillary effects are incorporated, which are required for nanoscale bubble growth, with comparisons made against new molecular simulations.

3.2 Bubble Growth

In the absence of thermal effects, the growth of a spherical vapour bubble with vapour pressure P_v surrounded by a liquid at pressure P_∞ is described by the Rayleigh–Plesset (RP) equation for Newtonian fluids (Prosperetti, 1982):

$$R\ddot{R} + \frac{3}{2}\dot{R}^2 = \frac{1}{\rho_l}\left(P_v - P_\infty - \frac{2\gamma}{R} - \frac{4\mu\dot{R}}{R}\right). \tag{3.1}$$

where the R, $\dot{R}$, and $\ddot{R}$ represent the radius, radial velocity, and radial acceleration, respectively. ρ_l, γ, and μ represent the liquid's density, surface tension, and dynamic viscosity, respectively. Equation (3.1) has been further generalised to account for non-Newtonian viscosity and mass transfer at the liquid-vapour interface (Prosperetti & Plesset, 1978) as well as the effects of a non-condensable gasses (Brennen, 2013). By integrating equation (3.1), it has been shown that the inertial bubble velocity reaches a maximum value of A, given as (Prosperetti, 2017):

$$\dot{R}_{\mathrm{RP,max}} = A = \sqrt{\frac{2\Delta P}{3\rho_l}}. \tag{3.2}$$

Taking the initial acceleration of $\ddot{R} = \Delta P/\rho_l R_0$ (Brennen, 2013, p. 38), the time taken by a stationary bubble of initial size R_0 to reach this inertial velocity A, can be approximated as:

$$\tau_{\mathrm{RP}} = \frac{A}{\ddot{R}} = R_0\sqrt{\frac{2\rho_l}{3\Delta P}}. \tag{3.3}$$

3.2.1 PZ model

While these expressions describe the inertia of bubble growth, as a bubble grows, maintaining the internal pressure requires evaporation of the surrounding liquid. The latent heat requirements associated with this vapour formation must be provided by conduction through the bulk liquid. We can write the energy balance at the interface as:

$$\rho_v h_{lv}\dot{V} = A_s q'', \tag{3.4}$$

where ρ_v and h_{lv} represent the vapour density and latent heat of evaporation, respectively, and $\dot{V}$ is the rate of change of volume of the bubble. The heat flux q'' is transported across the interface of area A_s. Solutions to equation (3.4) have been found for spherical bubbles by Scriven and Plesset and Zwick (1954), who solved for the heat flux using a thin thermal boundary layer approximation. This gives a limiting value for the growth of vapour bubbles controlled by thermal diffusion.

$$\dot{R}_{\mathrm{PZ}} = Ja\sqrt{\frac{3\alpha}{\pi t}}, \tag{3.5}$$

where $\alpha = k/\rho_l c_p$ is the thermal diffusivity of the liquid, k is the thermal conductivity, and c_p is the specific heat capacity, and ρ_l the liquid density. The Jakob number Ja, is the ratio of sensible heat to latent heat, given by $Ja = \rho_l c_p \Delta T_0/\rho_v h_{lv}$, where ΔT_0 is the initial liquid superheat, and h_{lv} is the enthalpy of vapourisation.

3.2.2 MRG model

Mikic et al. (1970) rewrote equation (3.5) in the form:

$$\dot{R}_{\mathrm{PZ}} = \frac{B}{2\sqrt{t}}\left(1 - \frac{T_{\mathrm{v}} - T_{\mathrm{sat}}}{\Delta T_0}\right), \tag{3.6}$$

where $B = Ja\sqrt{12\alpha/\pi}$, T_{v} is the instantaneous vapour temperature, and T_{sat} is the saturation temperature of the liquid. Assuming that the instantaneous superheat and pressure difference vary linearly (H. S. Lee & Merte, 1996; Theofanous & Patel, 1976) i.e.:

$$\frac{T_{\mathrm{v}} - T_{\mathrm{sat}}}{\Delta T_0} = \frac{P_{\mathrm{v}} - P_\infty}{\Delta P_0}, \tag{3.7}$$

where ΔP_0 is the initial pressure difference, equation (3.5) can now be rewritten in terms of the instantaneous pressure difference, $P_{\mathrm{v}} - P_\infty$:

$$P_{\mathrm{v}} - P_\infty = \Delta P_0\left(1 - \frac{2\sqrt{t}}{B}\dot{R}\right), \tag{3.8}$$

where $\dot{R}$ has been used in place of $\dot{R}_{\mathrm{PZ}}$ to clarify that the pressure difference varies with bubble velocity, consistent with literature on this topic (H. S. Lee & Merte, 1996; Prosperetti, 1982).

Mikic et al. (1970) then modified the inertial-limiting velocity (equation (3.2)) using the instantaneous (time-varying) pressure difference to recalculate the velocity rather than the initial (constant) pressure difference typically used, resulting in the MRG model. Thus, the MRG model accounts for the change in vapour pressure as the bubble grows and cools, producing a quadratic equation for $\dot{R}$. This is expressed in terms of the initial

limiting velocity A_0, calculated using the initial pressure difference ΔP_0. The negative root of this equation was rejected, giving:

$$\dot{R}_{\mathrm{MRG}} = A_0 \left[\sqrt{\frac{A_0^2}{B^2} t + 1} - \sqrt{\frac{A_0^2}{B^2} t} \right]. \tag{3.9}$$

Equation (3.9) represents an improvement over the PZ model (equation (3.5)) as it extends the applicability of the model to earlier stages of bubble growth, removing the non-physical infinite initial velocity that would be obtained if the PZ model were extrapolated (as $t \to 0$, $\dot{R}_{\mathrm{PZ}} \to \infty$ while $\dot{R}_{\mathrm{MRG}} \to A_0$). The MRG model has been shown to accurately predict the transition from inertially-limited to thermally-limited bubble growth (H. S. Lee & Merte, 1996; Robinson & Judd, 2004). Importantly, it sets the timescale:

$$\tau_{\mathrm{MRG}} = \frac{B^2}{A^2}, \tag{3.10}$$

when thermal effects cause the bubble growth to diverge from the inertial limit. Several papers have since made modifications to this model to better capture vapour bubble growth (Board & Duffey, 1971; Prosperetti & Plesset, 1978; Theofanous & Patel, 1976). These modifications generally involve using a different relationship between the vapour pressure and temperature difference, typically a direct linear relationship (H. S. Lee & Merte, 1996; Robinson & Judd, 2004), instead of the Clausius–Clapeyron approximation originally used by Mikic et al. (1970).

While the MRG model is an improvement over the PZ model, it still assumes that the bubble begins growing at the inertial-limiting velocity A, ignoring the finite time required for the bubble to reach this velocity from rest. This assumption implies an infinite radial acceleration in the case of an initially static bubble, which is clearly non-physical. In this work, we account for the finite acceleration of initially-static vapour bubbles rather than assuming the limiting value from equation (3.2), as elaborated in the next section.

3.3 Model Derivations

While the RP equation (3.1) is challenging to solve analytically in its full form, an analytical solution can be obtained for the inviscid case ($\mu = 0$) (Dergarabedian, 1953). However, this solution only provides the time taken for bubble growth for a given radius, and cannot be inverted to obtain an equation for the temporal variation in bubble radius. This prevents using a fully analytical solution to the RP equation with a time-varying vapour pressure, even in the case of zero viscosity.

Instead, a simplified model for the radial velocity in the absence of capillary and viscous effects ($\mu = \gamma = 0$) following the methodology of Avdeev (2016, pp. 55-58) is used. The RP equation (3.1) can be written in the simplified form (Brennen, 2013, p. 37):

$$\dot{R}_{\mathrm{RP}} = A\sqrt{1 - \left(\frac{R_0}{R}\right)^3}. \tag{3.11}$$

Avdeev then integrates this expression in the limits of $R \to R_0$, where the radial velocity $\dot{R} \to 0$, and $R \to \infty$, where $\dot{R} \to A$, and provides a simpler approximation for the radius interpolating these two limits:

$$R = \frac{R_0}{3} + \frac{2R_0}{3}\sqrt{1 + \frac{t^2}{\tau_{\mathrm{RP},0}^2}}, \tag{3.12}$$

by assuming a constant pressure difference ΔP_0, with $\tau_{\mathrm{RP},0}$ representing the corresponding inertial timescale from equation (3.3), computed using ΔP_0 instead of ΔP. Taking the time derivative of equation (3.12) returns the following approximation for the original expression given in equation (3.11):

$$\dot{R}_{\mathrm{RP},0} = \frac{A_0}{\sqrt{1 + \frac{\tau_{\mathrm{RP},0}^2}{t^2}}} \tag{3.13}$$

where $\tau_{\mathrm{RP},0}$ is the inertial growth timescale from equation (3.3).

This model interpolates between the linearly increasing velocity expected in the initial stages of the bubble growth ($\dot{R} \approx \ddot{R}t$) and the constant velocity in the late stages, when the velocity has reached the inertial limit ($\dot{R} \approx A_0$). This model has been shown to give excellent agreement with the numerical solution (Avdeev, 2016, p. 58).

3.3.1 Full Inertio-Thermal Model

Using this simple model for the evolution of the bubble's radius, a new model for the instantaneous velocity of the bubble $\dot{R}_{\mathrm{RP,i}}$, accounting for the change in pressure as the bubble grows, is developed. As Avdeev (2016, pp. 55-58) did for constant pressure, an interpolation between the early and late stages of growth is performed. In the early stages of growth, for $t \ll \tau_{\mathrm{RP}}$, the radial velocity is given as $\dot{R} = \ddot{R}t = At/\tau_{\mathrm{RP}}$. Similarly, in the late stages of growth, for $t \gg \tau_{\mathrm{RP}}$, the radial velocity is given by $\dot{R} = A$. Interpolating between these values gives an instantaneous radial velocity $\dot{R}_{\mathrm{RP,i}}$:

$$\dot{R}_{\mathrm{RP,i}} = \frac{A}{\sqrt{1 + \frac{\tau_{\mathrm{RP}}^2}{t^2}}}, \tag{3.14}$$

which describes the acceleration of the bubble from rest to its limiting value A, with a timescale of τ_{RP} (as opposed to A_0 and $\tau_{\mathrm{RP},0}$, respectively, in equation (3.13)). Note it is the term in the denominator that ensures the bubble velocity starts from zero, which is missing from equation (3.2) and therefore the MRG model (equation (3.9)). Equation (3.14) is equivalent to allowing the pressure to change over time in the velocity expression calculated from equation (3.13).

Following Mikic et al. (1970), the instantaneous pressure difference from equation (3.8) is substituted into the new inertial growth equation (3.14), and the radial velocity terms are treated as equivalent. This obtains the following expression:

$$\dot{R} = \sqrt{\frac{A_0^2}{1 + \frac{\tau_{\mathrm{RP},0}^2}{t^2\left(1 - \frac{2\sqrt{t}}{B}\dot{R}\right)}}\left(1 - \frac{2\sqrt{t}}{B}\dot{R}\right)}, \tag{3.15}$$

where $A_0^2\left(1 - \frac{2\sqrt{t}}{B}\dot{R}\right) = A^2$ and $\tau_{\mathrm{RP},0}^2 \Big/ \left(1 - \frac{2\sqrt{t}}{B}\dot{R}\right) = \tau_{\mathrm{RP}}^2$, from equations ((3.2)) and ((3.3)), respectively. Here a switch in terminology is made from $\dot{R}_{\mathrm{RP}}$ to $\dot{R}$ to equate the radial velocity terms, as was done with the MRG model. This expression accounts for the thermal effects on both the inertial-limiting velocity A and on the inertial timescale τ_{RP}. Rearranging equation (3.15) gives a cubic expression in $\dot{R}$:

$$\frac{2\sqrt{t}}{B}\dot{R}^3 + \left(\frac{4A_0^2 t}{B^2} - 1 - \frac{\tau_{\mathrm{RP},0}^2}{t^2}\right)\dot{R}^2 - \frac{4A_0^2\sqrt{t}}{B}\dot{R} + A_0^2 = 0, \tag{3.16}$$

The solution to equation (3.16) is referred to as the *full inertio-thermal* (FIT) model. In the case of $\tau_{\mathrm{RP}} = 0$, i.e. in the absence of dynamic inertial effects, the equation can be factorised to give:

$$\underbrace{\left(\dot{R} - \frac{B}{2\sqrt{t}}\right)}_{\mathrm{PZ}}\underbrace{\left(\dot{R} + A\left[\sqrt{\frac{A^2 t}{B^2} + 1} + \sqrt{\frac{A^2 t}{B^2}}\right]\right)}_{\text{Rejected MRG}}\underbrace{\left(\dot{R} - A\left[\sqrt{\frac{A^2 t}{B^2} + 1} - \sqrt{\frac{A^2 t}{B^2}}\right]\right)}_{\mathrm{MRG}} = 0. \tag{3.17}$$

These roots correspond to the Plesset–Zwick (PZ) model, the rejected negative solution in the Mikic–Rohsenow–Griffith (MRG) analysis and the MRG model. This factorisation cannot be performed for finite τ_{RP}, however, the equation can be solved using Cardano's formula for solving cubic equations in the form $ax^3 + bx^2 + cx + d = 0$. For this analysis,

it becomes convenient to define the following terms:

$$\Delta_0 = b^2 - 3ac, \tag{3.18}$$

$$\Delta_1 = 2b^3 - 9abc + 27a^2d, \tag{3.19}$$

$$C = \sqrt[3]{\frac{\Delta_1 \pm \sqrt{\Delta_1^2 - 4\Delta_0^3}}{2}}. \tag{3.20}$$

The discriminant of the equation can then by given by $\Delta = (4\Delta_0^3 - \Delta_1^2)/27a^2$. By substituting the values of a, b, c, and d from equation (3.16) and rearranging, the discriminant can be written as:

$$\Delta = A^2\left(A^2\frac{80t}{B^2}\chi + A^2\frac{4t}{B^2} + 12\chi^2 + 12\chi + 4 + 4\chi\left(A^2\frac{4t}{B^2} - \chi\right)^2\right) > 0, \tag{3.21}$$

where χ is the ratio τ_{RP}^2/t^2. As all of the terms in equation (3.21) are positive, the discriminant will always be positive. This indicates that the equation will have three distinct real solutions, except at $t = 0$, where two of the solutions will be identical ($\dot{R} = 0$).

The FIT model can then be expressed in the form:

$$\dot{R} = -\frac{1}{3a}\left(b + \xi^n C + \frac{\Delta_0}{\xi^n C}\right), \tag{3.22}$$

with ξ being the principal cube root of unity:

$$\xi = \frac{-1 + \sqrt{3}i}{2}, \tag{3.23}$$

and n being 2. This corresponds to the canonical third of the three cube roots being the FIT model. As in the case with no dynamic inertial effects (equation (3.17)), the first canonical root corresponds to the PZ model and the second to the rejected solution from the MRG analysis. While equation (3.21) shows that the roots of the equation are real, it is not possible to express the roots in a real form. The roots of this type of cubic equation can only be written symbolically in a complex form. However, when the numeric value of the roots are calculated, they will always be real.

As the FIT model presents as a complex equation, alternatively approximations can be found to the solutions of equation (3.16), which are less accurate than the FIT, but potentially more useful. These approximations further allow the inclusion of the effects of capillarity and viscosity, which are not accounted for in equation (3.14).

3.3.2 Approximate Inertio-Thermal Model

Returning to the derivation of equation (3.13), the assumption of constant pressure difference manifests in the integral (Avdeev, 2016, p.55):

$$\int_0^t \frac{A}{R_0} dt \approx \frac{3t}{2\tau_{\mathrm{RP},0}}. \tag{3.24}$$

If the integral from equation (3.24) is substituted into equation (3.12) rather than the approximated value, an expression for the radius of the bubble with a time varying pressure is retrieved:

$$R = \frac{R_0}{3} + \frac{2R_0}{3}\sqrt{1 + \left(\frac{3\int_0^t \frac{A}{R_0} dt}{2}\right)^2}. \tag{3.25}$$

Taking the time derivative of equation (3.25) gives an approximation for the radial velocity with varying pressure:

$$\dot{R}_{\mathrm{RP,i}} = \frac{A}{\sqrt{1 + \left(\frac{2}{3\int_0^t \frac{A}{R_0} dt}\right)^2}}. \tag{3.26}$$

Taking $A = A_0\sqrt{1 - \frac{2\sqrt{t}}{B}\dot{R}}$ as before, the integral term in equation (3.26) can be approximated by taking a Taylor series expansion around $t = 0$ giving:

$$\int_0^t \frac{A}{R_0} dt = \frac{A_0}{R_0}\int_0^t \sqrt{1 - \frac{2\sqrt{t}}{B}\dot{R}} dt = \frac{A_0}{R_0}\left(t - \frac{2t^{3/2}\dot{R}(0)}{3B} - \frac{t^2\dot{R}(0)^2}{4B^2} + O(t^{5/2})\right). \tag{3.27}$$

Evaluating this approximation for the initially static case $\dot{R}(0) = 0$ and ignoring the higher order terms lets equation (3.26) be approximated as:

$$\dot{R} = \frac{A_0\sqrt{1 - \frac{2\sqrt{t}}{B}\dot{R}}}{\sqrt{1 + \frac{\tau_{\mathrm{RP},0}^2}{t^2}}}. \tag{3.28}$$

Solving this expression for $\dot{R}$ gives:

$$\dot{R}_{\mathrm{AIT}} = \frac{A_0}{\sqrt{1 + \frac{\tau_{\mathrm{RP},0}^2}{t^2}}}\left[\sqrt{\frac{A_0^2}{B^2\left(1 + \frac{\tau_{\mathrm{RP},0}^2}{t^2}\right)}t + 1} - \sqrt{\frac{A_0^2}{B^2\left(1 + \frac{\tau_{\mathrm{RP},0}^2}{t^2}\right)}t}\right], \tag{3.29}$$

which will be referred to as the *approximate inertio-thermal* (AIT) model. Alternatively, rather than the above process, if the inertial-limiting velocity A_0 in the MRG model (equation (3.9)) is directly replaced with the instantaneous velocity from equation (3.14), again gives equation (3.29).

The AIT accounts for the need for the bubble to have grown (and phase change to have occurred), in order for the temperature gradient to form in the liquid. The AIT model can be rewritten more generally in terms of the instantaneous velocity predicted by the constant pressure RP model equation (3.13), $\dot{R}_{\mathrm{RP},0}$, as:

$$\dot{R}_{\mathrm{AIT}} = \dot{R}_{\mathrm{RP},0}\left[\sqrt{\frac{\dot{R}_{\mathrm{RP},0}^2}{B^2}t+1}-\sqrt{\frac{\dot{R}_{\mathrm{RP},0}^2}{B^2}t}\right]. \tag{3.30}$$

This allows the inclusion of the effects of capillarity and viscosity in the model through the calculation of the inertial velocity $\dot{R}_{\mathrm{RP},0}$ directly from equation (3.1). This is achieved in this case by numerically calculating using a Runge–Kutta ODE solver.

The AIT model offers a clearer insight into the coupling of inertial and thermal effects in the growth of vapour bubbles. It can now be seen how the inertial growth of the bubble causes the heat transfer behaviour to change. As the bubble accelerates, a greater heat transfer rate is required to maintain the growth, slowing down the bubble's velocity. Similarly, the model captures how, in the absence of significant inertial effects, the timescale for thermal diffusion controlled growth can be significantly increased. Most importantly, the effects of surface tension and viscosity can be included in the AIT model by explicitly calculating the value of $\dot{R}_{\mathrm{RP},0}$ from equation (3.1) (note that this is not possible in the FIT model). Using this model the coupled inertia and thermal diffusion effects on the growth of vapour bubbles when capillarity and viscosity are relevant can be better understood.

3.3.3 Simple Inertio-Thermal Model

In cases when the ratio of the inertial timescale τ_{RP} (equation (3.3)) to the thermal timescale τ_{MRG} (equation (3.10)) is low i.e. for $\tau_{\mathrm{RP}}/\tau_{\mathrm{MRG}} < 1$, inertial effects occur on a faster timescale than thermal effects, allowing them to be treated as independently changing parameters. This allows further simplification of the AIT model as the bubble will have approached its inertial limiting velocity before thermal effects on growth are significant, giving:

$$\dot{R}_{\mathrm{SIT}} = \frac{\dot{R}_{\mathrm{RP},0}\dot{R}_{\mathrm{MRG}}}{A_0}. \tag{3.31}$$

Equation (3.31) will be called the *simple inertio-thermal* (SIT) model. As with the AIT model, when $t \gg \tau_{\mathrm{RP},0}$ the effect of changing inertia can be disregarded in the SIT model as well. In addition, when $t \ll \tau_{\mathrm{MRG}}$, the $\tau_{\mathrm{RP},0}/t$ terms in equation (3.29) can be disregarded, justifying the simplification in equation (3.31). Again, capillary and viscous effects can be included by explicitly calculating the instantaneous inertial velocity term $\dot{R}_{\mathrm{RP},0}$ from equation (3.1). In general, this simplification can be performed and the SIT model used whenever $\tau_{\mathrm{RP}} < \tau_{\mathrm{MRG}}$.

The FIT, AIT, and SIT models, from equations ((3.16)), ((3.29)), and ((3.31)) respectively, represent a new class of inertio-thermal models for vapour bubble growth. For the cases with $\tau_{\mathrm{RP}} < \tau_{\mathrm{MRG}}$, the SIT model can be used, as inertial and thermal effects occur on different timescales. For $\tau_{\mathrm{RP}} > \tau_{\mathrm{MRG}}$, the AIT model should be used, as it captures the interaction between inertial and thermal effects. The FIT can be used for all timescale ratios, but only in the absence of viscous and capillary effects. An analysis of the agreement of the three models is now presented, highlighting the poor agreement of the SIT model for $\tau_{\mathrm{RP}} > \tau_{\mathrm{MRG}}$, but an improved agreement for $\tau_{\mathrm{RP}} < \tau_{\mathrm{MRG}}$.

3.3.4 Agreement of IT Models

The approximations made in the derivations of the *approximate inertio-thermal* (AIT) and *simple inertio-thermal* (SIT) models introduce additional errors into the predictions when compared to the FIT model. Analysing the disagreement between the model predictions gives further insight into the applicability of these models. Figure 3.1 shows plots of the relative error of the (a) AIT and (b) SIT models to those predicted by the FIT model. These error values are given for a bubble of initial radius R_0 as:

$$\text{Relative Error} = \frac{|R - R_{\mathrm{FIT}}|}{R_{\mathrm{FIT}} - R_0}. \tag{3.32}$$

To evaluate model agreement, the radii predicted by the AIT model were compared to those values predicted by the FIT model for various values of the ratio $\tau_{\mathrm{RP}}/\tau_{\mathrm{MRG}}$. The relative error in the AIT predictions is presented in figure 3.1(a), which shows that the error peaks at $t \approx \tau_{\mathrm{RP}}$ for $\tau_{\mathrm{RP}}/\tau_{\mathrm{MRG}} = 1$, moving to earlier times as this ratio increases and later as it decreases. This maximum relative error value is shown to be $\sim 20\%$ across all values of $\tau_{\mathrm{RP}}/\tau_{\mathrm{MRG}}$, dropping quickly beyond that and reaching a value of $\sim 5\%$ after 10 inertial timescales. The maximum relative error is obtained for a ratio of $\tau_{\mathrm{RP}}/\tau_{\mathrm{MRG}} \approx 4$, with the error decreasing as the ratio is changed from this value.

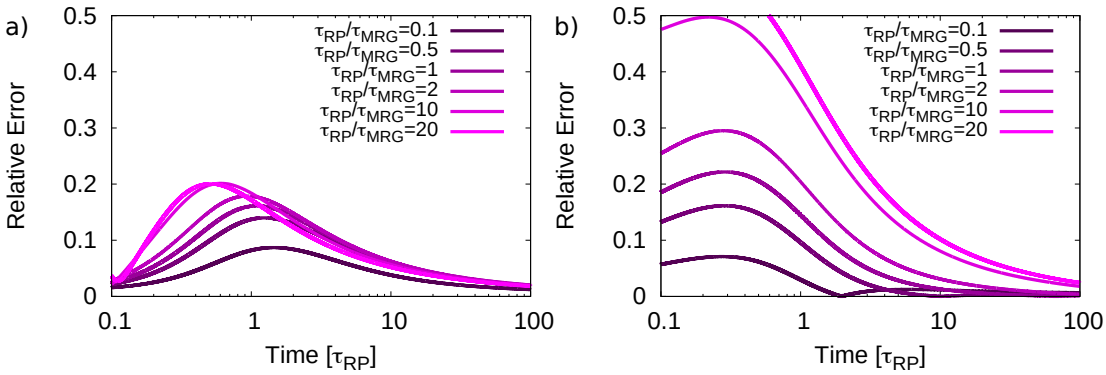

Figure 3.1: Relative error of the (a) AIT and (b) SIT models compared to the FIT model for various ratios of $\tau_{\mathrm{RP}}/\tau_{\mathrm{MRG}}$.

The SIT model predictions are compared to the FIT model in figure 3.1(b) to highlight when it is appropriate to use the model. The relative error now peaks consistently at a time of $0.25\tau_{RP}$. There is improved agreement compared to the AIT model for ratios $\tau_{\mathrm{RP}}/\tau_{\mathrm{MRG}} < 1$, as the relative error of the SIT model goes to zero at comparatively lower values of τ_{RP}, in contrast with the AIT model in figure 3.1(a), where they remain non-zero for the entire duration. The maximum error increases with $\tau_{\mathrm{RP}}/\tau_{\mathrm{MRG}}$ and, unlike the AIT model, continues to increase indefinitely with $\tau_{\mathrm{RP}}/\tau_{\mathrm{MRG}}$.

Here, the FIT, AIT, and SIT models are given in terms of the variables A, B, and τ_{RP}. As these equations are dependant on three variables, investigating their influence on the relative error is important. It then becomes convenient to analyse the equations in terms of three alternate variables, namely τ_{RP}, τ_{MRG} and R_0. In this case, it can be clearly seen that for a given value of $\tau_{\mathrm{RP}}/\tau_{\mathrm{MRG}}$ the values are dependant only on R_0. Therefore, figure 3.2 shows the variation of the errors plotted in figure 3.1 for various values of R_0 for the case of $\tau_{\mathrm{RP}}/\tau_{\mathrm{MRG}} = 1$. These radii are presented in terms of τ_{RP} with a $1\ m/s$ velocity scaling. There is excellent agreement in the error values for both the AIT and SIT equations across all values of R_0, indicating that the error is dependant only on the ratio of the inertial and thermal timescales $\tau_{\mathrm{RP}}/\tau_{\mathrm{MRG}}$.

3.4 Model Validation

3.4.1 In the absence of viscous and capillary effects

The effect of capillarity can be quantified through the ratio of the bubble's initial radius to the critical radius $\mathcal{R} = R_0/R_c$. The effect of viscosity can be quantified by the Reynolds number, $Re = A_0 R_0 \rho_l/\mu$. Capillary and viscous effects are expected to be greater for lower values of $\mathcal{R}$ and Re, respectively. In the absence of viscous and capillary effects, the inertio-thermal models are expected to deviate most from the MRG model

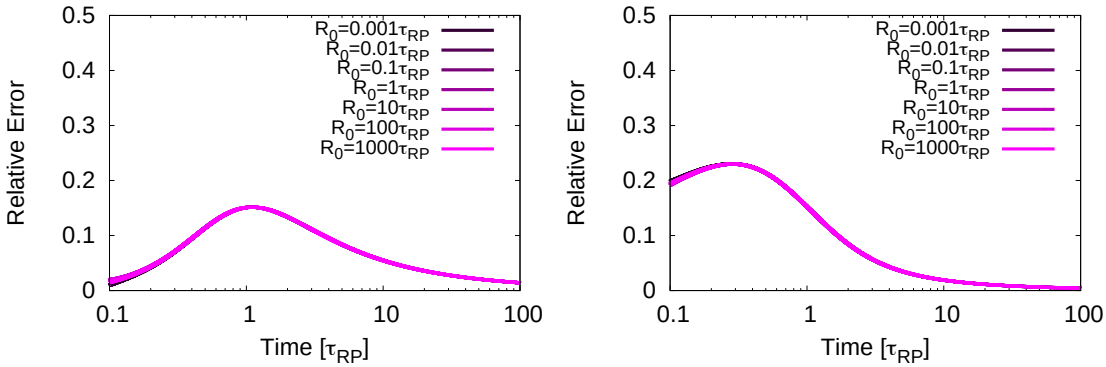

Figure 3.2: Relative error of the (a) AIT and (b) SIT models compared to the FIT model for various initial radii at a timescale ratio of $\tau_{\mathrm{RP}}/\tau_{\mathrm{MRG}} = 1$.

predictions when the thermal timescale is smaller than the inertial, i.e. $\tau_{\mathrm{RP}}/\tau_{\mathrm{MRG}} > 1$. The experiments of Florschuetz et al. (1969) meet this criterion as $\tau_{\mathrm{RP}}/\tau_{\mathrm{MRG}} \approx 42.5 > 1$. The effects of capillarity and viscosity can be neglected for this case as $\mathcal{R} \approx 60$ and $Re \approx 1700$.

The predictions of the MRG (equation (3.9)) and IT models are compared to the data in Florschuetz et al. (1969) in figure 3.3(a). From the figure it can be seen that the IT models better describe the early stages of the bubble's growth. The initial inertial velocity predicted by the MRG model overpredicts the actual growth rate. In the latter stages of the bubble's growth, the velocities predicted by both models converge to the limiting value of the PZ model. Therefore, in the absence of viscous and capillary effects, the MRG model overpredicts the experimental data overall, while the IT model predictions (which lie on top of each other) are more accurate. In this case, there is good agreement between all three IT models, as there are no effects of capillarity or viscosity.

It is worth noting that the results reported by Florschuetz et al. (1969) were for reasonably isolated bubbles that nucleated in the bulk liquid. This ensured that the thermal boundary layer of the bubble was not disrupted by the presence of other bubbles or the walls of the test vessel during the measurement period. In contrast to Lien (1969), where the maximum disruption to the thermal boundary layer was expected in the early stages of growth due to the electrodes used to cause the bubble nucleation, Florschuetz et al. (1969) nucleated bubbles on natural nucleation sites in the bulk liquid. In this case, the greatest deviation from theory is expected in the later stages of growth, when the bubble has grown sufficiently large for its thermal boundary layer to interact with the surroundings. For this reason, the disagreement of the early stage experimental results and the MRG model can be attributed to the limiting inertia and not the presence of other bubbles or walls.

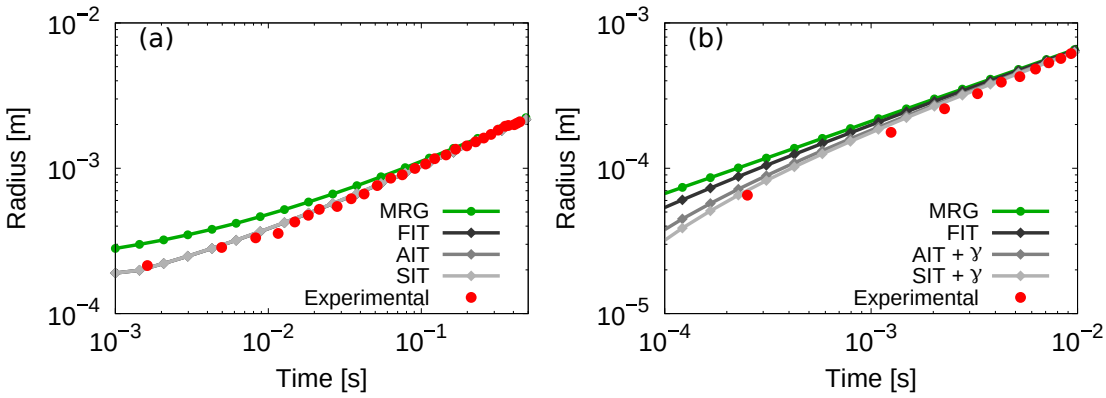

Figure 3.3: Comparisons of the predictions of the MRG and the IT models to the experimental work of (a) Florschuetz et al. (1969) where capilarity and viscosity are not relevant, and (b) Dergarabedian (1953). Note the symbol γ in (b) represents the inclusion of surface tension in the calculation of the AIT and SIT models.

3.4.2 The effect of capillarity

Capillary effects become important in determining the growth of bubbles when they are close to the critical size. In these cases, the available hydrodynamic pressure in the bubble is reduced by the Laplace pressure across the interface. Both numerical (H. S. Lee & Merte, 1996; Robinson & Judd, 2004) and experimental (Dergarabedian, 1960) studies have focused on the growth of critically-sized bubbles. One of the earliest such studies was that of Dergarabedian (1953), who experimentally measured the growth of vapour bubbles at low superheats. The case shown in figure 3.3(b) is of the growth of a water vapour bubble at a superheat of $\Delta T = 3.1\text{K}$. The bubble is initialised close to the critical radius, with $\mathcal{R} \approx 1.05$. The effect of viscosity can be neglected as $Re \approx 100$. The SIT model (with capillary effects included, shown as SIT + γ in figure 3.3(b)) can be used to predict the bubble growth here, as $\tau_{\text{RP}} < \tau_{\text{MRG}}$ ($\tau_{\text{RP}} \approx 2.3\,\mu\text{s}$ and $\tau_{\text{MRG}} \approx 5.3\,\mu\text{s}$). The SIT model allows the use of the exact inertial velocity, calculated from numerically integrating the RP equation (3.1), which includes the effects of capillarity *i.e.* the $2\gamma/R$ term in equation (1.1) is not zero, using a Runge–Kutta ODE solver. Figure 3.3(b) shows that the SIT curve provides better agreement with the experimental data than the MRG model, most notably during the earlier stages of growth. The AIT model (with capillary effects included, shown as AIT + γ in figure 3.3(b)) also provides good agreement for the growth of the bubble, predicting a slightly higher radius than the SIT model. The FIT model, which does not include capillary effects, does not show the same level of agreement. In this case, when capillarity dominates the early stage growth behaviour, the FIT model predicts bubble radii noticeably closer to those of the MRG model than the AIT and SIT models.

Again, as with the case in figure 3.3(a), the effects of surrounding bubbles and the walls of the experimental container are deemed negligible in their effect on the experimental results as their distances are significantly greater than the thermal boundary layer thickness δ_T, which can be approximated as $\delta_T = \sqrt{\alpha t} \approx R/2Ja$ (Dergarabedian, 1953). This allows the decreased growth rate in the early stages be attributed to the limiting inertia, rather than limited thermal diffusion due to the disruption of the boundary layer (Enríquez et al., 2014).

Numerical modelling of the growth of sodium bubbles was performed by Dalle Donne and Ferranti (1975) who coupled the Energy and Rayleigh–Plesset equations directly, and solved them with a Runge–Kutta solver. Prosperetti and Plesset (1978) additionally included the thin thermal boundary layer assumption of Plesset and Zwick (1954) to simplify the energy equation. These bubbles are initiated at close to their critical size, and capillary effects therefore play a significant role in the dynamics of the bubbles.

Figure 3.4 tracks the bubble radius R for cases representing (a) high, (b) moderate and (c) low superheats, respectively, compared to the MRG and IT model predictions. These plots show that the AIT and SIT models, with capillary effects included, provide better agreement with the numerical data across the range of superheats. During the early stages of the bubble growth, the MRG model fails to capture the acceleration of the initially-static bubble. This leads to the overprediction of the velocity and, subsequently, the radius of the bubble as seen for each of the three cases in figure 3.4(a–c). This overprediction does not occur for the AIT and SIT models, which capture these dynamic inertial effects. Little disagreement between the FIT and MRG models is seen due to the strong effects of capillarity in these near critically sized bubbles, which is not included in either model. During the late stages of the bubble growth, the agreement between all the IT models and the MRG model improves, as with previous cases. When the bubble has grown to the point where the dynamic inertial effects have stabilised, the growth is determined entirely by thermal effects. In the case of the low superheat, shown in figure 3.4(c), some disagreement between the results of Prosperetti and Plesset (1978) and the MRG model, and by extension the SIT model, is observed at larger timescales. This is attributed to the invalidity of the thin thermal boundary layer approximation at low Ja where additional terms ignored in the PZ model become important (Avdeev, 2016; Plesset & Zwick, 1954).

Robinson and Judd (2004) perform similar numerical calculations, investigating the transition from surface tension- to thermally-controlled growth of water vapour bubbles across a range of operating conditions. Their analysis shows that the assumptions in the MRG model are invalid at low Ja, showing disagreement with their results for $Ja < 10$. This is attributed to the theoretical limits of the PZ model, which is not accurate for $Ja < 4$ (Avdeev, 2016). This disparity is accounted for by considering the

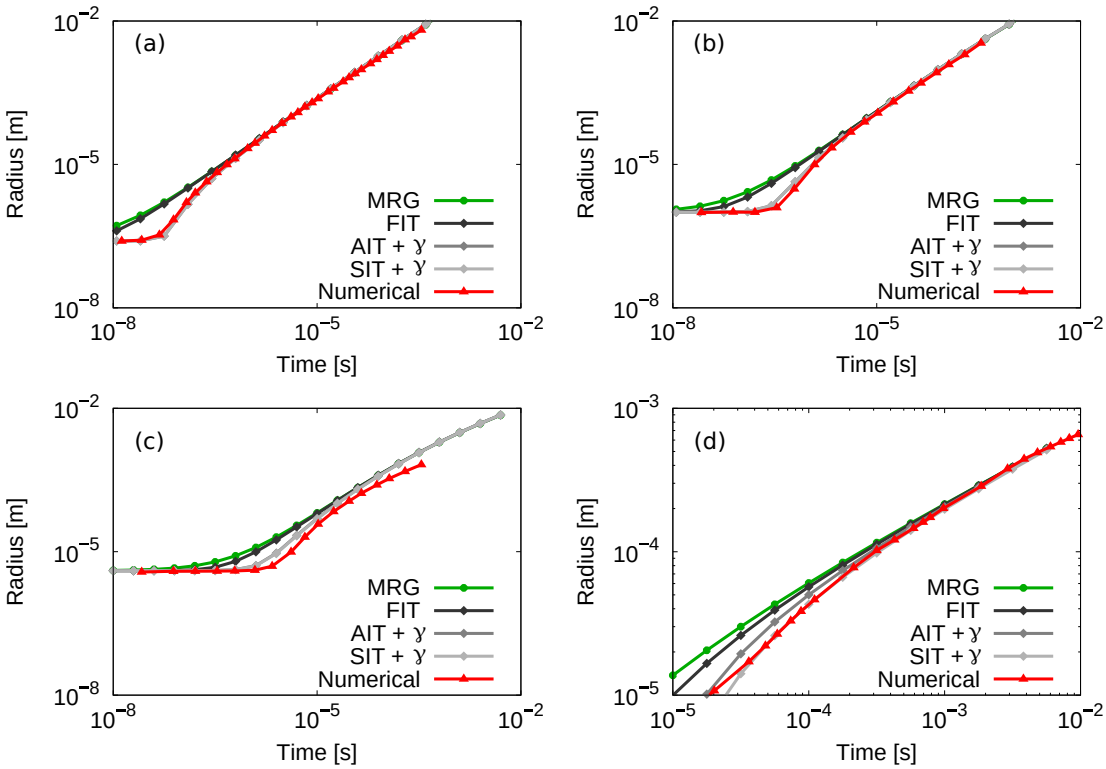

Figure 3.4: A comparison of the predictions of the MRG and IT models to the numerical studies of (a) high, (b) moderate, and (c) low superheats from the work of Prosperetti and Plesset (1978), and (d) Robinson and Judd (2004).

changing inertial driving force in the inertio-thermal models. Figure 3.4(d) shows vastly improved agreement between the results of Robinson and Judd (2004) and the AIT and SIT models when compared to the MRG model for $Ja = 9$. When the IT models are compared to each other, there is slightly better agreement visible with the SIT model than the AIT model, which will be elaborated on in the next section. Note that the bubble radius data from Robinson and Judd (2004) is offset by the initial radius, and the time data is offset by a thermal time constant, which is the time taken for the system to react to a change in the thermal environment, given as $t_c = 4\gamma^2/\left(9\alpha\Delta P^2\right)$.

3.4.3 The effect of viscosity

So far, only bubble growth in the absence of viscous effects has been analysed. Viscosity has been shown to be largely insignificant in many of the cases analysed in literature (Robinson & Judd, 2004), and so is typically not included in numerical investigations (Dalle Donne & Ferranti, 1975; H. S. Lee & Merte, 1996). However, for critically-sized bubbles at near-spinodal conditions, viscosity becomes one of the determining factors in the growth rate of the bubble (Avdeev, 2016, p. 63). These conditions are difficult to produce experimentally. The small critical radii near the spinodal mean that it

is very likely that a nucleation event will occur in an unplanned location, making it harder to study. Combined with the difficulties of measurement on the length and time scales necessary to capture the bubble growth in sufficient detail, this means that experimental data is not readily available to make comparisons. Thus, to validate the model predictions for bubble growth within this regime, molecular dynamics (MD) simulations were performed.

The MD simulations allow the measurement of the growth of Argon vapour bubbles with high spatial and temporal resolution. Simulations were performed with bubbles of initial radius 5 nm and 7 nm, each at two operating conditions; temperatures of 130 K and 135 K, and pressures of 0.1 MPa and 1 MPa, respectively. These cases have Reynolds numbers in the range $Re = 2.6 - 4.7$, meaning that viscous effects are of greater importance here than previous cases. The value of $\tau_{\mathrm{RP}}/\tau_{\mathrm{MRG}}$ ranges from $0.01 - 0.4$, permitting the SIT model to be used for these cases. The plots in figure 3.5 compare the MD results to the predictions of the RP, MRG and IT models. Inset in figure 3.5(a) is a series of simulation snapshots showing a section of the MD simulation alongside the measured bubble profile and the model predictions. The MRG model consistently overpredicts the initial growth rate. The RP prediction matches the early stage growth rate, but overpredicts at later stages. The SIT model predictions show excellent agreement for the entire timespan for each of the cases, along with reasonable agreement of the AIT model.

These results imply consistently improved agreement of the SIT model over the AIT model, despite the additional simplifications made in the derivation of the SIT model. From the derivation, it would be expected that the SIT model would underpredict the radius of the bubble as it predicts a greater cooling of the bubble than the available inertia would allow (as the bubble accelerates from rest). However, the linear temperature-pressure relationship used in the derivation of the MRG model, and through it the IT models (i.e. equation (3.7)) overpredicts the vapour pressure during the growth process (Prosperetti & Plesset, 1978) and has been shown to overpredict bubble radii by up to 40% (H. S. Lee & Merte, 1996). Therefore, the apparent advantage of the SIT over the AIT only results from the cancellation of these errors, and is not due to greater accuracy in modelling capacity. Both the SIT and AIT models are well within this range of error for the MD cases presented in figure 3.5, at 15% and 20% respectively. Meanwhile the error in the MRG model predictions is considerably higher during the early stages of growth, only reducing to an acceptable level as the bubble grows far from its initial size.

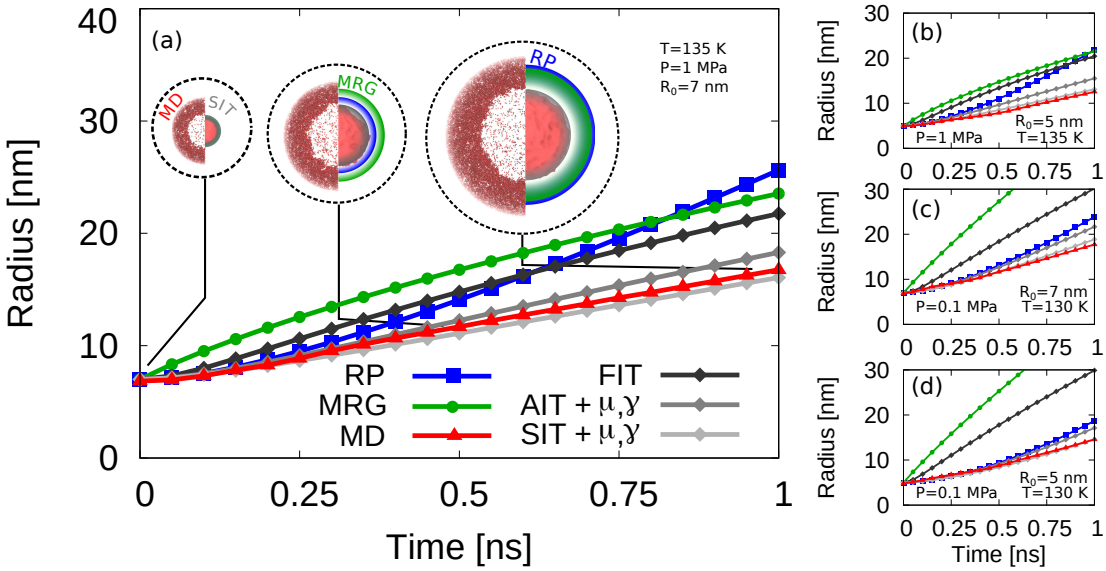

Figure 3.5: Comparison of the predictions of the RP, MRG, and IT models to the MD simulations for four different conditions; (a) $R_0 = 7\,\text{nm}$, $T = 135\,\text{K}$, and $P = 1\,\text{MPa}$, (b) $R_0 = 5\,\text{nm}$, $T = 135\,\text{K}$, and $P = 1\,\text{MPa}$, (c) $R_0 = 7\,\text{nm}$, $T = 130\,\text{K}$, and $P = 0.1\,\text{MPa}$, and (d) $R_0 = 5\,\text{nm}$, $T = 130\,\text{K}$, and $P = 0.1\,\text{MPa}$. Inset in (a) is a series of simulation snapshot segments (left) alongside the measured bubble profile and model predictions at times of 0, 0.5 and 1 ns. Note the symbols γ and μ represent the inclusion of surface tension and viscosity, respectively, in the calculation of the AIT and SIT models.

The effect of viscosity in isolation can be studied by comparing the predictions of the SIT model with and without viscosity. Plotted in figure 3.6 is the case from figure 3.5(a) comparing the SIT model, the SIT model without viscosity (SIT $\mu = 0$), the SIT model without viscosity and capillarity (SIT $\mu = \gamma = 0$), and the FIT model with the MD data. This plot shows that, in the absence of viscosity and capillarity, the SIT model is quite close to the FIT model. Figure 3.6 shows how a constant viscosity can be readily included into the AIT and SIT models when needed.

3.4.4 Effect of Temperature-Pressure Relationship

One of the most significant sources of error in the MRG model is the simplification of the temperature-pressure relationship of the fluid (H. S. Lee & Merte, 1996; Prosperetti & Plesset, 1978; Robinson & Judd, 2004). In their original work, Mikic et al. (1970) approximated this relationship using the integrated Clapeyron equation:

$$P_v - P_\infty = \frac{\rho_v h_{lv}}{T_{\text{sat}}} \left| T_v - T_{\text{sat}} \right| . \tag{3.33}$$

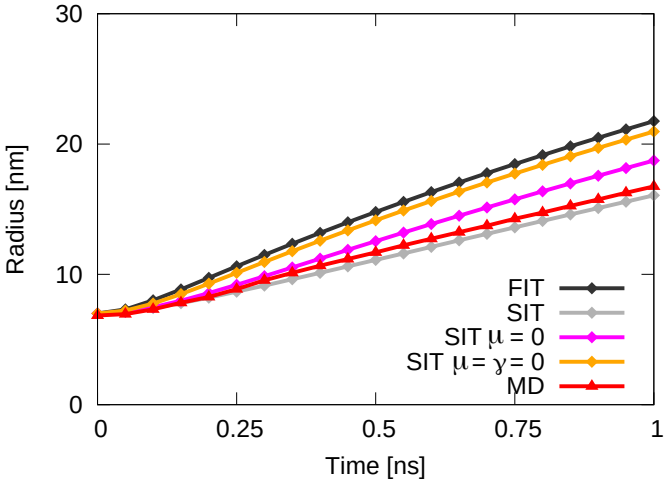

Figure 3.6: Comparison of the predictions of the SIT model with and without viscosity and capillarity to the MD simulations

This relationship accurately captures the slope of the temperature-pressure curve near the saturation temperature but consistently underestimates the actual vapour pressure (Prosperetti & Plesset, 1978; Theofanous & Patel, 1976). This leads to under-predictions of bubble radii as the inertial limiting velocity is under-predicted. This is particularly noticeable in the inertial-controlled regime, i.e. for $t < \tau_{\mathrm{MRG}}$. H. S. Lee and Merte (1996) compared the predictions of the model to their numerical calculations using a more accurate temperature-pressure relationship. They showed that the MRG model consistently under-predicted the radius, with a maximum error of 40%.

To more accurately capture the inertial limiting velocity, a linear relationship between the fluid temperature T_v and vapour pressure, in terms of the initial pressure difference ΔP_0, has been used instead (Prosperetti & Plesset, 1978; Robinson & Judd, 2004):

$$\frac{T_v - T_{\mathrm{sat}}}{\Delta T_0} = \frac{P_{\mathrm{v}} - P_\infty}{\Delta P_0}. \tag{3.34}$$

This linear relationship accurately captures the inertial limiting velocity. However, the vapour pressure is overestimated as the bubble grows and cools, resulting in over-predictions of the bubble radius. In their comparisons of the MRG model using this linear temperature-pressure relationship, H. S. Lee and Merte (1996) showed that the bubble radii were always over-predicted, again with a maximum error of 40%.

A surprising result presented in this chapter is the apparent improved agreement of the SIT model with the cases tested compared to the AIT model, which is counter-intuitive given the AIT model captures more physics and is therefore expected to be more accurate. This result can be explained in a straightforward way using two facts: a) the IT models rely on equation (3.34) to model the temperature-pressure relationship, which

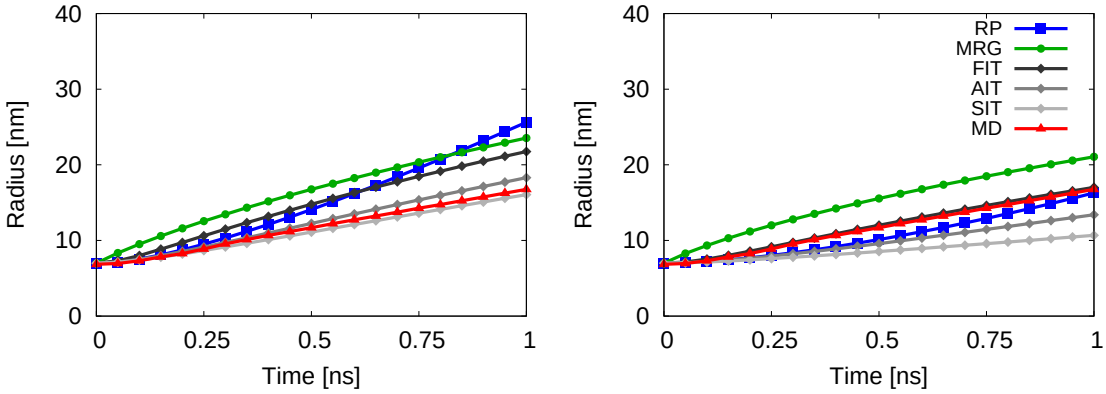

Figure 3.7: Predictions of the RP, MRG, and IT models compared to MD data using (a) the Clapeyron equation (3.33) and (b) the linear relationship (equation (3.34)) as the temperature-pressure relationship.

means that they are expected to overpredict the bubble radii as discussed previously; and b) the SIT model assumes that cooling is occurring as if the bubble is growing at its inertial limiting velocity and subsequently increases the rate at which bubble growth slows in the early stages[1]. Therefore, as per a) above, both AIT and SIT overpredict the bubble radius, but b) means the SIT model consistently underpredicts the bubble radius relative to AIT. The "fortuitous self-cancellation" of errors that results from a) and b) is that SIT deceptively appears to give more accurate predictions in this chapter's figures, but this only results from a systematic (i.e., not physics-based) underestimation of the bubble radius which happens to "reduce" the overall error in this instance.

When the Clapeyron equation is used, there is an under-prediction of the radius by both the AIT and SIT models. This is expected, as equation (3.33) under-predicts the initial vapour pressure. This can be further seen by comparing against the entirely inertial Rayleigh–Plesset equation, which under-predicts the bubble size. In this case, the error of the AIT model increases to 40%, matching the maximum errors seen in the MRG model, while the SIT model error increases to 60% as the inherent error in the model and the error in the temperature-pressure relationship compound. Interestingly, there is excellent agreement of the FIT equation, which does not capture the effects of capillarity and viscosity. The FIT model's over-predictions due to the absence of capillarity and viscosity appear to be compensated by the under-predictions of the temperature-pressure relationship.

1. It is for this reason, as has been shown in the derivation of the model, that it should only be applied when the inertial timescale τ_{RP} is greater than the thermal timescale τ_{MRG}.

3.5 Conclusions

Accounting for the changing inertial effects during the growth of an isolated vapour bubble has allowed the extension of the applicability of the existing bubble growth models. A new class of inertio-thermal (IT) models that capture the bubble's inertially-limited growth from rest, removing the singularity in the acceleration of the bubble that is present in other models. Excellent agreement with experimental and numerical data from literature as well as new MD simulations conducted here is shown.

The full inertio-thermal model (FIT) describes the growth of an isolated bubble in the absence of viscous and capillary effects, and will be most applicable for describing the growth of large vapour bubbles, where the effect of viscosity and capillarity is reduced. The approximate inertio-thermal model (AIT) provides an approximate solution to the FIT model, in a manner resembling the MRG model. Despite introducing some predictive errors, it captures the interplay between the thermal and inertial effects, with the effect of thermal diffusion becoming more relevant as the bubble grows from rest. When the timescale ratio between inertial and thermal growth is low, the simple inertio-thermal model (SIT) can be used. This provides a simple scaling of the velocity but does not account for the interplay between the thermal and inertial effects, treating them as independently changing parameters. In certain cases when inertial effects occur on a quicker timescale than the thermal effects, i.e. $\tau_{\mathrm{RP}} < \tau_{\mathrm{MRG}}$, the SIT model can give more accurate results than the AIT model despite its simpler form. This improved agreement is likely due to the cancellation of errors introduced in the model derivations (Theofanous & Patel, 1976) rather than a more accurate modelling of the problem. The exact criterion for when the intrinsic error in the SIT model outweighs the systematic error in the temperature-pressure relationship remains uncertain. However, it is hoped that this work will motivate further research into this topic and better complete the understanding of the interplay of inertial and thermal effects. The AIT and SIT models have the added advantage that they can include effects such as viscosity and capillarity, which are needed to accurately reproduce bubble growth rates. A flowchart indicating when each model should be used is given in figure 3.8

It is hoped that this improved understanding of homogeneous vapour bubble growth will lead to improvements in control of bubble systems. As technologies become more precise and more compact, understanding the growth behaviour of the full lifetime of vapour bubbles will become more significant. While there are additional modelling considerations that must be made to better represent these applications, such as the presence of a wall during heterogeneous bubble growth, the IT models introduced here represent the most accurate theoretical approach to predict homogeneous vapour bubble growth across all length and time scales.

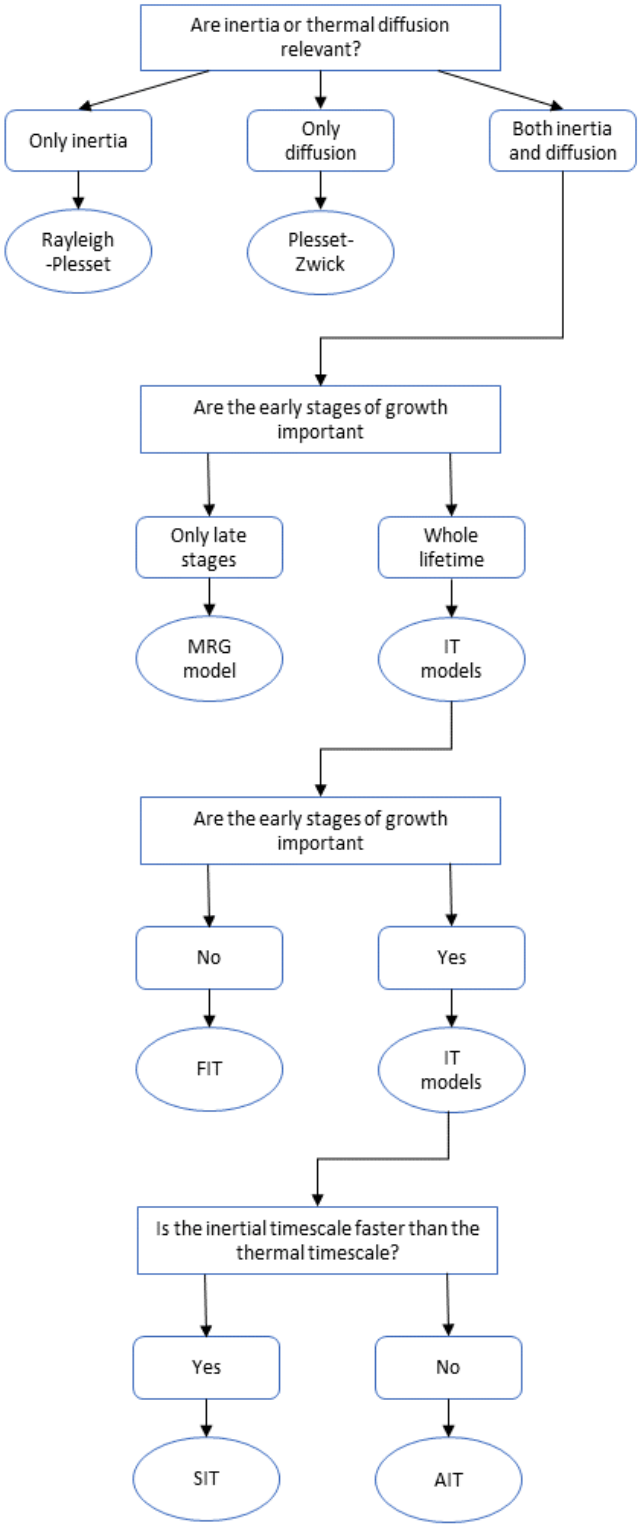

Figure 3.8: Flowchart indicating which homogeneous bubble growth model should be

Chapter 4

Heterogeneous Vapour Bubble Growth

The results of this chapter have already been published in: Sullivan, P., Dockar, D., Enright, R., Borg, M. K., & Pillai, R. The role of surface wettability on the growth of vapour bubbles *Int. J. Heat & Mass Trans.* (2023), vol. 217, 124657, and is available at doi.org/10.1016/j.ijheatmasstransfer.2023.124657

4.1 Introduction

Vapour bubble formation has been attributed as the driving factor behind natural phenomena, such as geyser formation and volcanic eruptions (Prosperetti, 2017). Similarly, the explosive failure of pressurised containers and wear of turbomachinery caused by cavitation bubbles, highlight the deleterious effects of vapour bubbles on industrial processes (Brennen, 2013). The high heat fluxes dissipated from surfaces during bubble formation and growth has seen pool boiling attracting significant interest in thermal management systems (Carey, 2018). Vapour bubbles appear across a range of both natural and engineered systems, and understanding heterogeneous vapour bubble growth growth is therefore an important question.

In the previous chapter, a more accurate approach to modelling the growth of homogeneous vapour bubbles was developed by including the changing inertial growth (rather than using a constant inertial limiting velocity) called the *inertio-thermal* bubble growth models. While these models are useful in the idealised case of perfectly-spherical bubbles growing in an infinite medium, in practice, bubbles typically form at a solid surface, where the barrier to nucleation is reduced (Kaschiev, 2000). This significantly changes the physics controlling the growth rate, as the presence of the solid surface alters the diffusive heat transfer in the liquid surrounding the bubble (Enríquez et al., 2014). To simplify the analysis of heterogeneous bubble growth, either spherical or hemispherical bubbles on a solid surface are typically analysed. Mikic et al. (1970) proposed a model for the growth of spherical bubbles at a wall, by using an error function solution to capture

the non-uniform temperature field close to a heated surface. However, the model did not account for the changes in diffusive heat transfer that arise in the surrounding liquid when a bubble grows on a wall, predicting identical results to their homogeneous bubble growth model in the case of a uniformly heated fluid. Indeed, they show a disagreement of a factor of approximately two with experimental results (Lesage et al., 2014). The altered thermal diffusive behaviour near the wall resembles the case of the growth of gas bubbles by species diffusion analysed by Enríquez et al. (2014), who showed how the solid surface halved the growth rate of spherical bubbles on a surface when compared to a homogeneous theory. This approach has not yet been adapted to analyse bubble growth driven by the unique thermal diffusion field from the surrounding liquid rather than species diffusion.

In the context of partially wetting bubbles, much of the existing literature has focused on the heat transfer into the bubble from the surface. Cooper and Lloyd (1969) developed a model for hemispherical bubble growth on a heated surface driven entirely by evaporation from the micro-scale layer of liquid that has been shown to form underneath bubbles, but neglecting heat transfer from the bulk fluid. This was seen as a reasonable approximation as the evaporation of the microlayer is often responsible for much of the heat transfer from the surface (Carey, 2018). Later, van Stralen et al. (1975) incorporated heat transfer through the bubble cap, in addition to the microlayer, using a laminar boundary layer heat transfer approximation. However, their model requires knowledge of the time taken by the bubble to leave the surface due to buoyancy, and therefore cannot be used to predict bubble growth *a priori*. While understanding the contributions of heat transfer from the surface is of great interest for thermal management applications, it is not the exclusive factor driving bubble growth and is of less significance for cavitation bubbles (Brennen, 2013). The Cooper and Lloyd (1969) and van Stralen et al. (1975) models additionally neglect the effect of the contact angle on bubble growth rate, only modelling hemispherical bubble growth. Despite the significance of wettability in bubble nucleation (Kaschiev, 2000) and departure (Carey, 2018), its effect on growth rate remains unexplored.

In addition to theoretical modelling, a wide range of experimental and numerical investigations have been performed on heterogeneous vapour bubble dynamics, typically focused on the departure of bubbles from heated surfaces (Chang et al., 2019; H. C. Lee et al., 2003; Lesage et al., 2014; Phan et al., 2010; Zhao et al., 2017). In these cases, surface wettability is typically measured using the contact angle of liquid droplets, however, Ardron and Giustini (2021) have recently shown that the presence of a nanoscale adsorbed layer underneath vapour bubbles alters the free energy balance that determines the shape of the bubble, indicating that contact angle measurements using droplets cannot always accurately predict the contact angle of vapour bubbles. Previous

continuum-based numerical investigations into the influence of surface wettability on vapour bubble dynamics were not capable of capturing the adsorbed layer, even after accounting for the changes to average near wall density (Gallo et al., 2021). Molecular dynamics (MD) simulations in contrast have been able to capture adsorbed layers underneath vapour bubbles (Datta et al., 2021; Maroo & Chung, 2008), making MD a promising tool for studying the complete physics of surface wettability on heterogeneous vapour bubble growth.

In summary, our understanding of heterogeneous bubble growth is currently limited to idealised approximations of bubble shapes and neglect the effects of the surface on the geometry of the bubble and diffusive heat transfer in the bulk liquid. It has been shown in literature that surface wettability plays a significant role in the formation and detachment of vapour bubbles, but there is currently little understanding of its effect on bubble growth, particularly in the early stages, when buoyancy is less relevant. In this chapter, the effects of the surface on the growth rate of heterogeneous vapour bubbles is analysed. The homogeneous growth rate model developed in the previous section is adapted to include the barrier to thermal diffusion introduced by the presence of a wall. The role of surface wettability in changing the shape of the bubble, and subsequently the thermal diffusive field surrounding the bubble is included in the model. The predictions of this model are then compared to the results of molecular dynamics simulations, showing good agreement provided the bubble shape can be accurately determined and the inertia can be approximated with spherical symmetry.

4.2 Development of Theoretical Model

In the previous chapter, the inertio-thermal (IT) models were developed which can be used when the timescale of the acceleration of the bubble is less than the timescale at which thermal effects become dominant in determining the bubble growth rate. The SIT model, from the previous chapter, predicts the radial velocity of an initially static vapour bubble using a combination of the radial velocities predicted by solving the RP equation $\dot{R}_{\mathrm{RP}}$ (equation (1.1)) and the MRG model $\dot{R}_{\mathrm{MRG}}$ (equation (3.9)):

$$\dot{R}_{\mathrm{IT}} = \frac{\dot{R}_{\mathrm{RP}}\dot{R}_{\mathrm{MRG}}}{\dot{R}_{\mathrm{RP,max}}}, \tag{4.1}$$

where the limiting velocity of the RP equation $\dot{R}_{\mathrm{RP,max}}$ is given by equation (3.2) as $\sqrt{2\Delta P/3\rho_l}$.

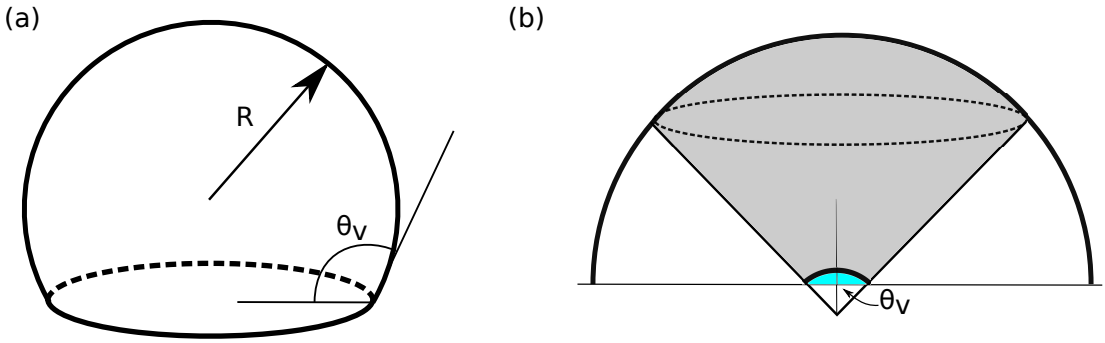

Figure 4.1: (a) Example of a spherical cap, defined by the bubble radius R and contact angle θ_v. (b) Comparison of the volume occupied by a hemisphere surrounding the heterogeneous bubble and the spherical sector of cone angle θ_v, shaded in gray. The contact angle of the vapour bubble (highlighted in blue) is identical to the cone angle that extends from its centre of curvature to the three-phase contact line.

In this chapter, this model will be adapted for the case of a heterogeneous bubble on an adiabatic surface. The appropriateness of the use of an adiabatic surface is investigated in section 4.4. This allows the effects of heat transfer from the surface to be neglected, and isolate the role of wettability in modifying diffusive heat transfer from the bulk liquid. This is achieved by modifying the terms of the energy balance at the bubble interface (given again in equation (4.2)) to account for the altered geometry of the bubble.

$$\rho_v h_{lv} \dot{V} = A q'', \tag{4.2}$$

For this analysis, the shape of the bubble will be assumed to be a spherical cap on the surface, shown in figure 4.1(a). The volume of a spherical cap V_{sc} can be expressed in terms of the volume of the sphere of equal radius V_{sp} as:

$$V_{sc} = V_{sp} \frac{(2 + \cos\theta_v)(1 - \cos\theta_v)^2}{4}, \tag{4.3}$$

where θ_v is the vapour side contact angle of the bubble, where $0 < \theta_v < 180°$. Similarly, the surface area of the spherical cap A_{sc} can be expressed in terms of the area of the sphere A_{sp} as:

$$A_{sc} = A_{sp} \frac{(1 - \cos\theta_v)}{2}. \tag{4.4}$$

Taking the ratio of these two scaling factors, i.e. the ratio of the volume scaling to surface area scaling of a spherical cap, gives:

$$\phi(\theta_v) = \frac{1}{2}(2 + \cos\theta_v)(1 - \cos\theta_v). \tag{4.5}$$

The energy balance from equation (4.2) can now be written for a spherical cap in terms of the sphere with the same radius and the factor ϕ as:

$$\phi(\theta_v)\rho_v h_{lv}\frac{d}{dt}V_{sp} = A_{sp}q''. \tag{4.6}$$

While equation (4.6) accounts for the geometrical differences in heat transfer at the bubble interface, it does not account for the change in available thermal energy due to the presence of the fixed wall. To account for this, we will assume that the available thermal energy is contained in a hemisphere around the bubble. The ratio of the volume of this hemisphere V_{hs} to the volume of the spherical sector V_{ss} of the same radius with a cone angle matching the bubble's contact angle gives a comparison of the difference in thermal energy surrounding the heterogeneous bubble compared to a homogeneous bubble of the same radius. This is illustrated in figure 4.1(b). This gives a further scaling factor on the heat flux of:

$$\frac{V_{ss}}{V_{hs}} = 1 - \cos\theta_v. \tag{4.7}$$

Dividing the scaling factor from equation (4.5) by the energy scaling factor in equation (4.7), an overall scaling factor for heterogeneous bubble growth $H(\theta_v)$ is obtained:

$$H(\theta_v) = \frac{A_{sc}/A_{sp}}{V_{ss}/V_{hs}} = \frac{1}{2}\left(2 + \cos\theta_v\right). \tag{4.8}$$

While it may be more intuitive to describe heterogeneous bubbles in terms of the vapour contact angle, in practise, surface wettability is widely described in terms of liquid contact angle θ_l. This is useful as the cosine of the liquid contact angle provides a dimensionless expression for the work of adhesion of the fluid on the solid (Israelachvili, 2011). Taking the liquid and vapour angles to be complementary $\theta_l = 180^\circ - \theta_v$, the heterogeneous scaling factor can be expressed in terms of θ_l as:

$$H(\theta_l) = \frac{1}{2}\left(2 - \cos\theta_l\right). \tag{4.9}$$

We can now express the growth rate of heterogeneous bubbles in terms of the equivalent homogeneous bubble growth rate $\dot{R}_{sp}$ as:

$$\dot{R}(\theta_l) = H(\theta_l)\dot{R}_{sp} = \frac{1}{2}\left(2 - \cos\theta_l\right)\dot{R}_{sp}, \tag{4.10}$$

which we call the heterogeneous inertio-thermal (HIT) model for vapour bubble growth.

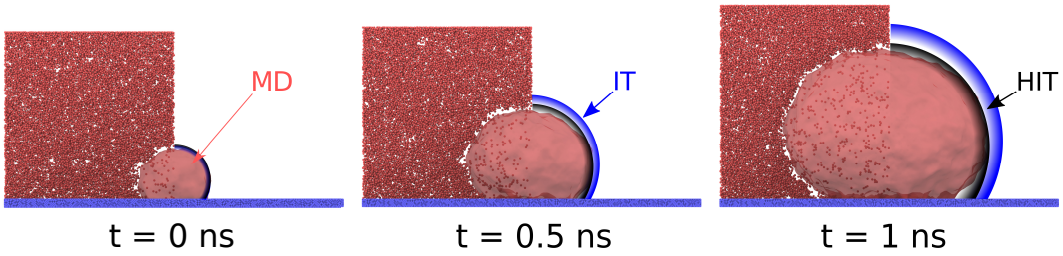

Figure 4.2: Simulation snapshot segments of a growing vapour bubble for $\theta_l = 70°$. The profile measured from MD is compared to the predictions of the homogeneous IT model and the heterogeneous HIT model. Some of the liquid molecules have been removed for visualisation purposes.

4.3 MD Results and Discussion

4.3.1 Comparison of Results to HIT model

In order to test the accuracy of the HIT model, we compare the predicted values of $H(\theta_l)$ to the values measured from MD simulation. Taking the radial velocities measured from MD as the heterogeneous values and the predictions of the homogeneous IT model at the same conditions of temperature, pressure, and initial radius, as the homogeneous values, we can rewrite equation (4.10) in terms of $H(\theta_l)$ to give:

$$H_{\mathrm{MD}}(\theta_l) = \frac{\dot{R}_{\mathrm{MD}}(\theta_l)}{\dot{R}_{\mathrm{IT}}}, \tag{4.11}$$

where $\dot{R}_{\mathrm{MD}}(\theta_l)$ is the heterogeneous bubble radial velocity measured from MD on a surface with a droplet contact angle of θ_l, and $\dot{R}_{\mathrm{IT}}$ is the growth rate predicted from the homogeneous IT model.

Figure 4.2 shows the measured profile of a growing vapour bubble for $\theta_l = 70°$ alongside the IT (homogeneous) and HIT (heterogeneous) predictions. The resulting MD measured values of $H(\theta_l)$ are shown in figure 4.3(a), compared to the theoretical HIT factor (equation (4.9)).

Figure 4.3 illustrates the three distinct regimes depending on surface wettability. For the *neutral wetting regime* (when $-0.5 < \cos\theta_l < 0.5$), we see excellent agreement with the HIT model predictions. Compared to an equivalent homogeneous bubble, we see an increased growth rate on the less wetting surfaces and a decreased growth rate on the more wetting surfaces, matching our theoretical predictions. In the *hydrophobic regime* ($\cos\theta_l < -0.5$) and the *hydrophilic regime* ($\cos\theta_l > 0.5$), we see greater bubble growth rates than those predicted by the HIT model, which will be discussed in the next two sections.

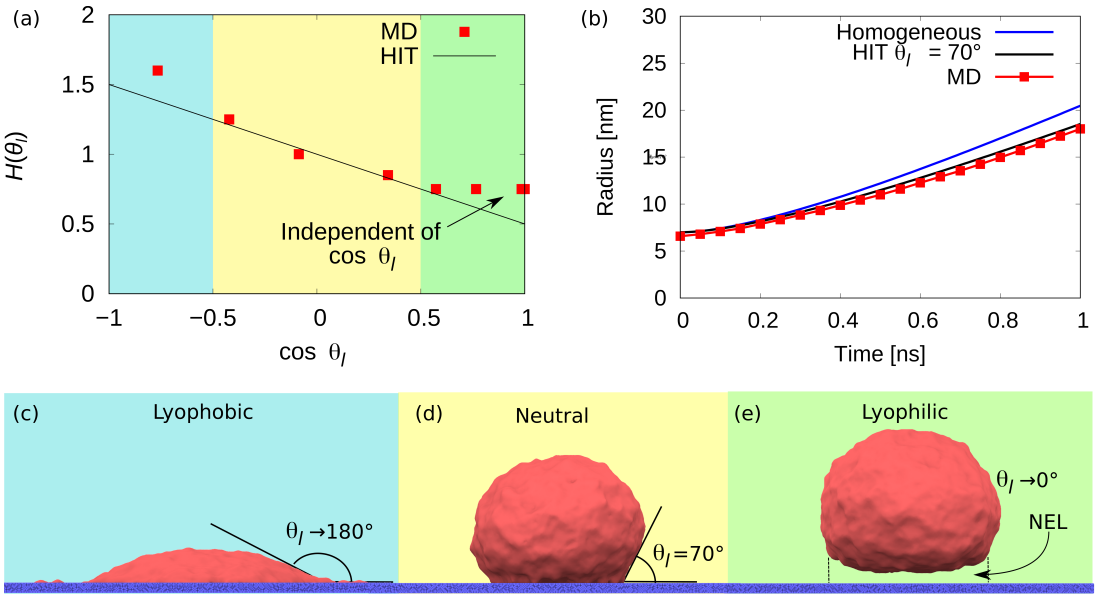

Figure 4.3: (a) Measured heterogeneous scaling factors from MD simulation compared to the HIT model predictions. (b) Measured radius of vapour bubble with $\theta_l = 70°$ from MD compared to homogeneous and heterogeneous models. Bubble profiles seen in the (c) hydrophobic, (d) neutral, and (e) hydrophilic regimes. A non-evaporating layer forms underneath the bubble in the hydrophilic regime.

4.3.2 Hydrophilic Regime

For highly-wetting surfaces, we see in figure 4.3(a) that the measured bubble growth rates exceed the rates predicted by the HIT model ($H(\theta_l) \approx 0.75$ once $\cos\theta_l > 0.5$). Interestingly, the HIT factor measured across these cases is independent of wettability, which can be seen in figure 4.3(a), where the measured cases approach a constant value instead of following the HIT trajectory predicted by surface wettability alone. This result can be explained by analysing the contact angle of static vapour bubbles on these surfaces. Figure 4.4(a) shows the size dependence of the equilibrium contact angle θ_0 of the vapour bubbles measured relative to the surface for various surface wettabilities (i.e. for varying θ_l) from separate NVT simulations. From this plot we can see that θ_0 is independent of bubble radius for $\theta_l > 70°$ (i.e. they appear as a flat, horizontal line), and dependent on bubble radius for $\theta_l \leq 70°$ (i.e. they appear as tilted lines with a negative slope). When the equilibrium contact angle is independent of radius, the measured bubble contact angles θ_0 match the liquid contact angle measured from droplet simulations ($\theta_0 \approx \theta_l$). When the equilibrium contact angle is dependant on radius, the relationship between θ_0 and θ_l no longer holds. Instead, we see an interesting trend in the *limiting value of* θ_0 as the bubble radius becomes larger (and $R^{-1} \to 0$). For each of these cases, figure 4.4(a) shows that the equilibrium contact angle tends to a similar value of $\theta_0 \approx 60°$.

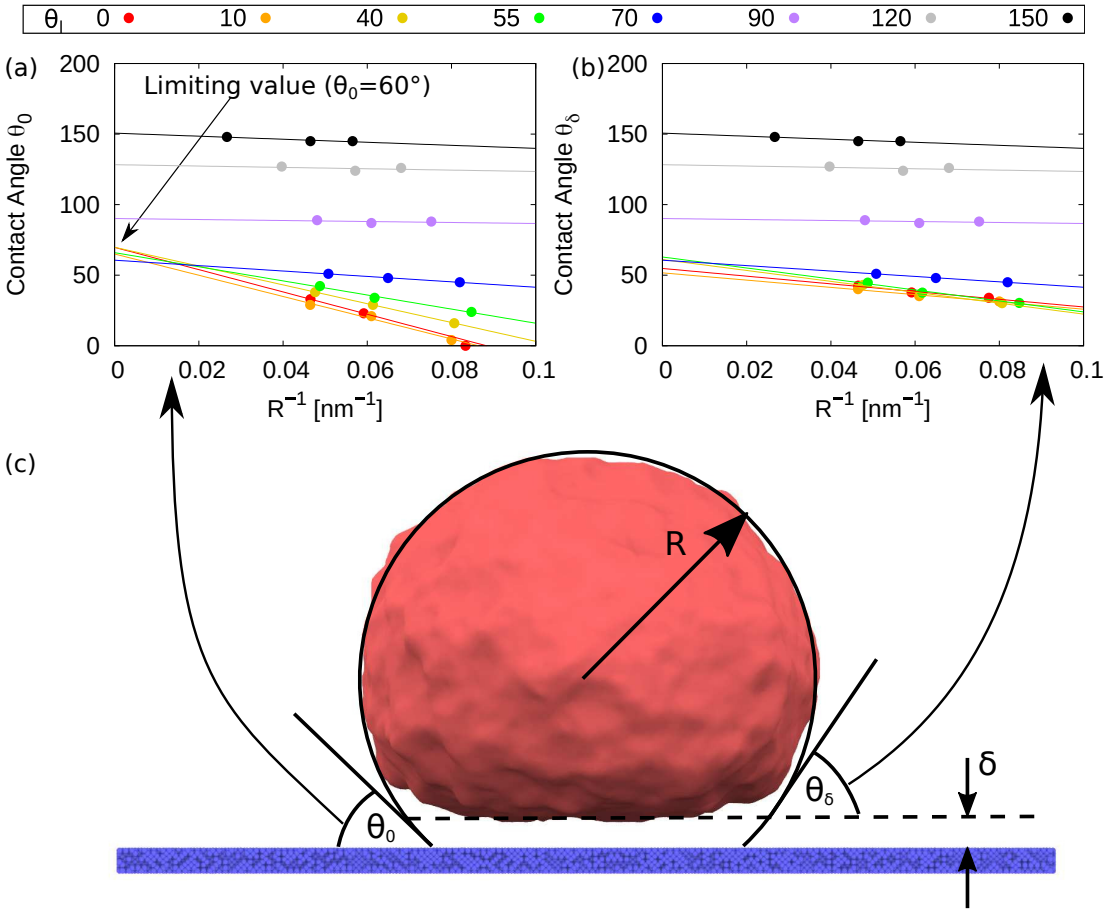

Figure 4.4: Comparison of liquid contact angles measured against the (a) solid substrate θ_0 and (b) non-evaporating layer θ_δ. (c) Schematic highlighting the difference between the two measurements. Note the separation of the bubble from the surface by a distance of δ due to the non-evaporating layer.

This behaviour can be explained by the formation of a non-evaporating layer (NEL) underneath the bubble (see figure 4.3(e)). This NEL forms due to surface adsorption of molecules once $\theta_l < 70°$, and has been shown to break the complementary nature of bubble and droplet contact angles (Ardron & Giustini, 2021). Instead of measuring the contact angle of the bubble relative to the solid surface θ_0, we can alternatively measure the contact angle relative to the the top of the NEL θ_δ (a schematic representation of the differences between these two measurements of contact angle is shown in figure 4.4(c)), again for different θ_l as shown in figure 4.4(b). We now see that the contact angle of the bubble becomes independent of surface wettability when a NEL forms, indicated by the collapsing of all cases onto a single line once $\theta_l < 70°$. This shows that the presence of the NEL fundamentally alters the bubble-surface interaction when compared to a bare surface. This leads to two fundamental questions: (a) by what mechanism does the NEL influence the contact angle behaviour? and (b) when and why does the NEL form?

Influence of NEL: We hypothesise that the first question, i.e. the change in the contact angle behaviour, can be attributed to the NEL changing the interfacial stress balance at the contact line. In these cases the NEL partially shields the bubble from the influence of the surface. To understand this process better, we need to quantify the variation in the interfacial stresses present in the NEL.

In the cases where a NEL forms, the solid-vapour interface effectively becomes a solid-NEL-vapour interface, with a notable effect on the resulting interfacial stress. Figure 4.5(a) shows how the cumulative stress changes with distance for both the $\theta_l = 70°$ and $\theta_l = 10°$ cases. We can see for the $\theta_l = 10°$ case that there is a noticeable effect from layering of molecules near the surface for both the solid-liquid and solid-vapour measurements. There is a slight offset in the location of these peaks between the solid-liquid and solid-vapour curves, this is due to the difference in far field pressure in the bulk liquid and inside the vapour bubble caused by the Laplace pressure. For $\theta_l = 70°$, the layering is only visible in the liquid. As there is no NEL, there is no layering observed in the solid-vapour cumulative stress profile. Thus the presence of the NEL significantly affects the interfacial stresses, which in turn must influence the contact angle, which we will demonstrate next. By measuring the liquid-vapour, solid-liquid, and solid-vapour interfacial stresses, γ_{lv}, γ_{sl}, and γ_{sv} respectively (as outlined in section 2.5.2), we can predict the resulting contact angle using Young's equation:

$$\cos\theta_Y = \frac{\gamma_{sl} - \gamma_{sv}}{\gamma_{lv}}. \tag{4.12}$$

Figure 4.5(b) compares the angle predicted by Young's equation (equation (4.12)) with the geometrically measured angles from our MD simulations (shown previously in figure 4.4(b)). We see good agreement between the predicted Young's angle θ_Y and the measured NEL-based contact angle θ_δ across the full range of wettabilities. This confirms that the NEL is responsible for the fixed θ_δ when $\theta_l < 70°$.

Formation of NEL: There remains the second question about why and when the NEL forms. To answer this, we develop a criterion based on the potential energy barrier that a molecule would need to overcome in order to evaporate from the surface. The potential barrier consists of the attractive potential from the wall (PE_{wall}) as well as from the pressure in the vapour (PE_{vapour}), effectively pushing molecules towards the surface. We hypothesise that if the kinetic energy (KE) of the molecules is greater than this attractive potential barrier, then molecules are capable of escaping from the potential well, and the NEL does not form. Conversely, if the kinetic energy is less than the potential barrier, the molecules lack sufficient energy to escape from the surface and

the NEL forms. We can then express this NEL formation criterion as:

$$KE - PE_{wall} - PE_{vapour} < 0. \tag{4.13}$$

This is similar to the *PK norm* measurement proposed by Y. J. Chen et al. (2020), who considered the local potential and kinetic energy to predict the location of bubble nucleation sites. Comparing the value of this criterion to our contact angle observations in figure 4.5(b), we can see good agreement with our simulation results. The change in sign of our NEL criterion, expected to occur when the potential barrier exceeds the available kinetic energy, occurs exactly when the NEL forms ($\theta_l \approx 70^\circ$) and the bubble contact angle becomes independent of wettability. This provides additional evidence that the formation of the NEL is responsible for the disparities between the different contact angle measurements.

We can thus clearly see that the presence of the NEL causes the liquid-side contact angle of the vapour bubble θ_δ to deviate from predictions of a droplet analysis. When the bubble growth data is compared to the HIT theory using the measured contact angles from bubble simulations (i.e. θ_δ, figure 4.6) rather than the values obtained from droplet simulations (i.e. θ_l, figure 4.3 (a)) we see significantly improved agreement in the hydrophilic regime. This indicates that while using droplet contact angles is useful for non-dimensionalising the wettability, they are not appropriate for analysing bubble systems when the NEL is present (Ardron & Giustini, 2021).

4.3.3 Hydrophobic Regime

Moving from the hydrophilic to the hydrophobic regime, the bubble assumes a flat, pancake-like shape in the latter case (see figure 4.3(c)), and can no longer be well analysed using spherical symmetry. The inertia of the system is therefore no longer well described by the RP equation, where the maximum growth velocity is independent of domain size. We can show that in the non-wetting limit (i.e. $\cos\theta_l \to -1$) the growth rate strongly depends on domain size. Indeed, in this limit the system simplifies to a 1D Stefan-type problem (Malan et al., 2021). A simple simulation setup to highlight this is shown in figure 4.7(a). The system is equivalent to the setup used previously except that a slab of fluid, and not a spherical cap, is removed to produce the bubble. This is equivalent to simulating a completely non-wetting spherical cap, where any volume of vapour would produce an infinite radius of curvature bubble. The amount of fluid removed from the system was adjusted to provide different initial heights of liquid h, creating different effective domain sizes with fluid sections of different mass.

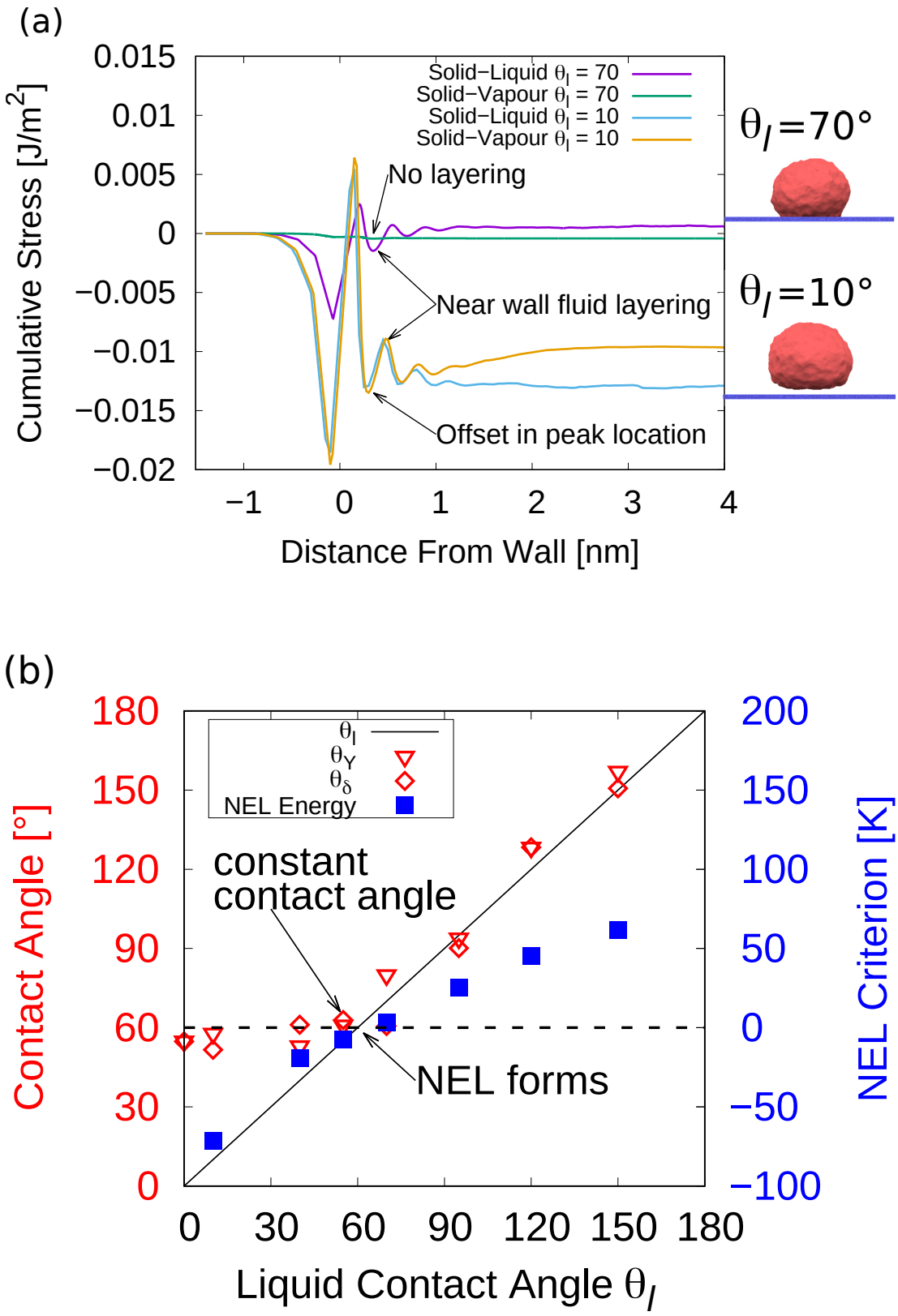

Figure 4.5: (a) Interfacial stress measurements of the solid-liquid and solid-vapour interfaces for liquid contact angles of 10° and 70°. (b) Liquid contact angles predicted by Young's equation θ_Y compared to those measured from MD simulation θ_δ. The predicted angle reaches a constant value as the NEL formation criterion changes sign.

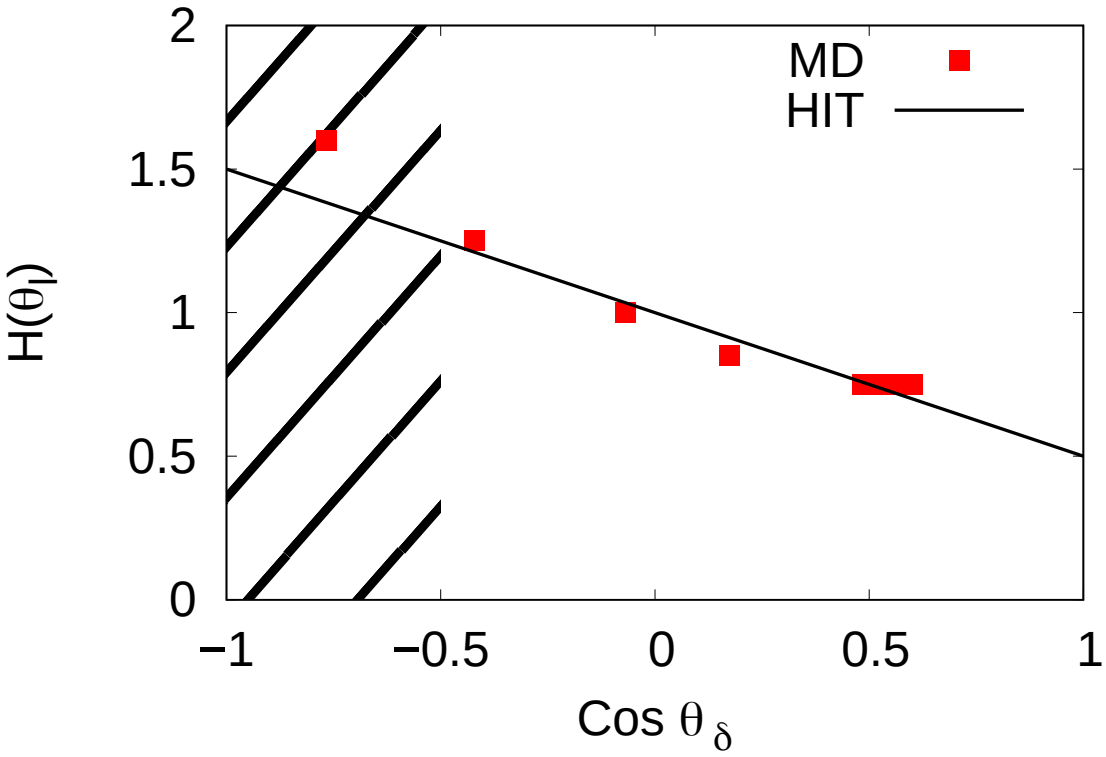

Figure 4.6: Measured heterogeneous scaling factors from MD simulation compared to the HIT model predictions with measured liquid contact angle θ_δ. The hatched region where $\cos\theta_\delta < -0.5$ indicates where the model predictions do not hold in the hydrophobic regime. The grouping of points around $\cos\theta_\delta = 0.5$ is due to the formation of the NEL.

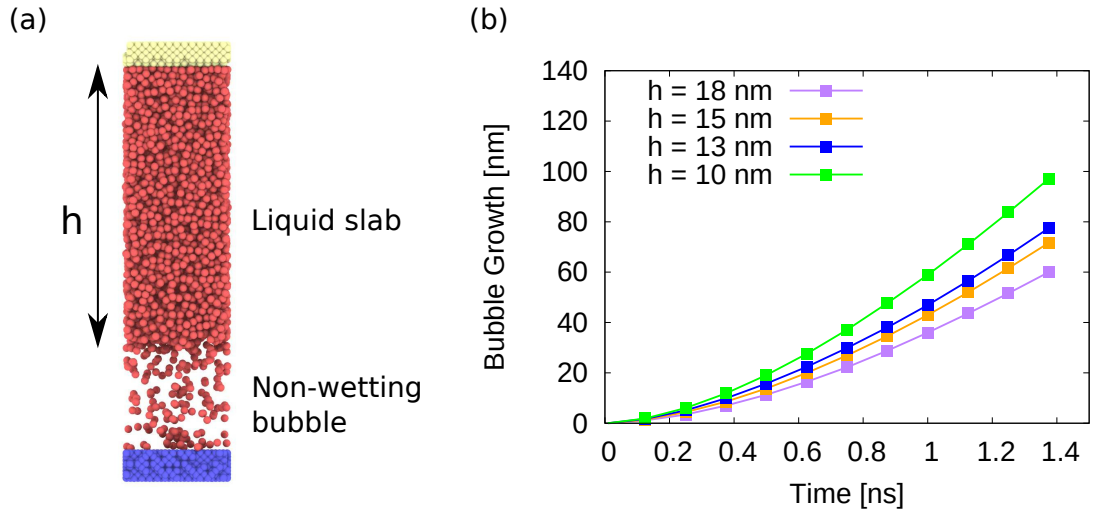

Figure 4.7: (a) Non-wetting bubble growth rates for various liquid slab heights measured from MD. Solid lines represent a linear modified IT model. (b) Schematic of the MD simulation setup used for non-wetting bubble tests.

From figure 4.7(b), we can see that as the height of the liquid layer is decreased, there is an increase in the bubble growth rate. Due to the greater inertia, the greater mass of fluid linearly accelerates at a slower rate. This highlights the inapplicability of the assumption of spherical symmetry in the force balance at the bubble interface. We are therefore unable to apply the HIT model to describe the growth of hydrophobic bubbles.

4.4 Effect of Surface Heat Transfer

The analysis presented in the main text investigates bubble growth where heat transfer occurs only from the surrounding liquid. In practise, particularly for large bubbles, heat transfer from the surface may become important. The effects of surface heat transfer on bubble growth rate are investigated by allowing heat transfer between the fluid and surface during the MD simulations. This involves the time integration of the wall molecules in the NVT ensemble, thermostatted to the same initial temperature as the fluid, rather than the non-thermalised, non-time integrated wall used for the adiabatic investigations. Figure 4.8 shows a comparison of measured bubble growth rates on an adiabatic and a diabatic surface. This shows that in the timescales investigated, there is negligible effect of surface heat transfer on bubble growth rate. This is likely, in part, due to the high superheats used in these investigations, providing significant thermal energy in the region surrounding the bubble. As the bubbles being modelled increase in size and as the superheats modelled decrease, it is expected that the effect of surface heat transfer will become more significant.

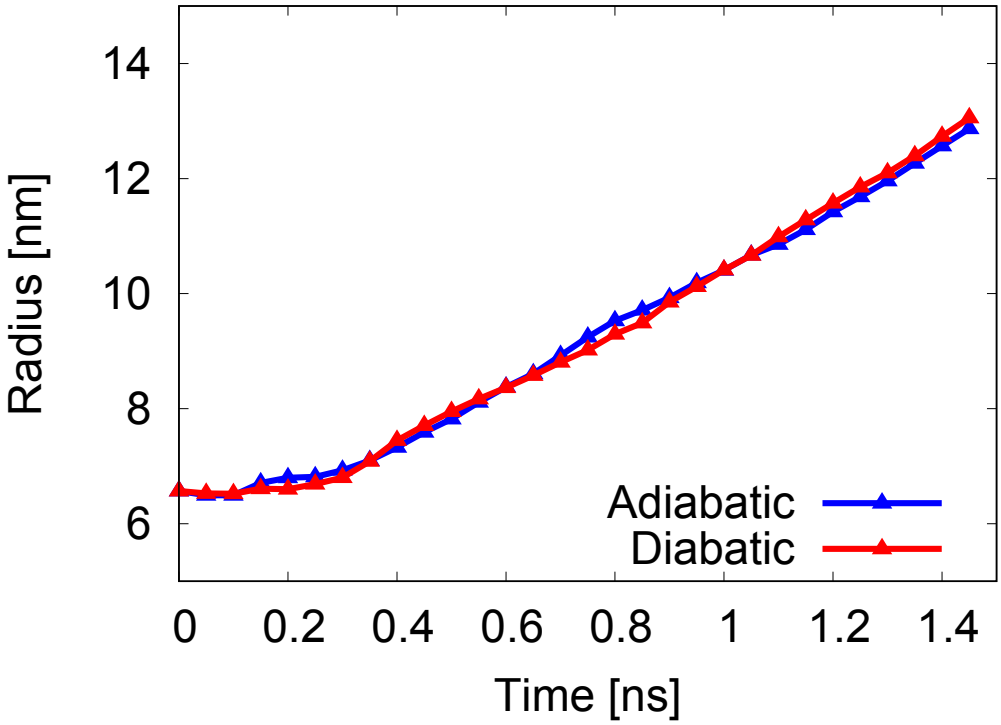

Figure 4.8: Comparison of bubble growth rates on adiabatic and diabatic surfaces for $\theta_l \approx 90°$.

4.5 Conclusions

In this chapter, a new heterogeneous inertio-thermal (HIT) model is developed by extending the homogeneous inertio-thermal model from the previous chapter. This is achieved by accounting for the effect of the surface on thermal diffusion. The model scales the bubble surface area and volume terms in the interfacial energy balance to that of an equivalent spherical cap. Additionally, the available thermal energy is scaled to be contained in a spherical cap around the bubble rather that the spherical sector that the equivalent homogeneous bubble would have available.

Three distinct regimes of bubble growth are identified. For the neutral wetting regime ($-0.5 < \cos\theta_l < 0.5$), we see excellent agreement of the HIT model predictions, with an increased growth rate observed for less wetting fluids and a decreased growth rate for more wetting fluids. Secondly, in the hydrophobic regime ($\cos\theta_l < -0.5$), the inertia of the system can no longer be well described by the spherical symmetry of the Rayleigh–Plesset equation and therefore cannot be accurately modelled. It is shown that in the limiting case, these systems are strongly dependent on domain size. Finally, in the hydrophilic regime ($\cos\theta_l > 0.5$), a non-evaporating layer (NEL) of adsorbed molecules forms on the surface underneath the bubble. The NEL substantially alters the interfacial stress balance at the contact line, causing the measured contact angle of the bubble θ_δ to differ from the complement of the liquid contact angle i.e. $\theta_\delta \neq \theta_l$. We show that when the NEL forms, the correct bubble growth dynamics can still be obtained if the liquid contact angle measured from the top of the NEL (θ_δ) is used instead of the value obtained from droplet measurements θ_l in the HIT model.

Chapter 5

Vapour Bubble Nucleation

This chapter contains preliminary results of an investigation into the nucleation of vapour bubbles on surfaces with varying wettabilities and topographies.

5.1 Introduction

The previous chapters have focused on the growth of vapour bubbles after they have formed. While an improved understanding of the key physics controlling growth has been found, there remain open questions on the formation of vapour bubbles. Understanding the physics governing the nucleation of vapour bubbles has been the focus of much applied research due to the numerous industrial applications. Where bubble formation is desired, such as in two-phase thermal management systems, significant research has been performed into understanding how surface wettability and roughness can optimise the onset of nucleate boiling (Betz et al., 2013; Bourdon et al., 2013; Chu et al., 2013). Similarly, where heterogeneous bubble formation is undesirable, such as in turbomachinery or in bubble chambers (Kozynets et al., 2019; Prosperetti, 2017), much work has been performed to suppress the formation of bubbles on the solid surface (Reinke, 1997).

Understanding the kinetic limit of superheat, or the maximum temperature at which a fluid can be heated before nucleation occurs, is therefore of significant interest. While many investigations have been performed in to the effects of surface modifications on nucleation (Gallo et al., 2021; Lavino et al., 2021; Liang & Mudawar, 2021), there remain outstanding questions on the combined effects of surface roughness and wettability. Experimental investigations into the individual effects of wettability on nucleation require the manufacturing of surfaces with identical roughness. This is quite difficult to achieve in practice, even for highly smooth experimental surfaces. Decoupling the effects of the change in wettability and change in roughness on different surfaces on the nucleation of vapour bubbles has proven difficult experimentally (Kim et al., 2011), which can make comparison to theory uncertain.

The role of surface roughness in enhancing the nucleation rate of vapour bubbles is widely reported (Carey, 2018). Surface cavities provide areas with a reduced Gibbs free energy barrier, forming active sites for nucleation. Lorenz et al. (1974) have developed a geometrical model for nucleation site activation, based on the assumption of conically shaped cavities. This model assumed that vapour becomes trapped in the cavities as the surface is wetting, forming pre-existing sites from which bubbles can grow. This analysis is based on macroscale and continuum assumptions, neglecting effects such as the non-evaporating layer discussed in the previous chapter. The activation mechanism for nanoscale nucleation sites is thus not fully understood.

In this chapter, the independent roles of surface wettability and roughness on vapour bubble nucleation are investigated. By adjusting the wettability of identical, atomically smooth surfaces, the predictions of nucleation theory are tested. Excellent agreement is seen between the theoretical predictions of nucleation temperature and the results from MD, provided an accurate homogeneous baseline. The effect of surface roughness on nucleation temperature is also investigated. The inclusion of a simple conical cavity is shown to reduce the temperature required for nucleation only under certain circumstances. In both extremes of wettability, nanoscale roughness is shown to provide no reduction in nucleation temperature, an initially surprising results in the context of existing theories (Carey, 2018; Lorenz et al., 1974). This can be explained by considering two factors. Firstly, in the hydrophilic case, the free energy barrier inside the cavities is not significantly reduced when compared to the bulk fluid. This is due to the strong fluid-solid interactions, keeping the fluid in a dense, liquid state. In the hydrophobic limit on the other hand, even though the surface cavities dewet, the radius of the bubbles that form on smooth surfaces can exceed the radius of the cavity. In this case, the cavities are shown to play no role in enhancing nucleation.

5.2 Nucleation kinetics

While the thermodynamics of nucleation as described in section 1.3 can determine the Gibbs free energy barrier to nucleation and the size of the critical nucleus, it does not tell us about the likelihood of this barrier being overcome and a critical nucleus forming. This energy barrier ΔG_c measures the free energy penalty that must be overcome in order for a nucleus to reach the critical size. The kinetics of nucleation theory investigates the rate J at which critical nuclei can be expected to form. In the case of isothermal nucleation at constant supersaturation, the nucleation rate can be expressed as (Kaschiev, 2000; Tanaka et al., 2015):

$$J = \alpha e^{-\Delta G_c / k_B T}. \tag{5.1}$$

The exponential term shows that the energy barrier ΔG_c plays a significant role in determining the nucleation rate. The prefactor α determines the kinetic contribution to the nucleation rate and can be expressed as:

$$\alpha = \Gamma \sqrt{\frac{c^3 \gamma}{18\pi^2 m_0}} C_0. \tag{5.2}$$

This depends on molecular mass of the particles m_0 and a particle attachment factor Γ, which is typically taken as unity (Kaschiev, 1970; Rosales-Pelaez et al., 2019). C_0 is the density of nucleation sites, with units of m^{-3} for homogeneous nucleation and m^{-2} for heterogeneous nucleation. The effect of the shape of the nucleus is captured in c^3, a factor which for spherical caps is given as:

$$c^3 = \frac{36\pi}{2 + \cos\theta}. \tag{5.3}$$

In the case of spherical nuclei, this shape factor simplifies to 36π. The units of this kinetic factor, and therefore the nucleation rate, are determined by the units of C_0, the concentration of active sites for nucleation. In the case of homogeneous nucleation, C_0 has units of sites per unit volume. For pure substances, there are no alternative nucleation sites, and so the site density is equal to the particle number density (Rosales-Pelaez et al., 2020). The nucleation rate J will then have units of nucleation events per unit volume per unit time. For heterogeneous nucleation, the site density is given as the number of active sites per unit surface area, which for atomically smooth surfaces is one site per unit lattice surface area. This value can vary significantly for irregular surfaces depending on the surface geometry and subsequent number of preferential nucleation sites (Carey, 2018). Roughness on the solid surface often allows for pre-existing nuclei to reduce the energy barrier to nucleation, causing a significant increase in nucleation rate and allowing nucleation to occur at lower supersaturations (Chu et al., 2013; Novak et al., 2008).

In the context of vapour bubbles, it is again useful to express the nucleation rate in terms of ΔP (Kaschiev, 2000):

$$J = \alpha e^{-B/\Delta P^2}. \tag{5.4}$$

Here the thermodynamic parameter B is given by

$$B = \frac{4c^3 \psi(\theta)\, \sigma^3}{27 k_B T}, \tag{5.5}$$

which is a function of both temperature and the shape of the nucleus. Here $\psi(\theta)$ represents the scaling factor of the volume of the spherical cap with contact angle θ to the volume of a sphere of the same radius and is given by:

$$\psi(\theta) = \frac{(2 + \cos\theta_v)\,(1 - \cos\theta_v)^2}{4}. \tag{5.6}$$

5.3 Simulation of Nucleation

As the formation of vapour bubbles is an activated event due to the presence of the free energy barrier, traditional continuum modelling cannot accurately capture nucleation. Numerical studies have therefore either utilised non-continuum models or seeded their simulations to bypass the energy barrier.

Diemand et al. (2014) performed molecular dynamics (MD) simulations of a large block of over 5×10^8 fluid molecules. This system was initially equilibrated with a Nosé–Hoover thermostat in a superheated state before micro-canonical (NVE) simulations were performed allowing vapour bubbles to nucleate. They showed good agreement between their simulation results and the predictions of classical nucleation theory for both the critical nucleus size and nucleation rate. They showed a slightly reduced nucleation rate when compared to the results of Wang et al. (2009), who utilised forward flux sampling to compute nucleation rates from MD. This may due to statistical effects, as nucleation in these simulations is driven by thermal fluctuations and localised hot spots. Denzel et al. (2016) later investigated the formation of vapour bubbles due to localised energy spikes in the fluid, similar to those expected from cosmic rays.

Rosales-Pelaez et al. (2019) performed MD simulations of seeded vapour nuclei in the isothermal-isobaric (NPT) ensemble to compute the free energy barrier of critical bubbles. They use these calculations, along with kinetic analysis to predict nucleation rates with good success. The same authors later adapted this technique, performing their seeding simulations in the isothermal-isochoric (canonical/NVT) ensemble, showing good agreement with their previous work (Rosales-Pelaez et al., 2020). This approach allows for stable, critically-sized bubbles to be produced, as the bubble will grow or shrink in size, changing the pressure in the liquid, until it reaches an equilibrium. The authors could then measure the equilibrium properties of their critical bubble and confirm the agreement with CNT.

Gallo et al. (2018) developed a continuum diffuse-interface model with a fluctuating hydrodynamic contribution to account for thermal fluctuations in the density of the system. This noise contribution allowed for sufficiently high fluctuations in density that critical nuclei form and grow in the bulk liquid, showing good agreement with the

nucleation rates predicted by CNT. The major advantage of this model is a significantly reduced computational cost when compared to non-continuum models such as MD. This model was later adapted to capture bubble nucleation on neutral wetting surfaces (Gallo et al., 2020) and subsequently on surfaces with varying wettability (Gallo et al., 2021). While the wettability model is capable of capturing density changes of the fluid near the surface, it does not capture the layering of fluid molecules seen in non-continuum simulations.

As shown in the previous chapter, the fluid-solid interactions that cause this layering of molecules near the surface is responsible for the formation of a non-evaporating layer underneath heterogeneous vapour bubbles. This layer has been observed to form underneath bubbles that nucleate on hydrophilic surfaces through both surface heating (Lavino et al., 2021) and from pressure oscillations caused by surface acoustic waves (Datta et al., 2021), showing the independence of this layer on the method of bubble formation. This layer has been investigated due to its potential role in the formation of the evaporation microlayer underneath heterogeneous bubbles (Maroo & Chung, 2008, 2009). This highlights the importance of including these near-wall effects in studies of heterogeneous nucleation.

Due to its ability to not only capture the nucleation of vapour bubbles but also capture the fluid-structure interaction on the molecular scale, MD has proved a popular tool for modeling heterogeneous vapour bubble nucleation. Early simulations from Maruyama and Kimura (1999) and Kinjo et al. (1999) showed that MD was indeed capable of capturing heterogeneous nucleation. Vapour bubble nucleation on a solid surface was achieved by isothermally decompressing a fluid contained between two walls until a void formed in the fluid. Simulations from Novak et al. (2008) showed that even in the absence of trapped gases, nucleation occurs preferentially in surface cavities. These findings were later supported by many other authors, using a variety of different surface structures (Y. Chen et al., 2018; Y. J. Chen et al., 2020; Lavino et al., 2021; She et al., 2016). Notably among these is the work of Liu et al. (2019), who tested boiling on surfaces with fractal roughness, showing an increased heat transfer rate and earlier onset of nucleation on rougher surfaces.

The wettability of the surface can be easily controlled in MD simulations by adjusting the interaction strength between the fluid and solid (Barrat & Bocquet, 1999). This has allowed for the effect of surface wettability on nucleation to be investigated. Yamamoto and Matsumoto (2012) performed MD simulations of fluids on heated surfaces with various wettabilities. There simulations showed that nucleation occurred faster on hydrophilic surfaces, in apparent disagreement with CNT. This finding can be explained by the reduced Kapitza resistance of the more wetting surface (Y. J. Chen et al., 2020). This is further supported by Zhou et al. (2019), who demonstrated a change in the

preferential wettability for nucleation with temperature. They demonstrated that on cooler walls nucleation occurs preferentially on a hydrophobic surface but as the wall temperature increases the higher heat transfer rate on hydrophilic surfaces overcomes the increased nucleation barrier. These findings have been supported by many other authors (Y. J. Chen et al., 2020; Diaz & Guo, 2017). This highlights the importance of accounting for the timescales at which molecular simulation can be performed when attempting to extrapolate findings to the macroscale.

5.4 Effect of Surface Wettability

To determine the effect of wettability on nucleation rate, a baseline value to compare against is needed. In order to find this reference value for nucleation rate, homogeneous nucleation simulations are performed using MD. In order to guarantee homogeneous nucleation, the simulation domain must consist of exclusively fluid molecules. The temperature and pressure of the system can then be controlled in the NPT ensemble. This ensures that the thermodynamic state of the system at the moment of nucleation is known.

The simulation methodology employed for this investigation involves slowly raising the temperature of an isobaric fluid until nucleation occurs. Initially, the system is equilibrated to a constant pressure of 0.1 MPa and temperature of 100 K. While this is a supersaturated state for liquid Argon, the supersaturation is not sufficient for nucleation to occur in the time and length scales practically achievable with MD. The temperature of the system is then raised to increase the supersaturation. This is achieved using a two step process; firstly, the system temperature is ramped up from its starting temperature T_0 to a higher temperature $T_0 + \delta T$. This is done over a time-frame of 0.5 ns to minimise transient effects from rapidly heating the fluid. The fluid is then allowed to equilibrate again at this higher temperature for a further 0.5 ns. These timescales were chosen to allow for sufficient time to elapse during the simulations for nucleation to occur and be detected, while not providing too much of a computational cost. This process is then repeated until nucleation occurs. The value of δT used was initially 2 K to find an approximate nucleation temperature, before a secondary run with smaller increments of 0.5 K to more precisely measure the nucleation temperature.

To measure homogeneous nucleation rates, the simulations are performed using a cubic simulation domain of length 10 nm with periodic boundary conditions consisting of just fluid molecules. This simulation is performed in the NPT ensemble, where the temperature and pressure of the homogeneous fluid can be controlled. The homogeneous nucleation temperature for Argon at 0.1 MPa was measured to be 134 K. Using the fluid properties of Argon at this temperature, equation (5.4) predicts a nucleation rate

of $10^{28}\,\mathrm{m^{-3}s^{-1}}$. In order to compare this value with heterogeneous simulations, the rate must be scaled by the volume of the simulation domain, which in this case is approximately $10^{-24}\,\mathrm{m^3}$. This gives an expected number of 10^4 nucleation events per second. While this is approximately 5 orders of magnitude off the value observed in the simulations (where a nucleation event is observed on the scale of nanoseconds), this is typically considered a "good" agreement for measures of nucleation rate (Rosales-Pelaez et al., 2019), which can vary by several orders of magnitude with a 1K change in temperature.

The theoretical homogeneous nucleation events per second is then used as a reference to predict the heterogeneous nucleation temperatures. The nucleation rates from equation (5.4) are calculated for various contact angles across a range of temperatures. These calculated rates can then be scaled by a surface area to produce an expected number of nucleation events per second. In the case of this work that is $4 \times 10^{-16}\,\mathrm{m^2}$. The temperature at which the predicted number of heterogeneous nucleation events per second exceeds the homogeneous threshold value can be taken as the heterogeneous nucleation temperature.

In order to test heterogeneous nucleation theory, a solid surface is needed on which nucleation can occur. The set up described in section 2.6 is employed to control the system pressure. Due to its interaction with the solid surface, the LAMMPS implementation of a barostat is not appropriate for this investigation and the use of a piston is necessary. The same simulation methodology of slowly ramping the temperature of the fluid under a constant pressure before an equilibrium step is used for these heterogeneous nucleation simulations. By varying the fluid-solid interaction, as in the heterogeneous growth simulations, the effect of surface wettability on nucleation temperature can be investigated.

The plot in figure 5.1 shows the measured effect of surface wettability on nucleation temperatures from MD simulation compared to the predictions from CNT. There is good agreement between the CNT predictions and measured temperatures across the whole range of wettabilities. In line with the reduced barrier to nucleation, there is a reduced nucleation temperature on the non-wetting surfaces. Interestingly the nucleation temperature reaches a constant value of 134 K for the wetting surfaces (i.e. for $\theta_l \leq 90°$), matching the value for the homogeneous case.

According to a purely thermodynamic analysis, the energy barrier for homogeneous nucleation is always greater than for heterogeneous nucleation. However, once the kinetics of nucleation are accounted for, higher nucleation rates may be achieved homogeneously for highly wetting surfaces. For scenarios where the greater number of homogeneous nucleation sites in the bulk fluid outweighs the reduced energy barrier of nucleation at the surface, higher nucleation rates are predicted homogeneously than heterogeneously. This

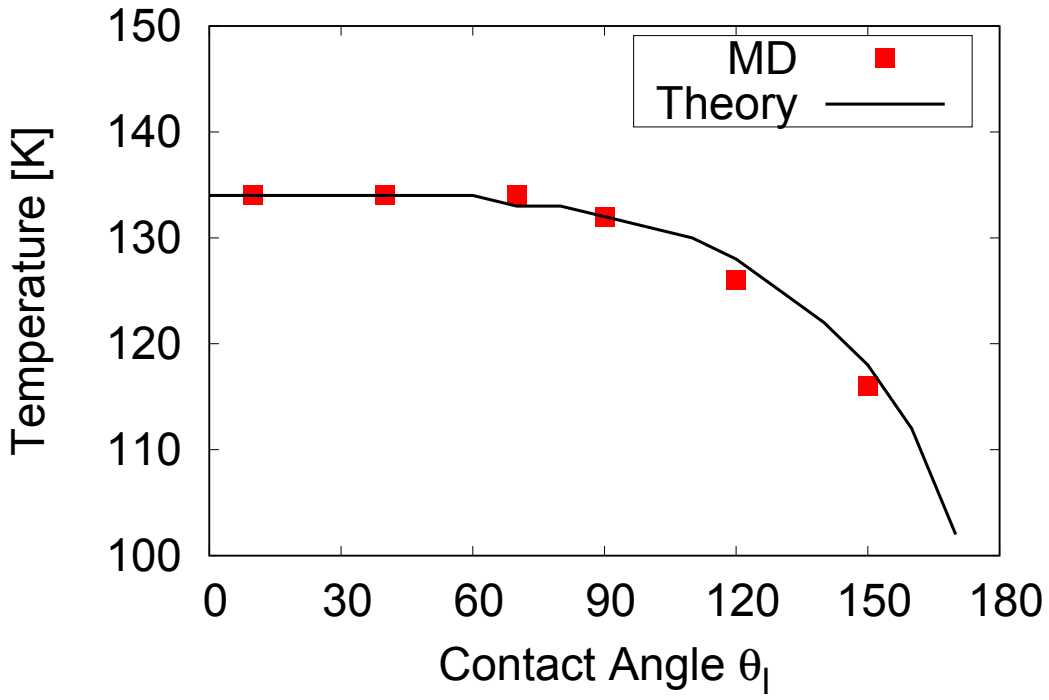

Figure 5.1: Temperature at which bubble nucleation occurs on smooth surfaces of varying wettability for liquid Argon at a pressure of 0.1 MPa

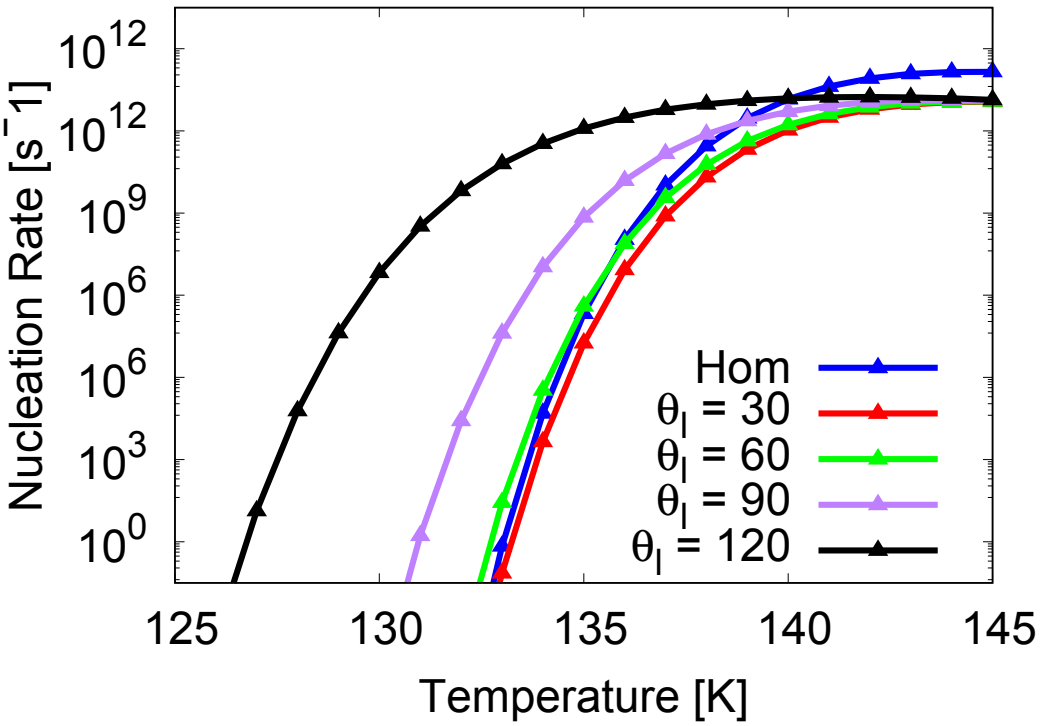

Figure 5.2: Nucleation rates calculated from CNT for homogeneous and various heterogeneous cases. The homogeneous rates are scaled by the volume of the simulation domain and the heterogeneous rates are scales by the surface area.

is illustrated in figure 5.2, where the expected number of nucleation events per second for various surface wettabilities as well as the homogeneous case is shown as calculated from equation (5.3), with the homogeneous nucleation rate exceeding the nucleation rate for the most wetting surface for all values of temperature. While adjusting the spacing between surface molecules will have some effect on the nucleation rate, by changing the density of preferential nucleation sites on the surface[1], it is not significant when compared to the order of magnitude difference between the predicted homogeneous and heterogeneous nucleation rates. While this work has not definitively shown a crossover from preferential heterogeneous to homogeneous nucleation, it remains an interesting open question and area for further research.

1. In the case of atomically smooth surfaces the nucleation site density corresponds to the gaps between lattice positions

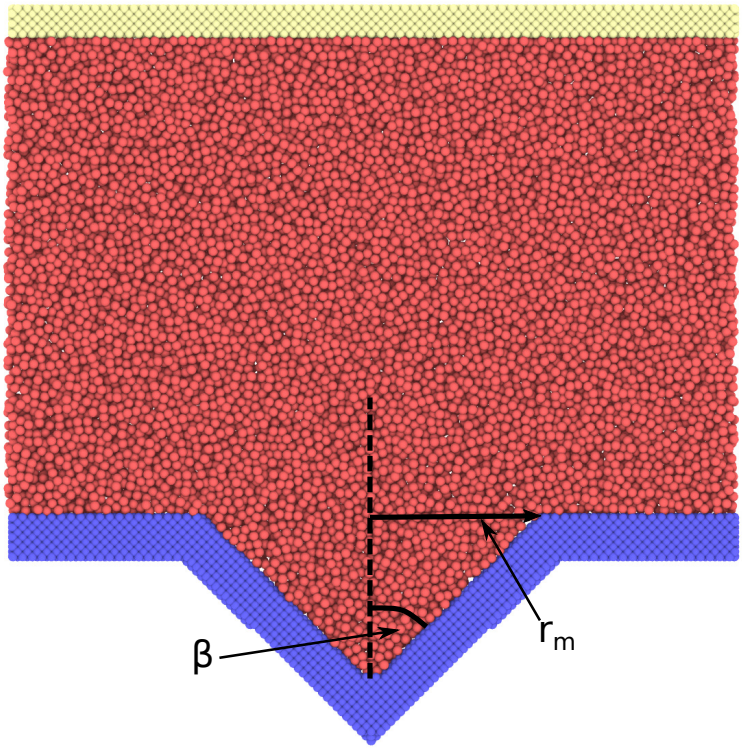

Figure 5.3: Simulation setup for nucleation investigations, highlighting roughness cone angle β and cavity mouth radius r_m.

5.5 Effect of Surface Topography

The effect of surface roughness on reducing the barrier to nucleation has been a motivating force behind the design of highly structured boiling surfaces (Chu et al., 2013). The ability of surface cavities to trap vapour or other non-condensable gases creates locations with a reduced barrier to nucleation. Enhanced boiling surfaces are designed with hierarchical, nanoporous, and re-entrant surface roughness to optimise the presence of these active sites (Carey, 2018).

The role of roughness is investigated here by using simple conic cavities on the solid surface, like those modelled by Lorenz et al. (1974). The surface cavities are created by deleting molecules from the wall to create a cone with a given radius and angle. This allows for the simplification of the analysis and comparison to the theory, which can then hopefully be extrapolated to more realistic surfaces in future work. Conical cavities are created on the solid surface defined by a combination of the cone angle β and the cavity mouth radius r_m. This setup is shown in figure 5.3.

For each of the cases tested here the cavity is initialised filled with liquid. The system is then equilibrated as before, initially thermostatted with the piston held in place, before the piston is released and allowed to reach the target pressure. The system temperature is then slowly ramped up until a vapour bubble forms.

Two distinct wetting regimes are visible throughout these simulations. The cavities either remain wetted during the equilibration process or dewet and fill with vapour. These approximately correspond to the Wenzel and Cassie–Baxter wetting states at the macroscale, respectively. The preferred state of the system, whether the cavity is wetted or dewetted, is controlled predominantly by the wettability of the surface and the geometry of the cavity. Higher wettability surfaces and less steep cavities (i.e. higher β) are more likely to remain wetted.

The images in figure 5.4 show two surfaces with the same cavity geometries, but different wettabilities, demonstrating different cavity wetting behaviour. On the more wetting surface, where the liquid contact angle $\theta_l = 10°$, the cavity remains wetted throughout the simulation procedure. The less wetting surface, with $\theta_l = 150°$ shows a visibly different wetting behaviour. In this case the cavity dewets during the equilibration procedure, forming a vapour-filled cavity. The liquid interface with the cavity is completely flat, in contrast with the convex interface that would be expected for this geometry (Carey, 2018; Lorenz et al., 1974). This matches the results of Xiao et al. (2017), who showed that the radius of curvature of a pinned surface vapour nanobubble matches the critical radius at the particular operating conditions of the system. By matching the critical radius, the pinned bubble can exist in a mechanical equilibrium with the surrounding liquid. In this case as the critical radius is significantly larger than the cavity radius ($r_c \gg r_m$), the interface appears flat. This configuration is more energetically stable as creating a curved interface would increase the interfacial free energy more than it would be reduced by allowing more molecules to vapourise.

Similarly, figure 5.5 shows two surfaces with the same wettability and different geometry cavities. The cavity remains completely wetted for the setup with cone angle $\beta = 60°$. When the cone angle is reduced to $\beta = 30°$, the wetting behaviour changes and the cavity spontaneously dewets during equilibration. Again, when the cavity has dewetted, a flat liquid-vapour interface forms, rather than the convex interface that would match the liquid contact angle as is assumed in the analysis of Lorenz et al. (1974). This shows the importance of both the cavity shape and fluid-surface interaction strength on the wetting state.

Having identified the two wetting regimes, their effect on vapour bubble nucleation can now be investigated. From the MD simulation results, a clear difference between the two regimes is identified.

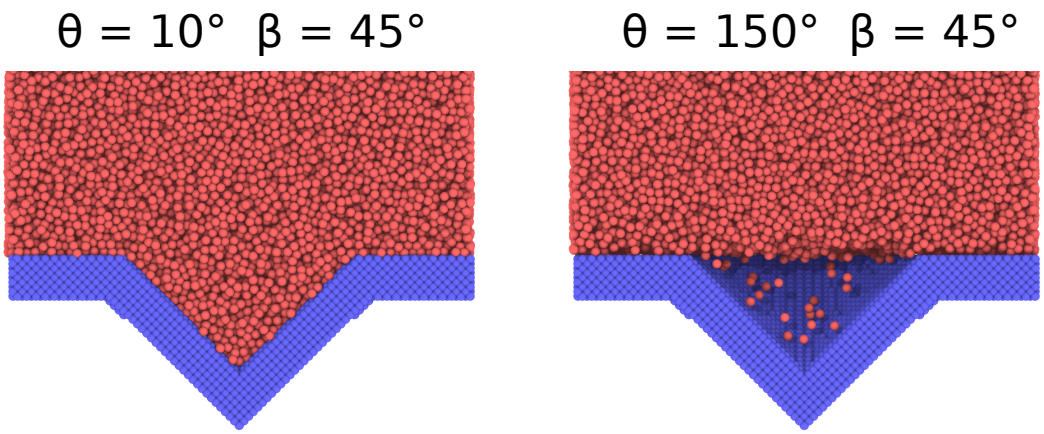

Figure 5.4: Comparison of the wetting state for identical cavities on surfaces with two different wettabilities. The cavity remains wetted on the $\theta = 10°$ surface but dewets on the $\theta = 150°$ surface.

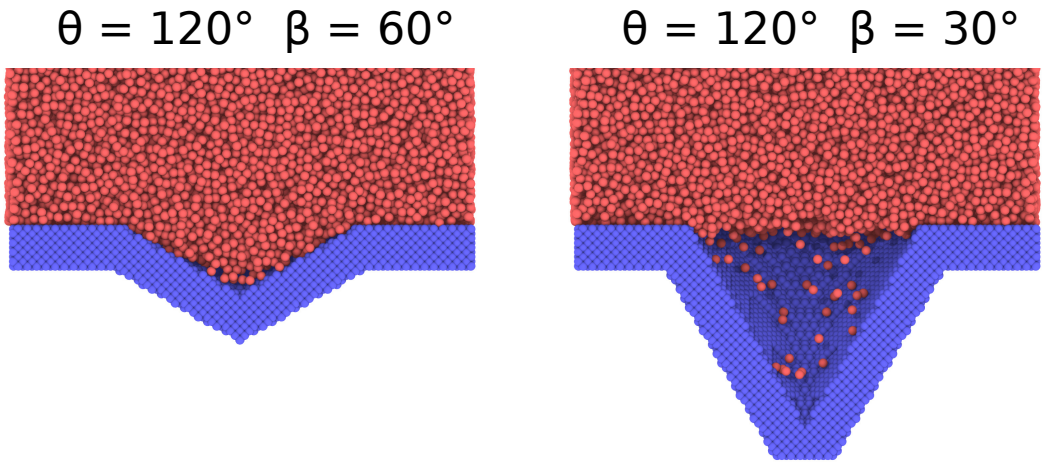

Figure 5.5: Comparison of the wetting state for identical cavities on surfaces with two different wettabilities. The cavity remains wetted on the cavity with $\beta = 60°$ (left) but dewets on the cavity with $\beta = 30°$ (right).

(a) *Wetted Cavities:* The simulation results in the wetted cavity regime do not differ significantly from the results of the smooth surface investigations. Nucleation is typically observed in the cavity but is occasionally observed to occur on the flat surface as well. The temperature required for nucleation to occur is identical in both cases. This shows that a completely wetted cavity does not significantly reduce the barrier to nucleation in the cases tested. However, as the parameter space investigated here is quite limited, further work is needed to completely verify this.

(a) *Dewetted Cavities:* A distinctly different nucleation behaviour is observed for dewetted cavities. When the cavity has dewetted, the vapour trapped in the cavity acts as a pre-existing nucleus and an active site at which nucleation can preferentially occur (Kaschiev, 2000). The presence of these sites reduces the barrier to nucleation, potentially allowing bubble growth to occur at lower superheats. These cavities produce bubbles with a base radius equal to the cavity radius r_m. For a bubble with a liquid contact angle θ_l this produces a radius of curvature of

$$r = \frac{r_m}{\sin \theta_l}. \tag{5.7}$$

Here θ_l represents the apparent liquid contact angle relative to the flat solid surface. The bubble will remain pinned and not grow out of the cavity until this angle reaches the intrinsic liquid contact angle of the surface, at which point it grows with a constant contact angle.

The plot in figure 5.6 shows the measured nucleation temperatures on dewetted cavity surfaces with different mouth radii for several different wettabilities. Good agreement is seen between the simulation results and theoretical predictions for $\theta_l = 90°$ with a slight overprediction for 120°. Notably, for the least wetting surface ($\theta_l = 150°$), the simulation results do not match the cavity based nucleation temperature criterion. This is because for this surface the critical nucleation temperature for a cavity-free surface is less than the nucleation temperature associated with the surface cavity. As a result, nucleation occurs at the lower, cavity free temperature and the surface cavity does not enhance nucleation. This indicates that for highly non-wetting surfaces, a minimum cavity radius is required for nucleation enhancement.

Having shown the importance of the wetting state to the nucleation behaviour of surfaces, an important open question remains, what decides the wetting state of a given surface? The simulation results have shown that the wetting state depends on the wettability and cavity geometry. These, however, do not completely describe the wetting state. While typically the cavities remain in one of the two wetting states throughout the entire

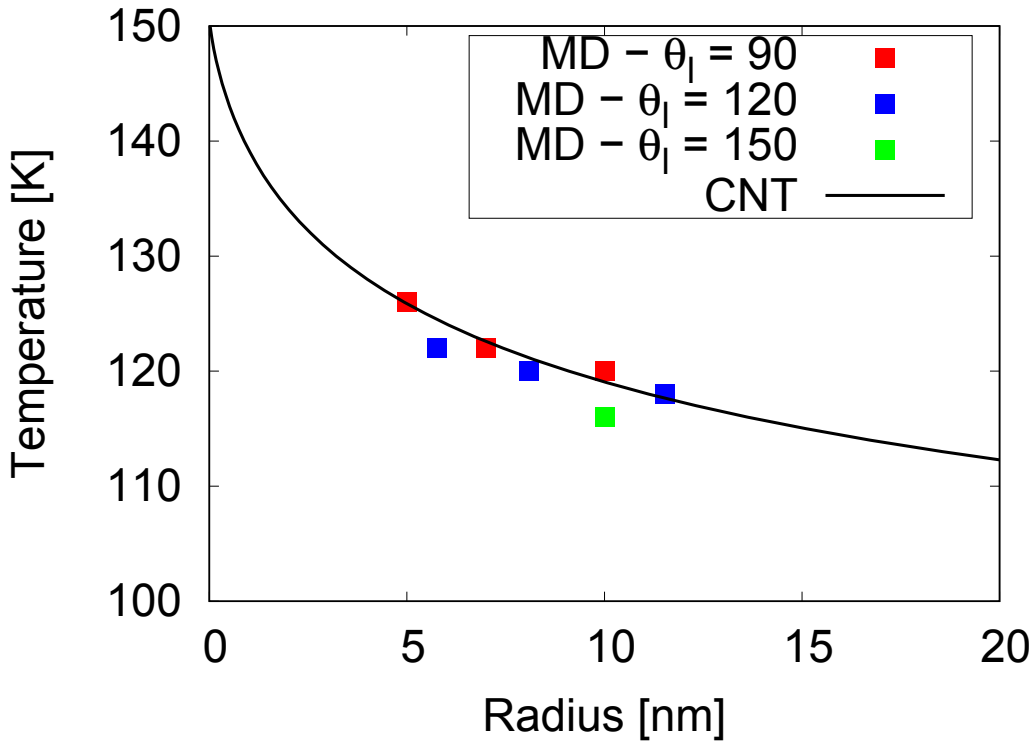

Figure 5.6: Comparison of the nucleation temperature on different wettability surfaces to the predictions of nucleation theory.

simulation procedure, under certain combinations of wettability and cavity geometry, a temperature-driven transition is observed. The exact mechanism driving this transition is not immediately clear, however the temperature dependence indicates that it is likely an activated, nucleation-like phenomenon.

At present, the underlying physics determining the wetting state are unclear and further investigation is required. Understanding the complete picture of cavity dewetting will give further insight into the factors effecting nucleation on realistic macroscale surfaces. The ability to control the presence or absence of pre-existing nucleation sites can then be used to optimise the design of surfaces looking to utilise bubble nucleation.

5.6 Summary of Results

Classical nucleation theory (CNT) has proven to be a powerful tool for predicting the nucleation behaviour of vapour bubbles on various surfaces. The initial results presented in this chapter have shown that CNT can accurately capture the effect of surface wettability on nucleation, showing excellent agreement between the predicted nucleation temperature and the values measured form MD simulation across a range of surface wettabilities.

The effect of surface roughness on nucleation has also been investigated, with a variety of distinct behaviours observed. When surface cavities remain wetted, nucleation occurs as if the surface were atomically smooth. When the cavities are dewetted, nucleation occurs when the cavity mouth radius matches the base radius of a critical bubble. This typically results in a reduction of the nucleation temperature. However, under certain conditions i.e. for small cavity radii on hydrophobic surfaces, nucleation occurs as if the surface were smooth. This is due to the radius of bubble that the surface cavities can support being smaller than the critical radius of bubbles that form on a smooth surface.

While these results have highlighted the usefulness of CNT for analysing vapour bubble nucleation, there remain open questions. In particular, discovering what causes the transition between the wetted and dewetted cavity states, and what potential impact this has on nucleation temperatures. Gaining a more complete understanding of the onset of nucleation will allow for improved design of boiling surfaces. It has been shown here that the wetting state is dependant on the geometry of the surface cavity and the wettability of the surface, but further investigation is needed to quantify these effects.

Chapter 6

Conclusions

Ranging from the eruption of volcanoes at the largest scales, to the detection of cosmic rays at the smallest, vapour bubbles are the driving force behind numerous natural, industrial, and scientific processes. Chapter 1 introduced the concept of vapour bubbles, highlighting the fundamental physics and what differentiates them from other types of bubbles. The differences between homogeneous and heterogeneous bubbles was introduced, describing how the fluid-solid interaction changes the shape of the bubble. The existing theoretical models describing the growth and formation of vapour bubbles were presented in the context of existing literature. This is used to frame the open problems with regard to the formation and growth of vapour bubbles.

The simulation methodology used in this work is presented in chapter 2. The concept of molecular dynamics (MD) is introduced and the fundamental principles involved are explained. The concepts of statistical mechanics and thermodynamic ensembles, which are necessary for the analysis of MD simulations, are described, providing details of the computation of the relevant thermodynamic properties. The Lennard–Jones potential is presented, and is validated against available reference data for argon. Further details are also provided about some of the techniques used to control pressure and detect the presence of vapour bubbles in the simulations.

Chapter 3 explores the growth of homogeneous vapour bubbles. The existing inertially- and thermally-limited models for bubble growth are given, with the discrepancies between the two highlighted. A new class of inertio-thermal (IT) models is presented, accounting for both the inertia driving the growth of bubbles and the limiting effects of thermal diffusion. Excellent agreement is seen between the predictions of these models and MD simulation, highlighting the improved agreement of the IT models in capturing the full lifetime of the vapour bubble.

This model is then extended in chapter 4, taking the change in geometry of heterogeneous bubbles into account. By accounting for the effects of surface wettability on changing not only the shape of the bubble but also the change in thermal diffusion in the surrounding liquid, the growth of heterogeneous vapour bubbles is accurately modelled, providing that spherical symmetry can still be approximated. It is shown that for highly wetting

surfaces, a non-evaporating layer forms underneath the bubble. This layer alters the force balance at the contact line, screening the bubble from the effects of the surface and producing bubbles with a constant contact angle, regardless of fluid-solid interaction strength. This is confirmed by analysing the effect of the layer on the interfacial stress balance in the contact line region. It is hoped that this improved understanding of heterogeneous bubble growth will lead to an improved performance of bubble technologies. In particular understanding the role that the surface plays on the thermal diffusion in the bulk liquid may provide additional insights for the design of phase change thermal management systems. The effect of surface adsorption in forming the non-evaporating layer has been shown to significantly alter the geometry of vapour bubbles (Ardron & Giustini, 2021). It has yet to be determined what effect this has on the interfacial heat transfer as the bubble grows, providing a promising avenue for future research. It is hoped that this model will help to provide a more complete understanding of the role of surface wettability in the growth of heterogeneous vapour bubbles, leading to further improvement in the design of bubble reliant systems.

Finally, chapter 5 presents initial findings into an investigation on the effects of surface wettability and roughness on vapour bubble nucleation. Using MD simulations, the effects of wettability can be investigated in isolation. By uniformly heating the fluid, rather than heating from the surface, the simulation results can be compared directly to nucleation theory. Excellent agreement of the measured nucleation temperatures with the predictions of CNT is seen across the full range of wettabilities. The investigation into surface roughness has identified two distinct regimes, a wetted and a dewetted cavity regime. In the wetted cavity regime, no difference is seen from the smooth surface case. In the dewetted cavity regime, bubbles will grow when the cavity radius matches the critical base radius predicted by CNT, provided this is at a lower temperature than the smooth surface case.

Overall, this thesis has attempted to close some of the gaps in the understanding of vapour bubbles. New models have been presented, accurately capturing the growth of both homogeneous and heterogeneous vapour bubbles. Initial results have indicated that CNT can capture the effect of wettability for nucleation on smooth surfaces, but there remain open questions on the effect of roughness, particularly at the nanoscale. It is hoped that these insights can help improve technologies such as multi-phase thermal management, acoustic cleaning, and minimise the wear of turbomachinery.

6.1 Future Work

The work presented in the thesis has answered some of the initial questions regarding the growth and nucleation of vapour bubbles. However, there remain open questions arising from this work.

6.1.1 Non-Evaporating Layer (NEL)

The results presented in chapter 4 have shown the importance of the NEL in determining bubble shape and subsequently growth rate. While a simple model has been presented for predicting the formation of the NEL, a more complete study is needed. The current investigation has shown good agreement for a select range of surface wettabilities and temperatures. While this serves its purpose for the investigation performed in this thesis, the model might make some interesting predictions if it is extended outside its current context.

Due to the combination of the linear scaling of the kinetic energy term, and exponential scaling of the potential energy term with temperature, this model predicts that for certain wettabilities, increasing temperature will cause the NEL to evaporate. Then, under a further increase in temperature, the NEL will reform. This non-intuitive behaviour has not yet been observed, but is an area of interest due to its potential impact on the shape and growth of vapour bubbles.

Further to this, more investigation is needed on the effects of wall thermalisation on the NEL. In the current investigation, a rigid, adiabatic wall has been used. Due to the highly non-continuum nature of the NEL, the thermal vibrations of wall molecules is expected to have a significant effect on the adsorption behaviour. Understanding the exact wetting behaviour of vapour bubbles is needed as continuum multi-phase solvers are investigation finer details of the bubble growth process such as the formation of the liquid microlayer, which is of significant interest due to its importance in thermal transport from the surface (Ardron & Giustini, 2021).

6.1.2 Activation of Surface Cavities

The results from chapter 5 have provided some interesting results into the activation of nucleation sites. The Lorenz et al. (1974) model does not appear to describe molecular cavities well. Further analysis is required to fully determine the factors controlling the wetting state of the surface cavities. The apparent absence of a partial wetting state is currently ambiguous. This may simply be due to the limited parameter space in the initial investigation. It does however, provide scope for further investigation.

Due to the activated, nucleation like transition that has been observed in the wetting state of the system, several further tests will be performed. Initially, a hysteresis investigation will be performed, to determine if a similar energy barrier is required to rewet an already dewetted cavity. This will confirm that the transition is an activated process. Additionally, a modified form of the nucleation rate expression will be developed, accounting for the geometry of the surface cavity and wettability of the fluid, to predict when this transition is expected to occur. The threshold nucleation rate obtained from the homogeneous and smooth surface simulations can be used for comparison. It is hoped that this will complete the picture of nanoscale heterogeneous nucleation.

Having understood the nucleation behaviour on smooth surfaces, as well as surfaces with simple geometric roughness, this analysis can be extended to surfaces with more realistic, fractal type roughness. This investigation can help to determine which of the previously investigated phenomena dominate in more application focused settings, with the ultimate aim being to apply these findings to real world systems.

Bibliography

Allen, M. P., & Tildesley, D. J. (2017). *Computer simulation of liquids: Second edition* (2nd ed.). Oxford University Press.

Andersen, H. C. (1980). Molecular dynamics simulations at constant pressure and/or temperature. *The Journal of Chemical Physics*, *72*(4), 2384–2393.

Ardron, K. H., & Giustini, G. (2021). On the wetting behavior of surfaces in boiling. *Physics of Fluids*, *33*(11).

Avdeev, A. A. (2016). *Bubble Systems*. Springer International Publishing.

Bardia, R., & Trujillo, M. F. (2019). Assessing the physical validity of highly-resolved simulation benchmark tests for flows undergoing phase change. *International Journal of Multiphase Flow*, *112*, 52–62.

Barrat, J. L., & Bocquet, L. (1999). Large slip effect at a nonwetting fluid-solid interface. *Physical Review Letters*, *82*(23), 4671–4674.

Berendsen, H. J., Postma, J. P., Van Gunsteren, W. F., Dinola, A., & Haak, J. R. (1984). Molecular dynamics with coupling to an external bath. *The Journal of Chemical Physics*, *81*(8), 3684–3690.

Betz, A. R., Jenkins, J., Kim, C. J., & Attinger, D. (2013). Boiling heat transfer on superhydrophilic, superhydrophobic, and superbiphilic surfaces. *International Journal of Heat and Mass Transfer*, *57*(2), 733–741.

Board, S. J., & Duffey, R. B. (1971). Spherical vapour bubble growth in superheated liquids. *Chemical Engineering Science*, *26*(3), 263–274.

Bourdon, B., Di Marco, P., Rioboo, R., Marengo, M., & De Coninck, J. (2013). Enhancing the onset of pool boiling by wettability modification on nanometrically smooth surfaces. *International Communications in Heat and Mass Transfer*, *45*, 11–15.

Bourdon, B., Rioboo, R., Marengo, M., Gosselin, E., & De Coninck, J. (2012). Influence of the Wettability on the Boiling Onset. *Langmuir*, *28*(2), 1618–1624.

Brennen, C. E. (2013). *Cavitation and bubble dynamics*. Cambridge University Press.

Busuioc, S., Frezzotti, A., & Gibelli, L. (2022). A Weighted Particle Scheme for Enskog-Vlasov Equation to Simulate Spherical Nano-Droplets/Bubbles. *SSRN Electronic Journal*.

Carey, V. (2018). *Liquid vapor phase change phenomena: An introduction to the thermophysics of vaporization and condensation processes in heat transfer equipment, Second Edition*. Taylor and Francis.

Chang, X., Huang, H., Cheng, Y. P., & Lu, X. Y. (2019). Lattice Boltzmann study of pool boiling heat transfer enhancement on structured surfaces. *International Journal of Heat and Mass Transfer*, *139*, 588–599.

Chen, R., Lu, M.-C., Srinivasan, V., Wang, Z., Cho, H. H., & Majumdar, A. (2009). Nanowires for Enhanced Boiling Heat Transfer. *Nano Letters*, *9*(2), 548–553.

Chen, Y., Zou, Y., Yu, B., Sun, D., & Chen, X. (2018). Effects of Surface Wettability on Rapid Boiling and Bubble Nucleation: A Molecular Dynamics Study. *Nanoscale and Microscale Thermophysical Engineering*, *22*(3), 198–212.

Chen, Y. J., Yu, B., Zou, Y., Chen, B. N., & Tao, W. Q. (2020). Molecular dynamics studies of bubble nucleation on a grooved substrate. *International Journal of Heat and Mass Transfer*, *158*.

Chu, K. H., Joung, Y. S., Enright, R., Buie, C. R., & Wang, E. N. (2013). Hierarchically structured surfaces for boiling critical heat flux enhancement. *Applied Physics Letters*, *102*(15), 151602.

Cooper, M. G., & Lloyd, A. J. (1969). The microlayer in nucleate pool boiling. *International Journal of Heat and Mass Transfer*, *12*(8), 895–913.

Dalle Donne, M., & Ferranti, M. P. (1975). The growth of vapor bubbles in superheated sodium. *International Journal of Heat and Mass Transfer*, *18*(4), 477–493.

Datta, S., Pillai, R., Borg, M. K., & Sefiane, K. (2021). Acoustothermal Nucleation of Surface Nanobubbles. *Nano Letters*, *21*(3), 1267–1273.

de Gennes, P.-G., Brochard-Wyart, F., & Quéré, D. (2004). Capillarity and Wetting Phenomena. *Capillarity and Wetting Phenomena*.

Denzel, P., Diemand, J., & Angélil, R. (2016). Molecular dynamics simulations of bubble nucleation in dark matter detectors. *Physical Review E*, *93*(1).

Dergarabedian, P. (1953). The Rate of Growth of Vapor Bubbles in Superheated Water. *Journal of Applied Mechanics*, *20*(4), 537–545.

Dergarabedian, P. (1960). Observations on bubble growths in various superheated liquids. *Journal of Fluid Mechanics*, *9*(1), 39–48.

Di Pasquale, N., & Davidchack, R. L. (2020). Shuttleworth equation: A molecular simulations perspective. *The Journal of Chemical Physics*, *153*(15), 154705.

Diaz, R., & Guo, Z. (2017). A molecular dynamics study of phobic/philic nano-patterning on pool boiling heat transfer. *Heat and Mass Transfer*, *53*, 1061–1071.

Diemand, J., Angélil, R., Tanaka, K. K., & Tanaka, H. (2014). Direct simulations of homogeneous bubble nucleation: Agreement with classical nucleation theory and no local hot spots. *Physical Review E - Statistical, Nonlinear, and Soft Matter Physics*, *90*(5), 13–16.

Din, X. D., & Michaelides, E. E. (1998). Transport Processes of Water and Protons through Micropores. *AIChE Journal*, *44*(1), 35–47.

Enríquez, O. R., Sun, C., Lohse, D., Prosperetti, A., & Van Der Meer, D. (2014). The quasi-static growth of CO2 bubbles. *Journal of Fluid Mechanics*, *741*, 1.

Florschuetz, L. W., Henry, C. L., & Khan, A. R. (1969). Growth rates of free vapor bubbles in liquids at uniform superheats under normal and zero gravity conditions. *International Journal of Heat and Mass Transfer*, *12*(11), 1465–1489.

Gallo, M., Magaletti, F., & Casciola, C. M. (2018). Thermally activated vapor bubble nucleation: The Landau-Lifshitz-Van der Waals approach. *Physical Review Fluids*, *3*(5), 1–20.

Gallo, M., Magaletti, F., & Casciola, C. M. (2021). Heterogeneous bubble nucleation dynamics. *J. Fluid Mech*, *906*, 20.

Gallo, M., Magaletti, F., Cocco, D., & Casciola, C. M. (2020). Nucleation and growth dynamics of vapour bubbles. *J. Fluid Mech*, *883*.

Gerardi, C., Buongiorno, J., wen Hu, L., & McKrell, T. (2010). Study of bubble growth in water pool boiling through synchronized, infrared thermometry and high-speed video. *International Journal of Heat and Mass Transfer*, *53*(19-20), 4185–4192.

Gong, S., & Cheng, P. (2012). A lattice Boltzmann method for simulation of liquid-vapor phase-change heat transfer. *International Journal of Heat and Mass Transfer*, *55*(17-18), 4923–4927.

Hill, T. L. (1956). *Statistical Mechanics: Principles and Selected Applications*. McGraw-Hill.

Israelachvili, J. (2011). *Intermolecular and Surface Forces*. Academic press.

Johnson, J. K., Zollweg, J. A., & Gubbins, K. E. (1993). The lennard-jones equation of state revisited. *Molecular Physics*, *78*(3), 591–618.

Joshi, S., Franc, J. P., Ghigliotti, G., & Fivel, M. (2019). SPH modelling of a cavitation bubble collapse near an elasto-visco-plastic material. *Journal of the Mechanics and Physics of Solids*, *125*, 420–439.

Kaschiev, D. (1970). Nucleation at Time Dependant Supersaturation. *Surface Science*, *22*, 319–324.

Kaschiev, D. (2000). *Nucleation: Basic Theory with Applications*. Butterworth Heinemann.

Kim, H., Truong, B., Buongiorno, J., & Hu, L. W. (2011). On the effect of surface roughness height, wettability, and nanoporosity on Leidenfrost phenomena. *Applied Physics Letters*, *98*(8), 083121.

Kinjo, T., Ohguchi, K., Yasuoka, K., & Matsumoto, M. (1999). Computer simulation of fluid phase change: vapor nucleation and bubble formation dynamics. *Computational Materials Science*, *14*, 138–141.

Kozynets, T., Fallows, S., & Krauss, C. B. (2019). Modeling emission of acoustic energy during bubble expansion in PICO bubble chambers. *Physical Review D*, *100*(5), 052001.

Lavino, A. D., Smith, E., Magnini, M., & Matar, O. K. (2021). Surface Topography Effects on Pool Boiling via Non-equilibrium Molecular Dynamics Simulations. *Langmuir*, *37*(18), 5731–5744.

Lee, H. C., Oh, B. D., Bae, S. W., & Kim, M. H. (2003). Single bubble growth in saturated pool boiling on a constant wall temperature surface. *International Journal of Multiphase Flow*, *29*(12), 1857–1874.

Lee, H. S., & Merte, H. (1996). Spherical vapor bubble growth in uniformly superheated liquids. *International Journal of Heat and Mass Transfer*, *39*(12), 2427–2447.

Lemmon, E. W., Bell, I. H., Huber, M. L., & McLinden, M. O. (2018). *NIST Standard Reference Database 23: Reference Fluid Thermodynamic and Transport Properties-REFPROP, Version 10.0, National Institute of Standards and Technology*.

Lennard-Jones, J. E. (1924). On the determination of molecular fields. —II. From the equation of state of a gas. *Proceedings of the Royal Society of London. Series A, Containing Papers of a Mathematical and Physical Character*, *106*(738), 463–477.

Lesage, F. J., Siedel, S., Cotton, J. S., & Robinson, A. J. (2014). A mathematical model for predicting bubble growth for low Bond and Jakob number nucleate boiling. *Chemical Engineering Science*, *112*, 35–46.

Liang, G., & Mudawar, I. (2021). Review of nanoscale boiling enhancement techniques and proposed systematic testing strategy to ensure cooling reliability and repeatability. *Applied Thermal Engineering*, *184*.

Lien, Y.-C. (1969). *Bubble growth rates at reduced pressure* (Unpublished doctoral dissertation). Massachuesetts Institute of Technology.

Liu, Y., Tang, J., Li, L., Shek, Y. N., & Xu, D. (2019). Design of Cassie-wetting nucleation sites in pool boiling. *International Journal of Heat and Mass Transfer*.

Lorenz, J. J., Mikic, B. B., & Robsenow, W. M. (1974). Effect of Surface Conditions on Boiling Characteristics. In *International heat transfer conference digital library* (pp. 35–39).

Lu, L., Fu, T., Tang, Y., Tang, T., Tang, B., & Wan, Z. (2016). A novel in-situ nanostructure forming route and its application in pool-boiling enhancement. *Experimental Thermal and Fluid Science*, *72*, 140–148.

Malan, L. C., Malan, A. G., Zaleski, S., & Rousseau, P. G. (2021). A geometric VOF method for interface resolved phase change and conservative thermal energy advection. *Journal of Computational Physics*, *426*, 109920.

Maroo, S. C., & Chung, J. N. (2008). Molecular dynamic simulation of platinum heater and associated nano-scale liquid argon film evaporation and colloidal adsorption characteristics. *Journal of Colloid and Interface Science*, *328*(1), 134–146.

Maroo, S. C., & Chung, J. N. (2009). Nanoscale liquid-vapor phase-change physics in nonevaporating region at the three-phase contact line. *Journal of Applied Physics*, *106*(6).

Maroo, S. C., & Chung, J. N. (2013). A possible role of nanostructured ridges on boiling heat transfer enhancement. *Journal of Heat Transfer*, *135*(4).

Martínez, L., Andrade, R., Birgin, E. G., & Martínez, J. M. (2009). Packmol: A Package for Building Initial Configurations for Molecular Dynamics Simulations. *Journal of Computational Chemistry*, *30*(13), 2157–2164.

Maruyama, S., & Kimura, T. (1999). A Molecular Dynamics Simulation of a Bubble Nucleation on Solid Surface. In *Trans. jpn. soc. mech. eng. b* (pp. 3461–3467).

Mikic, B. B., Rohsenow, W. M., & Griffith, P. (1970). On bubble growth rates. *International Journal of Heat and Mass Transfer*, *13*(4), 657–666.

Mirsandi, H., Rajkotwala, A. H., Baltussen, M. W., Peters, E. A., & Kuipers, J. A. (2018). Numerical simulation of bubble formation with a moving contact line using Local Front Reconstruction Method. *Chemical Engineering Science*, *187*, 415–431.

Mu, Y. T., Chen, L., He, Y. L., Kang, Q. J., & Tao, W. Q. (2017). Nucleate boiling performance evaluation of cavities at mesoscale level. *International Journal of Heat and Mass Transfer*, *106*, 708–719.

Mukherjee, A., & Kandlikar, S. G. (2007). Numerical study of single bubbles with dynamic contact angle during nucleate pool boiling. *International Journal of Heat and Mass Transfer*, *50*(1-2), 127–138.

Méndez-Bermúdez, J. G., Guillén-Escamilla, I., Méndez-Maldonado, G. A., & Alva-Tamayo, J. A. D. (2022). Argon force field revisited: a molecular dynamic study. *Journal of Physics Communications*, *6*(4), 041002.

Nagayama, G., & Cheng, P. (2004). Effects of interface wettability on microscale flow by molecular dynamics simulation. *International Journal of Heat and Mass Transfer*, *47*(3), 501–513.

Nishida, S., Surblys, D., Yamaguchi, Y., Kuroda, K., Kagawa, M., Nakajima, T., & Fujimura, H. (2014). Molecular dynamics analysis of multiphase interfaces based on in situ extraction of the pressure distribution of a liquid droplet on a solid surface. *The Journal of Chemical Physics*, *140*(7), 074707.

Novak, B. R., Maginn, E. J., & McCready, M. J. (2008). An atomistic simulation study of the role of asperities and indentations on heterogeneous bubble nucleation. In *Journal of heat transfer*.

Parker, E. N. (1954). Tensor virial equations. *Phys. Rev.*, *96*, 1686–1689.

Phan, H. T., Caney, N., Marty, P., Colasson, S., & Gavillet, J. (2010). A model to predict the effect of contact angle on the bubble departure diameter during heterogeneous boiling. *International Communications in Heat and Mass Transfer*, *37*(8), 964–969.

Plesset, M. S., & Zwick, S. A. (1954). The growth of vapor bubbles in superheated liquids. *Journal of Applied Physics*, *25*(4), 493–500.

Plimpton, S. (1995). Fast Parallel Algorithms for Short-Range Molecular Dynamics. *Journal of Computational Physics*, *117*, 1–19.

Prosperetti, A. (1982). A generalization of the Rayleigh-Plesset equation of bubble dynamics. *Physics of Fluids*, *25*, 409.

Prosperetti, A. (2004). Bubbles. *Physics of Fluids*, *16*(6), 1852.

Prosperetti, A. (2017). *Vapor Bubbles* (Vol. 49). Annual Reviews Inc.

Prosperetti, A., & Plesset, M. S. (1978). Vapour-bubble growth in a superheated liquid. *Journal of Fluid Mechanics*, *85*(2), 349–368.

Rayleigh, L. (1917). On the pressure developed in a liquid during the collapse of a spherical cavity. *The London, Edinburgh, and Dublin Philosophical Magazine and Journal of Science*, *34*(200), 94–98.

Reinke, P. (1997). Site deactivation techniques for suppression of nucleation in superheated liquid. *Experimental Heat Transfer*, *10*(2), 133–140.

Robinson, A. J. (2002). *Bubble Growth Dynamics in Boiling* (Unpublished doctoral dissertation). McMaster University.

Robinson, A. J., & Judd, R. L. (2001). Bubble growth in a uniform and spatially distributed temperature field. *International Journal of Heat and Mass Transfer*, *44*(14), 2699–2710.

Robinson, A. J., & Judd, R. L. (2004). The dynamics of spherical bubble growth. *International Journal of Heat and Mass Transfer*, *47*(23), 5101–5113.

Rosales-Pelaez, P., Garcia-Cid, M. I., Valeriani, C., Vega, C., & Sanz, E. (2019). Seeding approach to bubble nucleation in superheated Lennard-Jones fluids. *Physical Review E*, *100*(5), 52609.

Rosales-Pelaez, P., Sanchez-Burgos, I., Valeriani, C., Vega, C., & Sanz, E. (2020). Seeding approach to nucleation in the NVT ensemble: The case of bubble cavitation in overstretched Lennard Jones fluids. *Physical Review E*, *101*(2), 1–10.

Schneider, T., & Stoll, E. (1978). Molecular-dynamics study of a three-dimensional one-component model for distortive phase transitions. *Physical Review B*, *17*(3), 1302–1322.

She, X., Shedd, T. A., Lindeman, B., Yin, Y., & Zhang, X. (2016). Bubble formation on solid surface with a cavity based on molecular dynamics simulation. *International Journal of Heat and Mass Transfer*, *95*, 278–287.

Shi, B., Wang, Y. B., & Chen, K. (2015). Pool boiling heat transfer enhancement with copper nanowire arrays. *Applied Thermal Engineering*, *75*, 115–121.

Tanaka, K. K., Tanaka, H., Angélil, R., & Diemand, J. (2015). Simple improvements to classical bubble nucleation models. *Physical Review E - Statistical, Nonlinear, and Soft Matter Physics*, *92*(2), 1–9.

Theofanous, T. G., & Patel, P. D. (1976). Universal relations for bubble growth. *International Journal of Heat and Mass Transfer*, *19*(4), 425–429.

Ujereh, S., Fisher, T., & Mudawar, I. (2007). Effects of carbon nanotube arrays on nucleate pool boiling. *International Journal of Heat and Mass Transfer*, *50*(19-20), 4023–4038.

van Stralen, S. J., Cole, R., Sluyter, W. M., & Sohal, M. S. (1975). Bubble growth rates in nucleate boiling of water at subatmospheric pressures. *International Journal of Heat and Mass Transfer*, *18*(5), 655–669.

Vemuri, S., & Kim, K. J. (2005). Pool boiling of saturated FC-72 on nano-porous surface. *International Communications in Heat and Mass Transfer*, *32*(1-2), 27–31.

Verlet, L. (1967). Computer "Experiments" on Classical Fluids. I. Thermodynamical Properties of Lennard-Jones Molecules. *Physical Review*, *159*, 98.

Wang, Z. J., Valeriani, C., & Frenkel, D. (2009). Homogeneous bubble nucleation driven by local hot spots: A molecular dynamics study. *Journal of Physical Chemistry B*, *113*(12), 3776–3784.

Xiao, Q., Liu, Y., Guo, Z., Liu, Z., Frenkel, D., Dobnikar, J., & Zhang, X. (2017). What experiments on pinned nanobubbles can tell about the critical nucleus for bubble nucleation. *European Physical Journal E*, *40*(12), 114.

Yamaguchi, Y., Kusudo, H., Surblys, D., Omori, T., & Kikugawa, G. (2019). Interpretation of Young's equation for a liquid droplet on a flat and smooth solid surface: Mechanical and thermodynamic routes with a simple Lennard-Jones liquid. *Journal of Chemical Physics*, *150*(4).

Yamamoto, T., & Matsumoto, M. (2012). Initial stage of nucleate boiling: Molecular dynamics investigation. *Journal of Thermal Science and Technology*.

Yasui, K. (2018). *Acoustic Cavitation and Bubble Dynamics*. Springer.

Zhang, L., Xu, J., Liu, G., & Lei, J. (2020). Nucleate boiling on nanostructured surfaces using molecular dynamics simulations. *International Journal of Thermal Sciences*, *152*, 106325.

Zhao, Z., Zhang, J., Jia, D., Zhao, K., Zhang, X., & Jiang, P. (2017). Thermal performance analysis of pool boiling on an enhanced surface modified by the combination of microstructures and wetting properties. *Applied Thermal Engineering*, *117*, 417–426.

Zhou, W., Li, Y., Li, M., Wei, J., & Tao, W. (2019). Bubble nucleation over patterned surfaces with different wettabilities: Molecular dynamics investigation. *International Journal of Heat and Mass Transfer*, *136*, 1–9.

Zou, A., Singh, D. P., & Maroo, S. C. (2016). Early Evaporation of Microlayer for Boiling Heat Transfer Enhancement. *Langmuir*, *32*(42), 10808–10814.